STUDY OF PERMEABILITY CHANGES INDUCED BY EXTERNAL STIMULI ON CHEMICALLY MODIFIED ELECTRODES.

by

DINGIRI MUDIYANSELAGE NELUNI T. PERERA

B.S., The Open University of Sri Lanka, 2003

AN ABSTRACT OF A DISSERTATION

submitted in partial fulfillment of the requirements for the degree

DOCTOR OF PHILOSOPHY

Department of Chemistry
College of Arts and Sciences

KANSAS STATE UNIVERSITY
Manhattan, Kansas

2010

Abstract

This research was focused on understanding how external stimuli affect the permeability of the chemically modified electrodes, and how the materials used in modifying the working electrodes respond to the changes in the surface charge. We adopted a voltammetric type electrochemical sensor to investigate the permeability effects induced by pH and organic solvents. The working electrodes used in this research were chemically modified with thioctic acid self assembled monolayer (TA SAM), track etched polycarbonate membranes (TEPCM) and PS-b-PMMA nanoporous films (polystyrene-block-polymethylmethacrylate). We studied the permeability behavior of each of the material upon application of external stimuli.

In chapter 3, the permeability changes induced by change in surface charge of thioctic acid SAM was investigated. The surface charge of the monolayer was tuned by changing pH of the medium, which resulted in decrease of redox current of a negatively charged marker due to deprotonation of the surface –COOH groups of TA SAM. Decrease in redox current reflected a decrease in the reaction rate, and by using closed form equations the effective rate constants at several pKa values were extracted.

In chapter 4, permeability changes induced by pH in TEPCM were investigated. We assessed the surface charge of these membranes via cyclic voltammetry generated for neutral and charged redox molecules. Limiting current of charged markers were affected by the surface charge induced by pH, where as the redox current for the neutral marker was not affected. Experimental redox currents were larger than the theoretical current, indicating that redox molecules preferentially distributed in a surface layer on the nanopore. Organic solvent induced permeability changes of PS-b-PMMA nanoporous films were investigated via electrochemical impedance spectroscopy and AFM. Higher response of pore resistance in the presence of organic solvents indicated either swelling of the nanoporous film or partitioning of organic solvents in the pores. However AFM data revealed that the permeability changes are due to partitioning of the solvents rather than swelling of the porous film, since there was no appreciable change if the pore diameter in the presence of solvents.

STUDY OF PERMEABILITY CHANGES INDUCED BY EXTERNAL STIMULI ON CHEMICALLY MODIFIED ELECTRODES

by

DINGIRI MUDIYANSELAGE NELUNI T. PERERA

B.S., The Open University of Sri Lanka, 2003

A DISSERTATION

submitted in partial fulfillment of the requirements for the degree

DOCTOR OF PHILOSOPHY

Department of Chemistry
College of Arts and Sciences

KANSAS STATE UNIVERSITY
Manhattan, Kansas

2010

Approved by:

Major Professor
Dr. Takashi Ito.

Copyright

Abstract

This research was focused on understanding how external stimuli affect the permeability of the chemically modified electrodes, and how the materials used in modifying the working electrodes respond to the changes in the surface charge. We adopted voltammetric type electrochemical sensor to investigate the permeability effects induced by pH and organic solvents. The working electrodes used in this research were chemically modified with thioctic acid self assembled monolayer (TA SAM), track etched polycarbonate membranes (TEPCM) and PS-b-PMMA nanoporous films (polystyrene-block-polymethylmethacrylate). We studied the permeability behavior of each of the material upon application of external stimuli.

In chapter 3, the permeability changes induced by change in surface charge of thioctic acid SAM was investigated. The surface charge of the monolayer was tuned by changing pH of the medium, which resulted in decrease of redox current of a negatively charged marker due to deprotonation of the surface –COOH groups of TA SAM. Decrease in redox current reflected a decrease in the reaction rate, and by using closed form equations the effective rate constants at several pKa values were extracted.

In chapter 4, permeability changes induced by pH in TEPCM were investigated. We assessed the surface charge of these membranes via cyclic voltammetry generated for neutral and charged redox molecules. Limiting current of charged markers were affected by the surface charge induced by pH, where as the redox current for the neutral marker was not affected. Experimental redox currents were larger than the theoretical current, indicating that redox molecules preferentially distributed in a surface layer on the nanopore. Organic solvent induced permeability changes of PS-b-PMMA nanoporous films were investigated via electrochemical impedance spectroscopy and AFM. Higher response of pore resistance in the presence of organic solvents indicated either swelling of the nanoporous film or partitioning of organic solvents in the pores. However AFM data revealed that the permeability changes are due to partitioning of the solvents rather than swelling of the porous film, since there was no appreciable change if the pore diameter in the presence of solvents.

Table of Contents

List of Figures

List of Tables

Acknowledgements

Dr. Takashi Ito, thank you for giving me the opportunity to work in your group, your continuous guidance not only in research but in academic work too.

The Ito Group – grad, undergrad students, post docs past and present – Dr. Yongxin Li, Dr. Ahmad Audi, Dr. Helene Maire-Afeli, Shaida Ibrahim, Bipin Pandey, Feng Li, Khanh Hoa Tran Ba, Sarah Forman, and Evgeniy Shishkin. I have learnt a lot from every one of you.

I thank Ms. Shinobu Nagasaka for providing cyclic voltammetry data presented in the 3rd chapter.

I would like to thank my committee members –Dr. Stefan Bossmann, Dr. Christopher Culbertson, Dr. Mary Rezac and Dr. Dwight Day.

I thank Dr. Culbertson, for letting me use the profilometer and Scott and Kurt for their help in using the profilometer.

To the Chemistry department faculty and staff - I would like to thank Tobe Eggers, Ron Jackson, Jim Hodgson and Richard Bachamp for their valuable assistance in fabricating devices for my research. I would also like to thank the Chemistry office staff – Mary Dooley, Donna Wright, Connie Cusimano, Kim Ross, and Linda Gibbs for helping me in various ways.

To my friends – Smita, Kanika, Abhi, Prashant, Evan and Claudia thank you guys for many wonderful times spent together. (Specially the Ruchi lunches)

To my family – thank you so much for all your support and guidance throughout these five years. To Amma, Thaththa, malli and Kiki, you are the best family one could ask for. Without you I would not have been able to come this far. Kaniskha, Thank you so much for being there for me and being so patient with me whenever I get stressed out.

Dedication

To Amma and Thaththa.

Chapter 1 - Introduction

1.1 Electrochemical Sensors

Chemical sensing is one of the areas in analytical instrumentation that has shown a largest development. Chemical sensors are devices that detect and quantify specific analyte or a reaction.[1] A chemical sensor consists of a chemically selective layer to detect the response from the analyte from its environment and a transducer to transform the response to detector response.[2] They are categorized into groups depending on the operating principle of the transducer as electrochemical, optical, thermal, mass, electrical, and magnetic. Out of these types of sensors, electrochemical sensors are the leading ones due to their experimental simplicity, low detection limits and cost effectiveness. Electrochemical sensing merges with other branches of analytical chemistry, such as microfluidics, polymer materials and microscopic techniques (scanning electrochemical microscopy, scanning tunneling microscopy).[3, 4] Electrochemical sensors measure the changes in electrochemical quantities related to electrode processes in the presence of analyte such as ampherometry, voltammetry or coulometry. It also measure the changes in the electrical properties of the medium (e.g. monolayers, membranes) when it is bonded to the analyte, such as potentiometry, capacitance, conductivity and dielectric permittivity.[1] Depending on the electrochemical quantity measured, three main types of electrochemical sensors are identified. They are potentiomentric, amperometric (including voltammetric) and conductometric sensors.

Potentiometric sensors are based on the change in ionic species distribution in the electrode solution interface in the presence of an analyte. This measures the potential difference of the electrode or a membrane and a reference electrode, in the absence of a current. The potential of the reference electrode should be constant and known, and it should also be insensitive to the analyte being measured. These sensors are categorized into three groups, viz. ion selective electrodes (ISE), coated wire electrodes, and field effect transistors. Ion selective electrodes selectively measure the concentration of ionic species. The most common ISE is the pH electrode. These sensors use membranes which are permselective and ion conducting. The potential of the working electrode is related to the concentration of the analyte. Selectivity of Pb^{2+} ions over Cu^{2+}, Cd^{2+}, Mn^{2+}, Zn^{2+}, Co^{2+}, Ni^{2+} was demonstrated for an ISE based on p-tert-

butyl-calix[4]arene thioamide in a PVC (poly vinyl chloride) ionophore.[5] Aluminum ISE was developed to detect and quantify the Al^{3+} ions in pharmaceutical (in Al syrup) environmental (tap water) and food (tea leaves) samples. Potentiometric membrane of this ISE was composed of PVC, 6-(4-nitrophenyl)-2-phenyl-4-(thiphene-2-yl)-3-5-diaza bicycle[3.1.0]hex-2-ene (ionophore) and acetopheneone and oleic acid. This sensor showed improved detection limit (630nM), response time (~ 10s) and longer life time (~ 3 months).[6] An anion selective ISE was fabricated from Rh^{3+} porphyrin based ionophore to detect NO_2^- over lipophilic anions such as perchlorate, thiocyanate and salicylate.[7] A pH sensor developed from a fluorous membrane showed a selectivity of H^+ over K^+ over a large range of pH (5-13).[8]

Coated wire electrodes use a conductive wire coated with a suitable ion selective polymer (e.g. PVC, polyvinylbenzyl chloride or polyacrylic acid). They do not require an internal reference electrode, hence can be miniaturized.[2] Ion selective field effect transistors (ISFET) an ion selective membrane is incorporated on the gate area of a field effect transistor. This is a solid state device which can measure the charge build up in the ion selective membrane. This type of sensor is mainly used in *in-vivo* applications such as analysis of Human Serum Albumin[9] and in immunosensors[10].

In amperometric or voltammetric sensors signal transduction is the current generated during the transfer of electrons to or from the analyte. In amperometry, current flow is measured at a single applied potential, while in voltammetric sensor; current is measured when the potential is scanned from one value to another. These sensors use 2 or 3 electrode system; working, reference and /or a counter electrode. Use of an electrolyte solution is required to eliminate mass transfer due to migration, maintain a constant ionic concentration and to reduce solution resistance. An important part of the amperometric / voltammetric sensor is the working electrode used. It can consist of metals such as gold, silver, carbon, copper and platinum. Working electrodes in these sensors come in various shapes and dimensions, and provides means to miniaturize the sensors. Chemically modifying the working electrode by immobilizing a receptor opens up a multitude of applications for these sensors, due to greater control of the electrode reactions and electrode characteristics.[2] Modified electrodes were used in detection of glycated hemoglobin, a long term biomarker for glucose levels. Surface of a gold electrode was modified with a self assembled monolayer (SAM) of thiophene boric acid. Binding of

hemoglobin to the boric acid immobilize the hemoglobin on the electrode surface, which was detected by electrochemical impedance spectroscopy.[11] Use of whole bacteria (*Shewanella*) cells as electron transfer material for EC sensors has been demonstrated. This sensor was used to detect arsenite, H_2O_2 and nitrie ions.[12] Nanomaterials such as carbon nanotubes are ideal for EC sensors since they provide larger surface area, high aspect ratios and catalytic properties.[13] Multi walled carbon nanotubes have been used in detection of chemical warfare agents. In this sensor MWCNT were immobilized on ITO (indium tin oxide0 electrode), and ferrocene amino acids conjugates were attached to the CNTs, which can bind to CWA mimicking analytes. AC voltammetry and capacitance measurements were done to quantify the CWA analytes.[14] An EC based on microelectrode array was fabricated from carbon fiber for detection of neurotransmitter release.[15] Sensors have been developed to detect environmentally hazardous metal ions like Pb^{2+},[16-18] Cd^{2+},[16, 17] Tl^{+}[19] using glassy C electrodes modified with Nafion film containing MWCNTs, Bi nanoparticles, Langmuir Blodgett films. Perchlorate ions in drinking water has been detected by a gold electrode modified with a fluid membrane composed of PVC film and poly(3-octylthiphene).[20] Voltammetric sensors for detection of NO (major compound involved in signaling of eukaryote and prokaryote cells, nitrogen cycle) have been fabricated from various electrode nmaterials.[21-23]

Conductometric sensors measure the electric conductivity change of a film or in bulk material in the presence of an analyte. Basically they are non-selective, but with the use of modified electrode surfaces, selectivity of analytes has become possible. The advantage of conductometric sensors is that they do not need a reference electrode.[2] These sensors are mainly utilized to detect gaseous analytes. These sensors include, O_2 sensors based on a CdS thin film,[24] humidity sensor fabricated from $MnWO_4$ porous films,[25] H_2S sensor based on copper oxide or oxides doped with Cu,[26, 27] and semi conducting Ga_2O_3 thin films for detection of CH_4 gas.[28]

When comparing the above types of electrochemical sensors voltammetric / amperometric based ECs show more versatility due to the ability to use a variety of working electrode material (gold, silver, Pt, C), chemical modification of the working electrode (SAM coated, LB films, polymer brush, film coated etc), electrode size and arrangement (micro electrodes, nano electrodes, micro / nano array electrodes). Thus voltammetric / ampherometric ECs are far more attractive in analytical view point.

1.1.1 Ion Channel Sensors

Ion channel sensors (ICS) are electrochemical sensors widely used in detection of large hydrophilic, multi charged ionic species such as proteins, polysaccharides, oligonucleotides and multivalent inorganic ions.[29] The concept of ICS stems from ion channels in biological systems. Ion channels in biological systems are selective towards substrates, and upon binding of the correct substrate with the receptors, induce opening of ion specific channels. This allows permeation of ions across the biological membrane, creating an electrochemical potential gradient.[30] The earliest work on ICS showed the effect of deprotonated acid groups in a self assembled monolayer on redox current of a marker ion at the electrode surface.[31] However the first reported work of biomimitic ICS was demonstrated by Sugarawa et.al. in late 1980s. In this work, a synthetic lipid multi layer was coated on a glassy carbon electrode by Langmuir-Blodgett method. Acidic phosphate head in the phospholipid bi-layer interacted with the di-valent metal ions, causing a conformational change in lipid membrane, opening up the channels in the bi-layer, through which marker ions permeated to the underlying electrode.[30]

Biomimitic ICS has been developed for many analytes such as redox inactive small ions and molecules[30, 32-39] and large bioactive molecules.[40-43] ICS can be categorized in to two groups, depending on their response mechanisms. In one group the analyte molecules form inclusion type complexes with the substrate, and physically block the intramolecular channels, thus preventing the permeation of the redox molecules to the electrode surface.[32, 39] The other type of ICS shows electrostatic attraction/ repulsion based mechanism. Binding of ionic analytes change the net charge of the synthetic receptor layer, and this regulates the permeation of marker ions to the electrode surface.

Binding of analytes to the receptor sites immobilized films will change the surface charge and / or porosity of the films.[30, 32, 44] This will result in a gated permeability of the marker molecule, which is the mode of signal transduction in ICS. This means that for ICS the signal transduction method doesn't have to be tailored for each analyte-receptor combination.[29] Another advantage in ICS is the signal amplification, since a small number of analyte molecules give an electrochemical response caused by a larger number of redox species.

This research investigates the processes triggered by binding of analytes to receptor sites of immobilized films. These processes include changes in surface charge of self assembled

monolayer (Thioctic Acid) modified electrode (chapter 3), and in nanoporous track etched membranes (chapter 4). Hence these chapters discuss the change in electrode kinetics due to surface charge change in SAM (Self Assembled Monolayer) modified electrodes and the permeability of redox markers in nano-porous TEPCM (Track Etched Poly Carbonate Membranes). An extension of the research discusses the gated permeability of redox markers, induced by organic solvents in nano-porous di block copolymer membranes. The basic concept connecting this whole research is the permeability induced by surface charge changes and external stimuli.

1.2 Motivations and Objectives

There is a huge drive for fabrication of ultra sensitive, selective, miniaturized devices for array based sensors, detectors in in-vivo biological research, micro fluidic chips etc. These devices come as micro and nano scale ion channel sensors, nano-porous membrane and block copolymer based array electrodes. Therefore it is necessary to understand the response behavior of materials used in these devices in order to maximize their sensitivity and selectivity.

The research presented in this dissertation covers different nano material, viz. thioctic acid SAM, TEPCM, and PS-b-PMMA (polystyrene block polymethylmethacrylate) nano-porous films. These materials were connected together under one concept; permeability changes induced by surface charge changes, which can be regulated by external stimuli. The overall goal of this research was to investigate the permeability changes brought about by various external stimuli such as pH of the medium and organic solvents. Understanding how each of the aforementioned materials behaves on applied external stimuli would allow one to optimize the properties of them for sensor applications.

Chapter 2 discusses the analytical techniques used in characterizing and measuring permeability changes triggered by external stimuli. Chapter 3 discuss the effect of change in surface charge on electrochemical reaction kinetics, based on a Thioctic acid SAM modified microelectrode. This system represents a charge based ICS (CB-ICS). In chapter 4, cyclic voltammetry studies done on a recessed nano-disk array electrode, fabricated from TEPCM is discussed in terms of permeability changes. This study shows the effect of medium pH on the surface charge of nano-pores and permeability changes of neutral and charged redox markers.

Chapter 5 is based on a study of permeability changes induced by organic solvents in PS-b-PMMA nano-porous films. This study was focused on determining whether the permeability change was due to swelling caused by the organic solvents or the partitioning of the solvents in the nano-pores.

1.3 Background / Literature Review

1.3.1 Self Assembled Monolayers (SAM)

Thioctic acid SAM modified micro electrode was used to discuss surface charge change due to pH of the medium, and the resulting permeability changes for a negatively charged redox marker. This system represents a chemically modified voltammetric type electrochemical sensor (Figure 1.1) Self assembly of molecules is based upon spontaneous adsorption of organic molecules on a solid surface to lower the free energy of the metal surface and the environment.[4546] General structure of SAM consists of a surface active head group which binds with the substrate, and end group at the monolayer surface, and an alkyl chain connecting the head and the tail which also facilitates monolayer packing[47] (Figure 1.2). SAM formed on a substrate has many advantages for sensor applications such as tailoring the end group for selectivity, fast response, immobilization of biological recognition receptors and high response.[46, 48, 49]

Surface active thiol group binds strongly to the substrate (gold) according to the following equation.[47, 50]

$$2Au + RS\text{-}SR \rightarrow 2Au\text{-}SR \qquad (1.1)$$

End groups can be functionalized to control the interfacial properties of the monolayer (hydrophilic / hydrophobic). In this research, -COOH terminated thioctic acid SAM gives a hydrophilic character to the monolayer interfacial properties.

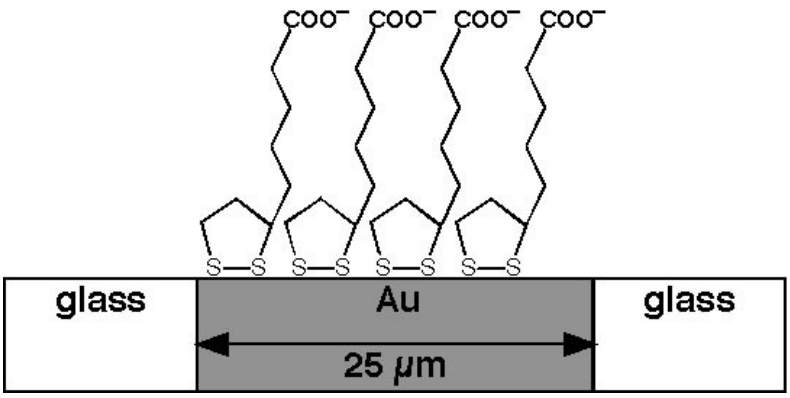

Figure 1.1 Schematic diagram of Thioctic Acid self assembled monolayer on gold disk electrode.

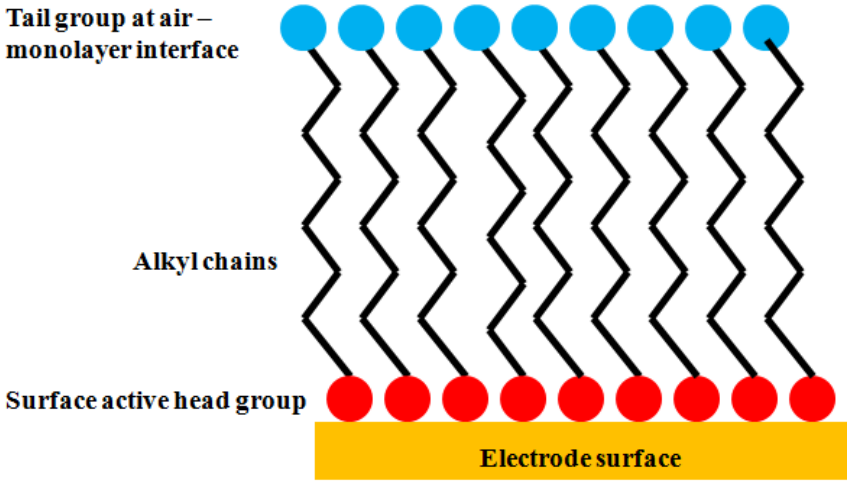

Figure 1.2 Schematic diagram of a self assembled monolayer formed on a substrate.

1.3.2 Monolithic nanoporous membranes

Monolithic nanoporous membranes include track etched membranes (polycarbonate / polyester), anodic aluminum oxide membranes, and block copolymer (BCP) nanoporous films.[51] Two types of monolithic nanoporous membranes/ films were used in this research, viz. track etched polycarbonate membranes (TEPCM) and PS-b-PMMA nanoporous films. In contrast to other nanoporous media such as entangled polymer gels, charged polyelectrolyte films, monolithic nanoporous membranes have well defined structures with uniform cylindrical pores.[51]

TEPCM polymer membranes are fabricated by bombarding a sheet of polycarbonate or polyester film with nuclear fission and subsequent chemical etching of the damage tracks created

by ion bombardment. Unlike anodic alumina membranes and BCP films, pore densities of TEPCMs are low and the distribution of pores is random (Figure 1.3). Pore diameter of TEPCM can be controlled by controlling the etching time and pore shapes can be modified by controlling the bombarding and etching conditions.[52, 53] Pore size of TEPCMs is controlled by electroless deposition of gold on nanopore surface.[52, 54] Chemical Functionalization of nanopore surface offers selectivity in molecular separations. This is realized by modification of gold deposited pore surface with thiol SAMs or amidation of polyester based TEPMs.[52, 54] These membranes are used in many applications such as size exclusive and chemical interaction based separations,[52, 54] as model systems for mass transport studies,[55] as templates for synthesis of nanowires,[56] nano electrode ensembles,[57, 58] as diffusion controlled separators between channels in microfluidic devices,[59] and as potential gates.[60-64]

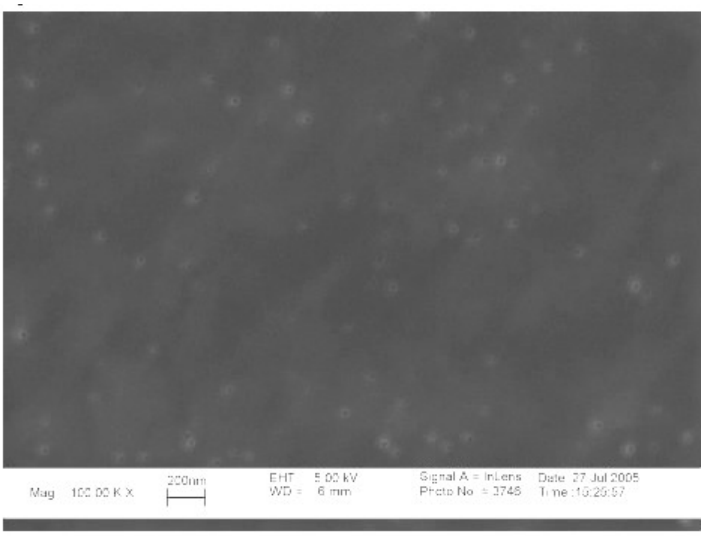

Figure 1.3 SEM image of TEPCM. Note that the pore density is low, and spacing between pores is large.

BCPs have two or more chemically distinct polymers connected end-to-end. If the constituent polymers are immiscible, and the volume fraction of the minor component is ~ 30% v/v, the minor component will self assemble to form cylindrical domains in a matrix of the major polymer fragment.[65-67] To obtain BCP nanoporous films, the minor component is etched out chemically,[68] photo-chemically (UV irradiation)[69] or thermally.[70] Nanoporous membranes fabricated from BCP has a higher pore density and a narrow pore size distribution, compared to

TEPCM (Figure 1.4), and their pre size is tuned by choosing an appropriate molecular weight.[65, 66] BCP derived nanoporous films are ideal for many applications due to their ordered nano scale structure and high surface area. Many of these applications depend on vertical domain orientation and interactions (specific, non-specific adsorption and electrostatic interactions) between the analytes and nanoporous surface.[71] Thus control of domain orientation and surface functionalization are key factors for many applications of BCPs.

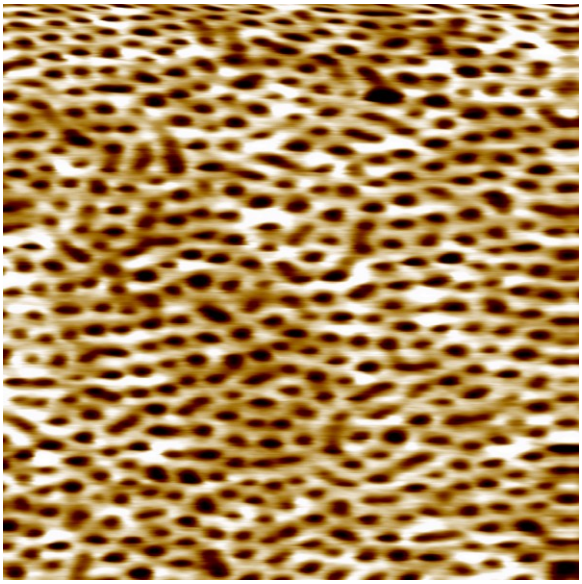

Figure 1.4 AFM image (contact mode, 1 x 1 µm, 1024 pixels, Z scale = 7nm) of etched PS-b-PMMA nanoporous film (image taken in 0.1M phosphate buffer).

Micro domains in BCP, self organize into a configuration that minimizes the free energy of the system. For thin BCP films, thickness as well as the interactions between the substrate and the each block determines the orientation of domains (parallel or perpendicular). This means that the block having the lower interfacial energy with the substrate will preferentially wet the substrate while, the block with lower surface energy will be confirmed at the free surface. This arrangement leads to domain orientation parallel to the substrate.[72-76] Vertical domain orientation can be achieved by controlling solvent evaporation conditions,[77, 78] solvent annealing,[79, 80] optimizing film thickness,[81, 82] applying an electric field during annealing,[83, 84] adding homo-polymers (for PS-b-PMMA)[85] and surface modification(chemically modify the surface in order to balance the affinities of BCP fragments to the substrate).[86, 87] Surface chemistry of BCP can be controlled by two methods. One method is to synthesize BCP that offers known functional

groups (such as –COOH) upon formation of nano-pores via etching.[68, 71, 88, 89] Hillmyer et.al. synthesized BCP having PLA (poly lactic acid) as the minor component, which upon hydrolysis (chemical etching) offered –COOH groups on the nanopore surface. They modified the surface functional groups via esterification[68] and amidation.[71] The other method is to functionalize the surface functional groups that result etching the minor component.[90] Applications of monolithic BCP includes masks in lithography,[91, 92] templates for electrophoretic deposition of nano particles,[93, 94] templates for nano wires (Si and metal),[84, 95, 96] ultra low di-electric constant materials for high density circuits,[97] filtration membranes for viruses[98, 99] and size based separations.[100, 101]

1.3.3 Electrode Kinetics[102-104]

Reactions at the electrodes are important factor in practical electrochemical systems. When describing an electrochemical reaction major consideration is given to the reaction rate, which is related to the current density.

$$\text{Rate} = i/nFA = j/nF \qquad (1.2)$$

where i is current (A), j is the current density (A/cm^2), F is Faraday's constant (= 96485 C/mol) and n is the number of electrons. Rate of a reaction is dependent on

i) Nature of the electrode

ii) Composition of the electrolyte solution adjacent to the electrode surface (double layer structure).

iii) Electrode potential which is characterized by the over potential (deviation of the electrode potential from the equilibrium potential when a Faradaic current flows through the system.

1.3.3.1 Electrical Double Layer

The interface between the electrode and the adjacent solution behaves as a capacitor. Which means at any given potential, there will be a charge q^m on the electrode and charge q^s in the solution. At all the times $q^m = q^s$. The arrangement of charged species on the electrode surface, and the cations or anions in the solution, and the dipoles present at the electrode surface – solution interface is known as the electrical double layer (Figure 1.5).

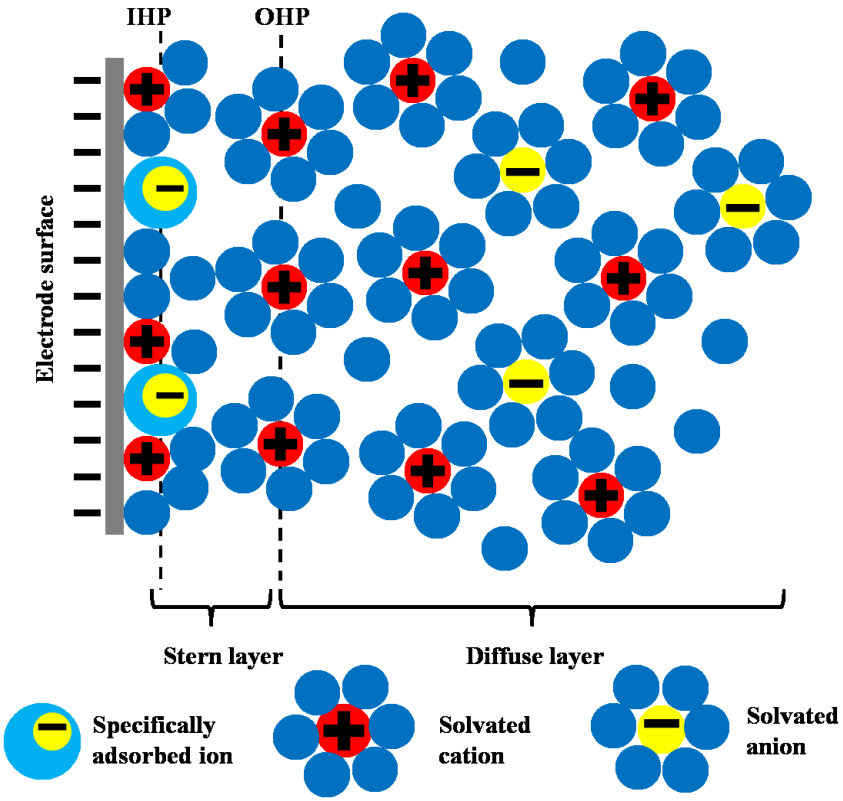
IHP
OHP
Electrode surface
Stern layer
Diffuse layer
Specifically adsorbed ion
Solvated cation
Solvated anion

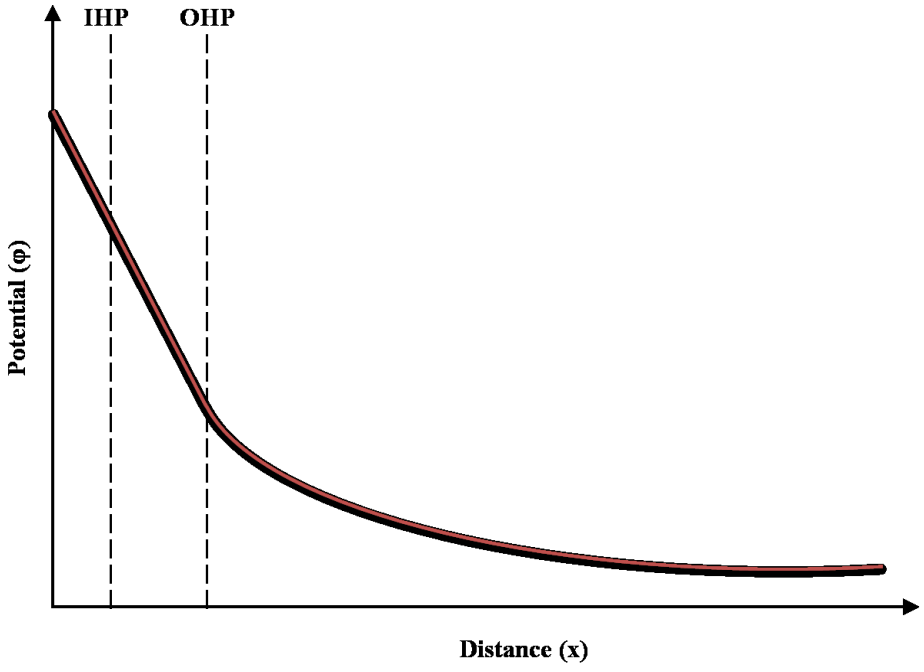
IHP
OHP
Potential (φ)
Distance (x)

Figure 1.5 Schematic diagram of the electrical double layer for a negatively charged electrode surface. Stern layer boundaries are Inner Helmholtz plane (IHP) and Outer Helmholtz plane (OHP). Diffuse layer bound by OHP and the bulk solution. Potential profile in each layer is given as a function of distance from the electrode surface.

The electrical double layer is composed of several layers. The layer adjacent to the electrode surface has specifically adsorbed solvent molecules and other species (cations/ anions). This is the compact/ Helmholtz / Stern layer. Composition of the ions in the inner layer is determined by electrostatic interactions. This inner layer is divided into two parts, inner Helmholtz plane (IHP) and outer Helmholtz plane (OHP). The thickness of the IHP is defined by the distance between the electrode surface and the center of the electrical centers of specifically adsorbed ions after they lose their salvation shell. The total charge density of IHP is σ_i. Outer Helmholtz plane has solvated ions and they can approach the electrode surface only upto a distance of x (due to their salvation shells). Diffuse layer is adjacent to the OHP and it extends upto the bulk solution, and contains non-specifically adsorbed ions. This layer has a charge density of σ_d. According to this model, the electro-neutrality of the electrode – solution interface at equilibrium is maintained by balancing the charge on the metal, σ_m and charge on the solution side interface, σ_s. (eq. 1.3)

$$-\sigma_m = \sigma_s = \sigma_i + \sigma_d \qquad (1.3)$$

1.3.3.2 Gouy-Chapman- Stern model of electrical double layer (EDL)

This model is a combination of Gouy-Chapman model and the Helmholtz model of EDL. It assumes that (1) the diffuse double layer is in equilibrium with the bulk solution, (2) the solution is divided into laminae, parallel to the electrode surface with thickness x, and all laminae are in thermal equilibrium with each other (3) these laminae are treated as energy states with equivalent degeneracies. Concentration of ionic species in two laminae is determined by the Boltzman factor.

According to this model, the potential profile in the diffuse layer for 1:1 electrolyte is given by,

$$\tanh(ze\varphi/4kT) / \tanh(ze\varphi_2/4kT) = e^{-K(x-x2)} \qquad (1.4)$$

Where φ is the potential measured with respect to the bulk solution (potential drop across the double layer) and φ_2 is the potential at x_2 (OHP) w.r.t. the bulk solution. κ is the inverse of Debye length given by,

$$\kappa = (2n^0z^2e^2 /\varepsilon\varepsilon_0kT)^{1/2} \quad (1.5)$$

Where n^0 is the concentration of the electrolyte, T is the temperature (= Kelvin), k is the Boltzman constant (= J/K), z is the charge on the supporting electrolyte ion, ε is the di-electric constant of the solution, ε_0 is the permittivity of free space (= 8.85 X 10^{-2} F/m). For low concentrations of electrolytes used, the thickness of the electrical double layer will be higher. With th separation of charge, there is a potential drop across the double layer. The charge density at any point from the surface of the electrode to OHP is zero. As a result the potential drop is linear in the compact layer. All the charge in the solution side is accumulated in the diffuse layer; therefore the potential at the OHP is related to the electrode surface charge, σ_m by eq. 1.6.[102]

$$\sigma_m = -\sigma^s = (8RT\varepsilon\varepsilon_0C)^{1/2} \sinh(zF\varphi_2 /2RT) \quad (1.6)$$

1.3.3.3 Effect of double layer on electrode kinetics

In the work discussed in chapter 3, the surface charge of the SAM modified electrode was varied according to the pH of the medium. The surface density, σ of the TA monolayer is given by,[105]

$$\sigma = - (FK_a\Gamma_{COOH.\ total}) / ([H+] + K_a) \quad (1.7)$$

Where F is the Farady's constant (= 96485 C/mol), K_a is the apparent acid dissociation constant of the surface –COOH groups, $\Gamma_{COOH.\ total}$ is the density of TA on the electrode surface, and $[H^+]$ is the proton concentration in the solution. Protonation / deprotonation of surface –COOH groups leads to variation in surface charge density, thus affecting the potential at OHP (equation 1.6).[106, 107] This means when the electrode surface has a negative charge ($q^m < 0$, $\phi_2 < 0$), anions will be repelled and cations will be attracted and vice versa for the positively charged electrode ($q^m > 0$, $\varphi_2 > 0$). As a result, the distribution of ionic species at the electrode surface will be changed due to electrostatic interactions. Furthermore the potential driving the electrode reaction will no longer be $\varphi^m - \varphi^s$, instead it will be $\varphi^m - \varphi^s - \varphi_2$. The resulting effective electrode potential is now $E - \varphi_2$. The decrease of the electrode potential/ or the driving force of

electron transfer and the change in the distribution of ions at a charged electrode surface affect reaction kinetics, and this effect is known as the Frumkin effect. This alters the reaction kinetics of the electrochemical reaction. Studies have shown a similar effect on k^0 (rate constant at bare electrode) due to electrolyte concentrations altering the electrical double layer charge distribution.[108] In this research, the surface charge density, σ of TA monolayer was determined to assess the potential φ_2 at OHP of SAM coated microelectrode. The modified φ_2 was used to determine the k^0_{eff} at each pH condition by using the equation 1.8.[102, 108, 109]

$$k^0_{eff} = k^0 \exp[(\alpha - z_{red}) F \varphi_2 / RT] \quad (1.8)$$

k^0_{eff} and k^0 are rate constants of the reaction at a charged and a bare electrode respectively. Z_{red} is the charge of the electroactive species, φ_2 (V) is the potential at the OHP, r is the gas constant (= 8.31 J/K.mol). The exponential term in this equation is the Frumkin correction factor, used to determine the true rate constant. Previous studies have reported other processes involved in charge propagation and electrode kinetics on SAM modifies electrodes. These studies described "inversion of the apparent surface charge, when a highly charged marker ion covers the SAM surface leading to coordination of oppositely charged ions in a second coordination layer.[110, 111] Qualitative discussions on cyclic voltammetry studies of $Fe(CN)_6^{3-/4-}$ on a TA modified microelectrode has been reported (at pH 7.4 and 1.5).[112] The research presented here discusses the reaction kinetics on a charged electrode based on Frumkin effect as well as extracted k^0_{eff} using closed form equations.

1.3.4 Surface charge on nanoporous membranes[113-115]

Nano scale pores in TEPCM gives larger surface area to volume ratios. This means that a considerable amount of surface charge is immobile. In addition, adsorption of ions/ molecules changes the surface charge and hence the potential distribution, which affect the permeability of charged analytes through nanopores.[116] In assessing the surface charge of nanopores, zeta potential is used in many cases. This is the potential of the surface at the plane of shear (an imaginary plane between the solid surface and the adjacent fluid). It is useful in characterizing the outer diffuse double layer and interactions between the analytes and the nanopore surface. Calculation of zeta potential in nanopores is based on measurements of streaming potential, electro-osmosis (primary electrokinetic effects – measurements of electrical / hydrodynamic

quantity) and electro-viscous effect and salt retention in membranes (secondary electrokinetic measurements – measurements of flux and salt retention).[117]

1.3.4.1 Streaming Potential

When a hydrostatic pressure is applied to a porous membrane (use of a pressure gradient) the flow of liquid will drag / strip off part the charges / ions present in the double layer to one end of the pore. This generates a streaming current, I_s. Dragging of the charges by the fluid flow will cause a potential drop across the membrane. This potential drop will create a conduction current of co-ions (I_c) in opposite direction of the fluid flow. A steady state is achieved when the streaming current balances out the conduction current. The electrostatic potential at this steady state is called the streaming potential (Figure 1.6). It is measured as a function of applied pressure. Zeta potential can be calculated from the measured streaming potential by,

$$\zeta = (\Delta E_s / \Delta P) \cdot (\eta \lambda_0 / \varepsilon \varepsilon_0) \qquad (1.9)$$

Where ΔEs is the potential drop at the end of the pore, ΔP is the pressure gradient, η is the viscosity of the electrolyte solution, λ_0 is the specific conductivity of the electrolyte within the pores, ε is the relative dielectric constant of the electrolyte and ε_0 is the permittivity of free space. However above equation cannot be applied for nano scale pores or highly charged pores without using some corrections. In nano scale pores, the overlapping of double layers especially in low electrolyte concentrations, result in uniform potential distribution throughout the pore. In the case of highly charged surface, both the fixed part of the double layer and the electrolyte (both factors taken together termed the surface conductivity) contributes to the electrical conductivity. To adjust for these factors, ohmic resistance of the pore is measured with pores filled with the test solution and subsequently when pores are filled with highly concentrated electrolyte to neglect the surface conductance.[113, 118] Zeta potential is then given by,

$$\zeta = (\Delta E_s \eta / \Delta P \, \varepsilon \varepsilon_0) \cdot (\lambda_h R_h / R) \qquad (1.10)$$

Where λ_h is the specific conductivity of highly concentrated electrolyte, R_h and R are the corresponding ohmic resistance of the highly concentrated electrolyte solution and the test solution respectively.

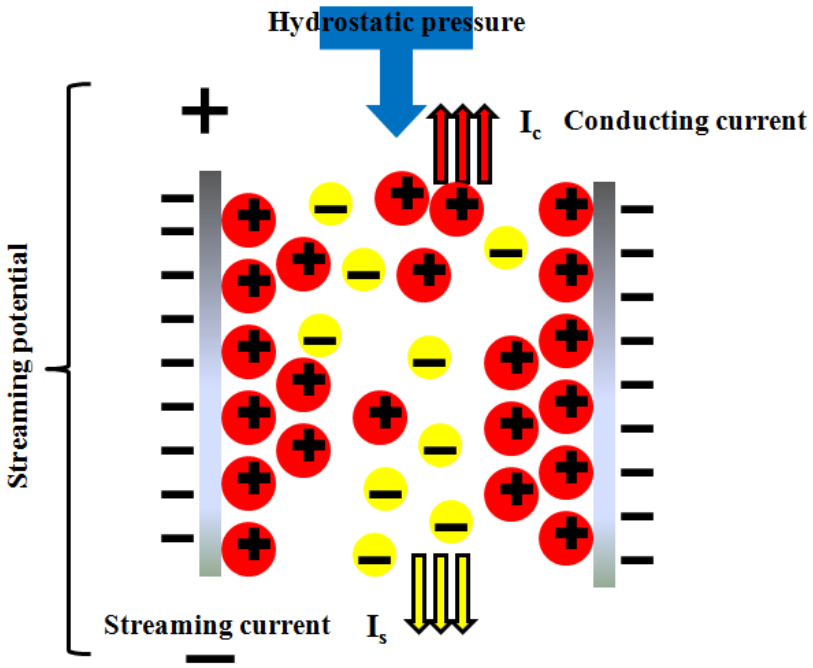

Figure 1.6 Schematic diagram of streaming potential in a nanopore.

1.3.4.2 Electroviscous effects

Electro-viscous effect is defined as the increase in apparent viscosity over bulk viscosity of a solution. This effect arises from influence of electrical double layer on the flow of a fluid. When an electrolyte is flowed through a pore, under a pressure gradient, a streaming potential is generated. This will cause a back flow of fluid by electro-osmotic effect. Then the fluid shows increased viscosity compared to the flow in the absence of a double layer. Electro viscous effect for a nanopore can be determined by the following equation.[113]

$$\eta_a = \eta / [1-(3(\varepsilon\zeta)^2) / (h^2\, \eta\lambda_0)] \qquad (1.11)$$

where η and η_a are bulk and apparent viscosity of the solution, ε is the dielectric constant of the solution, ζ is the zeta potential, λ_0 is the solution conductivity and h is the pore length. Previous studies have shown the use of electro viscous measurements to determine the sign of zeta potential of polycarbonate membranes.[117] For negatively charged membranes, increase in the viscosity will be higher if there is a large difference between the cation and the anion nobilities. This indicates that the electro-viscous behavior within a pore is determined by the interaction between counter ions and the charge of the nanopore surface.

Streaming potential was used in determining zeta potential to assess the surface charge of polycarbonate membranes. In this method streaming potentials were measured at different pressures and zeta potential was determined from the slope of the graphs of ΔE_s vs. ΔP. This study discussed the effect of pH on zeta potential for membranes with different pore sizes. Use of permeation flow and tangential flow allowed to differentiate between the pore size effects of zeta potential since the latter mode of flow is independent of the pore size.[118]

Furthermore the surface charge has been assessed by flow of fluorescent molecules by applying an electric field to manipulate the transport of neutral and charged ions.[116, 119] When there is no applied field the fluorescent probe transport through the nanopores of TEPCM was driven by a concentration gradient. In the presence of an electrolyte, the membranes possess a negative charge due to anion adsorption on the surface of nanopores. This indirectly states that the membranes have a positive charge in contrast to the earlier studies. These studies suggest that the origin of surface charge of a solution filled nanopores is functional groups developed from membrane processing or the adsorption of ions from the electrolyte solution.[116, 118-120]

1.3.5 Responsive behavior of polymers to external stimuli

Polymeric materials have been incorporated into sensors for due to many advantageous features they offer. They are inexpensive materials and can be fabricated by low cost techniques. These materials can be deposited on various substrates and they offer a variety of functionalization possibilities such as addition of side chains, incorporation of charged or neutral chemical moieties in the bulk medium or on the surface.[121] Polymeric materials used in these sensors include hydro-gels, polymer beads, poly-electrolytes, permselective membranes, polymer brushes, ionic polymers, and optically sensitive polymers. These materials are signal responsive because they change or tune their properties such as structural alignment, shape or dimensions,[122] electrochemical,[123] optical,[124, 125] magnetic,[126] permeability,[127] mechanical,[128] and wetting/ adhesion[129] upon receiving chemical or physical stimuli. Response to external stimuli of these polymer materials are categorized into several groups such as optical, electrochemical, thermal, mechanical etc. Table 1.2 summarizes the types of sensors based on polymeric materials and the measured parameters of these sensors.

Table 1.1 Types of sensors based on polymeric materials and the measured parameters.

Types of sensors	Measured parameter
Electrochemical	Cell potential / Conductivity/ Current
Optical	Light scattering/ changes in refractive index/ adsorption or emission properties of the material
Calorimetric	Change in temperature
Semiconductor	Diode characteristics/ threshold voltage
Impedance	Capacitance / resistance
Mechanical	Elasticity / Flexibility
Chemical	pH / salinity
Biosensors	Enzyme / immune reactions

1.3.5.1 Sensors based on polymer swelling

This type of sensors is fabricated immobilizing stimuli responsive polymers on a suitable substrate. These polymers undergo swelling and shrinking according to the external stimuli they are exposed. However these sensors suffer from delamination of the polymer film due to swelling and shrinking, which leads to severing of covalent bonds between the polymer and the substrate. These drawbacks have been addressed to fabricate more stable sensors by adding a toughening agent, cross linking or preparing membranes containing porous polymer pores in a hydrogel membrane.[130] Optical properties of polymers change when external stimuli are applied, and these changed are coupled to optical sensing component to fabricate sensors. A sensor for pH has been fabricated by casting microspheres of lightly cross linked nitrated poly(4-hydroxystyrene) into hydrogel membranes. This sensor is sensitive to pH at wave lengths corresponding to swelling.[131] Sensors have been made by coupling fiber optics to polymer swelling. A fiber optic sensor was fabricated from sulphonated polystyrene polymer which is sensitive to salt concentrations. As the ionic strength of the solution increase, polymer membrane shrinks, causing the reflecting diaphragm to move (PS polymer is coupled to a reflector), changing the intensity of light reflected back into the optical fiber.[132] Other sensors based on

polymer swelling include dicarboxylated polymer particles that respond to pH,[133, 134] Copper and Ca^{2+} ions,[135] glucose,[136, 137] salinity in water,[124] chloride detection[138] have been reported.

1.3.5.2 Polymer swelling

Swelling of polymers on application of external stimuli has been used in chemical sensing. Crosslinked polymers swell in the presence of a suitable solvent, and this leads to changes in the optical parameters of the polymer.[130, 139] Polymer swelling occurs when the solvent molecules diffuse into the crosslinked polymer and dilutes the bulk polymer. This process is called salvation and it is driven by temperature. The chains of polymer elongate to accommodate the volume change, and as a result, elastic retractive forces are generated to oppose deformation of the polymer. When these forces are balanced the equilibrium state is reached. The degree of swelling is dependent on the affinity of the polymer to the solvent, and for ionic polymers electrostatic repulsion between the neighboring groups also contributes to swelling.[130, 140] According to Flory and Rehner swelling of a polymer is described by two terms. These two terms are elastic free energy term and polymer solvent mixing free energy term.[141] They expressed the swelling of a polymer as,

$$\ln a_s = \ln v_s + v_p + v_p^2 \chi_s + V_s \xi (v_p^{1/3} - v_p/2) \qquad (1.12)$$

where a_s is solvent activity, v_s and v_p are volume fraction of solvent and polymer respectively, χ_s is Flory interaction parameter, V_s is solvent molar volume, and ξ is number of cross linking points.

According to equation 1.12, cross linking density is a determining factor of swelling of polymers. Magnitude of swelling can be determined by considering the volume changes of a polymer in a dried state and a saturated state with the solvent. Usually this is expressed as volume (in mL) of solvent adsorbed per gram of polymer.[142]

$$S = [(W_s - W_0)/ d - V_0] / xW_0 \qquad (1.13)$$

Where S is the volume in mL of solvent adsorbed per gram of polymer, W_s and W_0 are the weights of polymer saturated with solvent and dried state respectively, V_0 is the void volume of the polymer, d is the density of the solvent and x is the weight fraction of polymer.

To determine if a given solvent cause maximum swelling of a polymer, the swelling power of the solvent is used. It is related to the magnitude of swelling, S in the following equation.[140, 142, 143]

$$S = C\,(\lambda^{1/3} - \lambda_0^{1/3}) \qquad (1.14)$$

Where C is the swelling power for a given solvent, λ and λ_0 are the average number of atoms in the back bone of the polymer fragments and critical crosslinking density of the polymer. In terms of solubility parameters, swelling is maximum for a crosslinked polymer when $(\delta_{polym} - \delta_{solv})^2$ is zero.[144] Swelling of polystyrene in different solvent groups have been studied, and relative swelling power C, has been correlated to the solubility parameters. The major factor determining the swelling of PS has been the relative affinity of the functional group of the solvent. This affinity is reduced by the steric hindrance due to the substituent groups attached near the functional groups.[140, 143, 145] These studies have used polymer–solvent systems. In this research we investigated the swelling of PS-b-PMMA nanoporous films for polymer-solvent aqueous systems, where there is a possibility of solvent partitioning inside the nanopores. We compared the stability and permeability effect of solvents on PS brush and PS-b-PMMA nanoporous films (Figure 1.7). These comparisons will allow us to understand the how the BCP material behaves for external stimuli such as organic solvents and to optimize their applicability in electrochemical sensors.

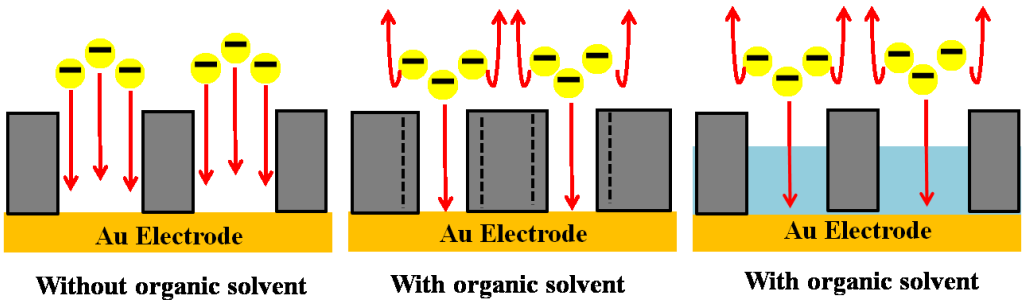

Figure 1.7 Schematic diagram showing permeability changes induced by organic solvent for a PS-b-PMMA nanoporous film on gold substrate.

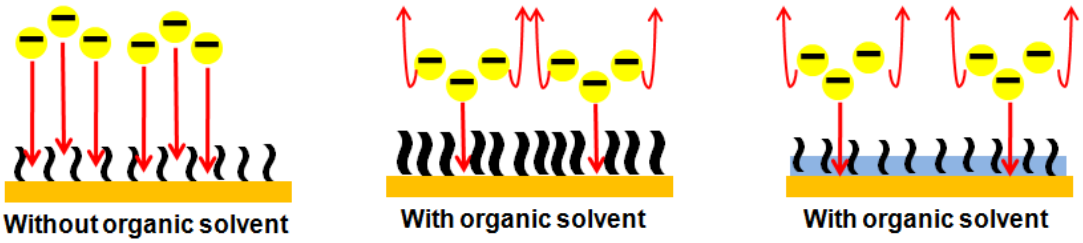

Figure 1.8 Schematic diagram showing permeability changes induced by organic solvent for a PS brush on gold substrate.

References

(1) Trojanowicz, M. In

Main Concepts of Chemical and Biological Sensing *;* Potyrailo, R. A., Mirsky, V. M., Eds.; *Combinatorial Methods for Chemical and Biological Sensors*; Springer: New York, 2009; Vol. 1, pp 25-60.

(2) Stradiotto, N. R.; Yamanaka, H.; Zanoni, M. V. B. *J. Braz. Chem. Soc.* **2003***, 14*, 159-173.

(3) Bakker, E.; Telting-Diaz, M. *Anal. Chem.* **2002***, 74*, 2781-2800.

(4) Bakker, E. *Anal. Chem.* **2004***, 76*, 3285-3298.

(5) Bochenska, M.; Guzinski, M.; Kulesza, J. *Electroanalysis* **2009***, 21*, 2054-2060.

(6) Arvand, M.; Asadollahzadeh, S. A. *Talanta* **2008***, 75*, 1046-1054.

(7) Pietrzak, M.; Meyerhoff, M. E. *Anal. Chem.* **2009***, 81*, 3637-3644.

(8) Lai, C.; Koseoglu, S. S.; Lugert, E. C.; Boswell, P. G.; Rabai, J.; Lodge, T. P.; Buhlmann, P. *J. Am. Chem. Soc.* **2009***, 131*, 1598-1606.

(9) Wang, J.; Tian, B.; Rogers, K. R. *Anal. Chem.* **1998***, 70*, 1682-1685.

(10) Ghindilis, A. L.; Skorobogat'ko, O. V.; Gavrilova, V. P.; Yaropolov, A. I. *Biosensors and Bioelectronics* **1992***, 7*, 301-304.

(11) Park, J.; Chang, B.; Nam, H.; Park, S. *Anal. Chem.* **2008***, 80*, 8035-8044.

(12) Prasad, K. S.; Arun, A. B.; Rekha, P. D.; Young, C. C.; Chang, J. L.; Zen, J. M. *Electroanalysis* **2009***, 21*, 1646-1650.

(13) Privett, B. J.; Shin, J. H.; Schoenfisch, M. H. *Anal. Chem.* **2010***, 82*, 4723-4741.

(14) Khan, M. A. K.; Kerman, K.; Petryk, M.; Kraatz, H. *Anal. Chem.* **2008***, 80*, 2574-2582.

(15) Zhang, B.; Adams, K. L.; Luber, S. J.; Eves, D. J.; Heien, M. L.; Ewing, A. G. *Anal. Chem.* **2008***, 80*, 1394-1400.

(16) Xu, H.; Zeng, L.; Xing, S.; Xian, Y.; Shi, G.; Jin, L. *Electroanalysis* **2008***, 20*, 2655-2662.

(17) Yantasee, W.; Hongsirikarn, K.; Warner, C. L.; Choi, D.; Sangvanich, T.; Toloczko, M. B.; Warner, M. G.; Fryxell, G. E.; Addleman, R. S.; Timchalk, C. *Analyst* **2008***, 133*, 348-355.

(18) Rico, M. Á. G.; Olivares-Marín, M.; Gil, E. P. *Talanta* **2009***, 80*, 631-635.

(19) Zou, L.; Zhang, Y.; Qin, H.; Ye, B. *Electroanalysis* **2009***, 21*, 2563-2568.

(20) Kim, Y.; Amemiya, S. *Anal. Chem.* **2008***, 80*, 6056-6065.

(21) Schreiber, F.; Polerecky, L.; de Beer, D. *Anal. Chem.* **2008***, 80*, 1152-1158.

(22) Shim, J. H.; Lee, Y. *Anal. Chem.* **2009***, 81*, 8571-8576.

(23) Shin, J. H.; Privett, B. J.; Kita, J. M.; Wightman, R. M.; Schoenfisch, M. H. *Anal. Chem.* **2008***, 80*, 6850-6859.

(24) Smyntyna, V.; Golovanov, V.; Kacˇiulis, S.; Mattogno, G.; Righini, G. *Sensors Actuators B: Chem.* **1995***, 25*, 628-630.

(25) Qu, W.; Meyer, J. U. *Meas. Sci. Technol* **1997***, 8*, 593-600.

(26) Maekawa, T.; Tamaki, J.; Miura, N.; Yamazoe, N. *J. Mater. Chem.* **1994***, 4*, 1259-1262.

(27) Rumyantseva, M. N.; Labeau, M.; Senateur, J. P.; Delabouglise, G.; Boulova, M. N.; Gaskov, A. M. *Materials Science and Engineering B* **1996***, 41*, 228-234.

(28) Fleischer, M.; Meixner, H. *Sensors Actuators B: Chem.* **1995***, 26*, 81-84.

(29) Umezewa, Y.; Aoki, H. *Anal. Chem.* **2004***, 76*, 320 A-326 A.

(30) Sugawara, M.; Kojima, K.; Sazawa, H.; Umezawa, Y. *Anal. Chem.* **1987***, 59*, 2842-2846.

(31) Moses, P. R.; Wier, L.; Murray, R. W. *Anal. Chem.* **1975***, 47*, 1882-1886.

(32) Odashima, K.; Kotato, M.; Sugawara, M.; Umezawa, Y. *Anal. Chem.* **1993***, 65*, 927-936.

(33) Nagase, S.; Kataoka, M.; Naganawa, R.; Komatsu, R.; Odashima, K.; Umezawa, Y. *Anal. Chem.* **1990***, 62*, 1252-1259.

(34) Xiao, K. P.; Buhlmann, P.; Umezawa, Y. *Anal. Chem.* **1999***, 71*, 1183-1187.

(35) Katayama, Y.; Ohuchi, Y.; Higashi, H.; Kudo, Y.; Maeda, M. *Anal. Chem.* **2000***, 72*, 4671-4674.

(36) Ito, T. *J Electroanal Chem* **2001***, 495*, 87-97.

(37) Murata, M.; Nakayama, M.; Irie, H.; Yakabe, K.; Fukuma, K.; Katayama, Y.; Maeda, M. *Analytical Sciences* **2001***, 17*, 387-390.

(38) Aoki, H.; Hasegawa, K.; Tohda, K.; Umezawa, Y. *Biosensors and Bioelectronics* **2003***, 18*, 261-267.

(39) Kurzatkowska, K.; Dolusic, E.; Dehaen, W.; Siero-Stoltny, K.; Sieron, A.; Radecka, H. *Anal. Chem.* **2009***, 81*, 7397-7405.

(40) Gadzekpo, V. P. Y.; Xiao, K. P.; Aoki, H.; Buhlmann, P.; Umezawa, Y. *Anal. Chem.* **1999***, 71*, 5109-5115.

(41) Gadzekpo, V. P. Y.; Bühlmann, P.; Xiao, K. P.; Aoki, H.; Umezawa, Y. *Anal. Chim. Acta* **2000***, 411*, 163-173.

(42) Aoki, H.; Umezawa, Y. *Analyst* **2003***, 128*, 681-685.

(43) Hou, Y.; Gochin, M. *Anal. Chem.* **2008***, 80*, 5924-5929.

(44) Perera, D. M. N.; Ito, T. *Analyst* **2010***, 135*, 172-176.

(45) Bigelow, W. C.; Pickett, D. L.; Zisman, W. A. *J. Colloid Sci.* **1946***, 1*, 513-538.

(46) Love, J. C.; Estroff, L. A.; Kriebel, J. K.; Nuzzo, R. G.; Whitesides, G. M. *Chem. Rev.* **2005***, 105*, 1103-1170.

(47) Chechik, V.; Stirling, C. J. M. In *Gold-thiol self-assembled monolayers;* Patai, S., Rappoport, Z., Eds.; The chemistry of organic derivatives of gold and silver; John Wiley & Sons Ltd: 1999; pp 551-640.

(48) Mandler, D.; Turyan, I. *Electroanalysis* **1996***, 8*, 207-213.

(49) Wink, T.; van Zuilen, S.J.; Bult, A.; van Bennekom, W.,P. *Analyst* **1997***, 122*, 43R-50R.

(50) Whitesides, G. M.; Laibinis, P. E. *Langmuir* **1990***, 6*, 87-96.

(51) Ito, T.; Perera, D. M. N. T. In *Analytical Applications of Block Copolymer Derived Nanoporous Membranes;* Pierce, D. T., Zhao, J. X., Eds.; Trace Analysis with Nanomaterials; WILEY-VCH Verlag GmbH & Co. KGaA: Weinheim, 2010; pp 341-358.

(52) Baker, L. A.; Jin, P.; Martin, C. R. *Crit. Rev. Solid State Mat. Sci.* **2005***, 30*, 183-205.

(53) Siwy, Z. *Adv. Funct. Mater.* **2006***, 16*, 735-746.

(54) Martin, C. R.; Nishizawa, M.; Jirage, K.; Kang, M.; Lee, S. B. *Adv Mater* **2001***, 13*, 1351-1362.

(55) Deen, W. M. *AIChEJ* **1987***, 33*, 1409-1425.

(56) Martin, C. R. *Science* **1994***, 266*, 1961-1966.

(57) Hulteen, J. C.; Martin, C. R. *J. Mater. Chem.* **1997***, 7*, 1075-1087.

(58) Ito, T.; Audi, A. A.; Dible, G. P. *Anal. Chem.* **2006***, 78*, 7048-7053.

(59) Ismagilov, R. F.; Ng, J. M. K.; Kenis, P. J. A.; Whitesides, G. M. *Anal. Chem.* **2001***, 73*, 5207-5213.

(60) Kuo, T.; Cannon, D. M.; Shannon, M. A.; Bohn, P. W.; Sweedler, J. V. *Sensors and Actuators A: Physical* **2003***, 102*, 223-233.

(61) Kuo, T.; Cannon, , Donald M.; Chen, Y.; Tulock, J. J.; Shannon, M. A.; Sweedler, J. V.; Bohn, P. W. *Anal. Chem.* **2003***, 75*, 1861-1867.

(62) Cannon, Donald M.; Kuo, T.; Bohn, P. W.; Sweedler, J. V. *Anal. Chem.* **2003***, 75*, 2224-2230.

(63) Fa, K.; Tulock, J. J.; Sweedler, J. V.; Bohn, P. W. *J. Am. Chem. Soc.* **2005***, 127*, 13928-13933.

(64) Gatimu, E. N.; Sweedler, J. V.; Bohn, P. W. *Analyst* **2006***, 131*, 705-709.

(65) Hillmyer, M. A. *Adv. Polym Sci.* **2005***, 190*, 137-181.

(66) Olson, D. A.; Chen, L.; Hillmyer, M. A. *Chemistry of Materials* **2008***, 20*, 869-890.

(67) Li, M.; Coenjarts, C. A.; Ober, C. K. *Adv. Polym Sci.* **2005***, 190*, 183-226.

(68) Zalusky, A. S.; Olayo-Valles, R.; Wolf, J. H.; Hillmyer, M. A. *J. Am. Chem. Soc.* **2002***, 124*, 12761-12773.

(69) Melde, B. J.; Burkett, S. L.; Xu, T.; Goldbach, J. T.; Russell, T. P.; Hawker, C. J. *Chemistry of Materials* **2005***, 17*, 4743-4749.

(70) Chung, C. M.; Lee, J. H.; Cho, S. Y.; Kim, J. G.; Moon, S. Y. *J Appl. Polym. Sci.* **2006***, 101*, 532-538.

(71) Rzayev, J.; Hillmyer, M. A. *J. Am. Chem. Soc.* **2005***, 127*, 13373-13379.

(72) Russell, T. P.; Coulon, G.; Deline, V. R.; Miller, D. C. *Macromolecules* **1989***, 22*, 4600-4606.

(73) Russell, T. P.; Menelle, A.; Anastasiadis, S. H.; Satija, S. K.; Majkrzak, C. F. *Macromolecules* **1991***, 24*, 6263-6269.

(74) Kim, H. C.; Russell, T. P. *Journal of Polymer Science Part B: Polymer Physics* **2001***, 39*, 663-668.

(75) Pickett, G. T.; Balazs, A. C. *Macromolecules* **1997***, 30*, 3097-3103.

(76) Singh, C.; Pickett, G. T.; Zhulina, E.; Balazs, A. C. *The Journal of Physical Chemistry B* **1997***, 101*, 10614-10624.

(77) Kim, G.; Libera, M. *Macromolecules* **1998***, 31*, 2569-2577.

(78) Fukunaga, K.; Elbs, H.; Magerle, R.; Krausch, G. *Macromolecules* **2000***, 33*, 947-953.

(79) Kim, S. H.; Misner, M. J.; Xu, T.; Kimura, M.; Russell, T. P. *Adv. Mater.* **2004***, 16*, 226-231.

(80) Xuan, Y.; Peng, J.; Cui, L.; Wang, H.; Li, B.; Han, Y. *Macromolecules* **2004***, 37*, 7301-7307.

(81) Fasolka, M. J.; Mayes, A. M. *Annual Review of Materials Research* **2001***, 31*, 323-355.

(82) Guarini, K. W.; Black, C. T.; Milkove, K. R.; Sandstrom, R. L. *J. Vac. Sci. Technol. B* **2001***, 19*, 2784.

(83) Thurn-Albrecht, T.; DeRouchey, J.; Russell, T. P.; Jaeger, H. M. *Macromolecules* **2000***, 33*, 3250-3253.

(84) Thurn-Albrecht, T.; Schotter, J.; Kastle, G. A.; Emley, N.; Shibauchi, T.; Krusin-Elbaum, L.; Guarini, K.; Black, C. T.; Tuominen, M. T.; Russell, T. P. *Science* **2000***, 290*, 2126-2129.

(85) Jeong, U.; Ryu, D.; Kho, D.; Kim, J.; Goldbach, J.; Kim, D.; Russell, T. *Adv Mater* **2004***, 16*, 533-536.

(86) Mansky, P.; Russell, T. P.; Hawker, C. J.; Pitsikalis, M.; Mays, J. *Macromolecules* **1997***, 30*, 6810-6813.

(87) Ryu, D. Y.; Shin, K. S.; Drockenmuller, E.; Hawker, C. J.; Russell, T. P. *Science* **2005***, 308*, 236.

(88) Bailey, T. S.; Rzayev, J.; Hillmyer, M. A. *Macromolecules* **2006***, 39*, 8772-8781.

(89) Klaikherd, A.; Ghosh, S.; Thayumanavan, S. *Macromolecules* **2007***, 40*, 8518-8520.

(90) Li, Y.; Ito, T. *Langmuir* **2008***, 24*, 8959-8963.

(91) Park, M.; Harrison, C.; Chaikin, P. M.; Register, R. A.; Adamson, D. H. *Science* **1997***, 276*, 1401-1404.

(92) Zschech, D.; Kim, D. H.; Milenin, A. P.; Hopfe, S.; Scholz, R.; Goring, p.; Hillebrand, R.; Senz, S.; Hawker, C. J.; Russell, T. P.; Steinhart, M.; Gosele, U. *Nanotechnology* **2006***, 17*, 2122-2126.

(93) Zhang, Q.; Xu, T.; Butterfield, D.; Misner, M. J.; Ryu, D. Y.; Emrick, T.; Russell, T. P. *Nano Letters* **2005***, 5*, 357-361.

(94) Bandyopadhyay, K.; Tan, E.; Ho, L.; Bundick, S.; Baker, S. M.; Niemz, A. *Langmuir* **2006***, 22*, 4978-4984.

(95) Kim, H. C.; Jia, X.; Stafford, C. M.; Kim, D. H.; McCarthy, T. J.; Tuominen, M.; Hawker, C. J.; Russell, T. P. *Adv Mater* **2001***, 13*, 795-797.

(96) Crossland, E. J. W.; Ludwigs, S.; Hillmyer, M. A.; Steiner, U. *Soft Mater.* **2007***, 3*, 94-98.

(97) Fu, G. D.; Yuan, Z.; Kang, E. T.; Neoh, K. G.; Lai, D.; Huan, A. *Adv. Funct. Mater.* **2005***, 15*, 315-322.

(98) Yang, S.; Ryu, I.; Kim, H.; Kim, J.; Jang, S.; Russell, T. *Adv Mater* **2006***, 18*, 709-712.

(99) Yang, S. Y.; Park, J.; Yoon, J.; Ree, M.; Jang, S. K.; Kim, J. K. *Advanced Functional Materials* **2008***, 18*, 1371-1377.

(100) Li, Y.; Ito, T. *Anal. Chem.* **2009***, 81*, 851-855.

(101) Uehara, H.; Kakiage, M.; Sekiya, M.; Sakuma, D.; Yamonobe, T.; Takano, N.; Barraud, A.; Meurville, E.; Ryser, P. *ACS Nano* **2009***, 3*, 924-932.

(102) Bard, A. J.; Faulkner, L. R., Eds.; In *Electrochemical Methods, Fundamentals and Applications;* Bard, A. J., Faulkner, L. R., Eds.; Wiley: New York, 2001; Vol. 2nd.

(103) Grahame, D. C. *Chem. Rev.* **1947***, 41*, 441-501.

(104) Grahame, D. C. *Annu. Rev. Phys. Chem.* **1955***, 6*, 337-358.

(105) Smith, C. P.; White, H. S. *Langmuir* **1993***, 9*, 1-3.

(106) Creager, S. E.; Weber, K. *Langmuir* **1993***, 9*, 844-850.

(107) Cheng, Q.; Brajter-Toth, A. *Anal. Chem.* **1995***, 67*, 2767-2775.

(108) Watkins, J. J.; White, H. S. *Langmuir* **2004***, 20*, 5474-5483.

(109) Burshtain, D.; Mandler, D. *J Electroanal Chem* **2005***, 581*, 310-319.

(110) Degefa, T. H.; Schön, P.; Bongard, D.; Walder, L. *J Electroanal Chem* **2004***, 574*, 49-62.

(111) Schön, P.; Degefa, T. H.; Asaftei, S.; Meyer, W.; Walder, L. *J. Am. Chem. Soc.* **2005***, 127*, 11486-11496.

(112) Cheng, Q.; Brajter-Toth, A. *Anal. Chem.* **1996***, 68*, 4180-4185.

(113) Hunter, R. J. In *Zeta Potential in Colloid Science Principles and Applications;* Ottewill, R. H., Rowell, R. L., Eds.; Academic Press, Harcourt Brace Javanovich Publishers.: 1981; .

(114) Hunter, R. J. In *Foundations of Colloid Science 2nd Ed.* Oxford University Press Inc.: New York, 2001; .

(115) Brij M. Moudgil, Pankaj K. Singh and Joshua J. Adler In *Surface Chemistry in Dispersion, Flocculation and Flotation;* Holmberg, K., Ed.; Handbook of Applied Surface and Colloid Chemistry, Volumes 1-2; John Wiley & Sons Ltd: 2001; Vol. 1-2, pp 219-232.

(116) Kuo, T.; Sloan, L. A.; Sweedler, J. V.; Bohn, P. W. *Langmuir* **2001***, 17*, 6298-6303.

(117) Huisman, I. H.; Prádanos, P.; Calvo, J. I.; Hernández, A. *J. Membr. Sci.* **2000***, 178*, 79-92.

(118) Lettmann, C.; Möckel, D.; Staude, E. *J. Membr. Sci.* **1999***, 159*, 243-251.

(119) Kemery, P. J.; Steehler, J. K.; Bohn, P. W. *Langmuir* **1998***, 14*, 2884-2889.

(120) Möckel, D.; Staude, E.; Dal-Cin, M.; Darcovich, K.; Guiver, M. *J. Membr. Sci.* **1998***, 145*, 211-222.

(121) Harsányi, G. *Sens Rev* **2000***, 20*, 98-105.

(122) Tokarev, I.; Orlov, M.; Katz, E.; Minko, S. *The Journal of Physical Chemistry B* **2007***, 111*, 12141-12145.

(123) Zheng, L.; Xiong, L. *Colloids Surf. Physicochem. Eng. Aspects* **2006***, 289*, 179-184.

(124) Cong, J.; Zhang, X.; Chen, K.; Xu, J. *Sensors Actuators B: Chem.* **2002***, 87*, 487-490.

(125) Zhang, L.; Langmuir, M. E.; Bai, M.; Rudolf Seitz, W. *Talanta* **1997***, 44*, 1691-1698.

(126) Lai, J. J.; Hoffman, J. M.; Ebara, M.; Hoffman, A. S.; EstournÃ¨s, C.; Wattiaux, A.; Stayton, P. S. *Langmuir* **2007***, 23*, 7385-7391.

(127) Motornov, M.; Sheparovych, R.; Katz, E.; Minko, S. *ACS Nano* **2008***, 2*, 41-52.

(128) Aggeli, A.; Bell, M.; Boden, N.; Keen, J. N.; Knowles, P. F.; McLeish, T. C. B.; Pitkeathly, M.; Radford, S. E. *Nature* **1997***, 386*, 259-262.

(129) Minko, S.; MÃ¼ller, M.; Motornov, M.; Nitschke, M.; Grundke, K.; Stamm, M. *J. Am. Chem. Soc.* **2003***, 125*, 3896-3900.

(130) Lavine, B. K.; kaval, N.; Westover, D. J.; Oxenford, L. *Anal. Lett.* **2006***, 39*, 1773-1783.

(131) Westover, D.; Rudolf Seitz, W.; Lavine, B. K. *Microchemical Journal* **2003***, 74*, 121-129.

(132) McCurley, M. F.; Seitz, W. R. *Anal. Chim. Acta* **1991***, 249*, 373-380.

(133) Zhang, L.; Langmuir, M. E.; Bai, M.; Rudolf Seitz, W. *Talanta* **1997***, 44*, 1691-1698.

(134) Zhang, L.; Seitz, R. *Analytical and Bioanalytical Chemistry* **2002***, 373*, 555-559.

(135) Shakhsher, Z. M.; Odeh, I.; Jabr, S.; Rudolf Seitz, W. *Microchimica Acta* **2004***, 144*, 147-153.

(136) Kataoka, K.; Miyazaki, H.; Bunya, M.; Okano, T.; Sakurai, Y. *J. Am. Chem. Soc.* **1998***, 120*, 12694-12695.

(137) Asher, S. A.; Alexeev, V. L.; Goponenko, A. V.; Sharma, A. C.; Lednev, I. K.; Wilcox, C. S.; Finegold, D. N. *J. Am. Chem. Soc.* **2003***, 125*, 3322-3329.

(138) Grossman, B. G.; Yongphiphatwong, T.; Sokol, M. *Optics & Laser Technology* **2005***, 37*, 217-223.

(139) Mönch, W.; Monch *Appl. Phys. Lett.* **2006***, 89*, 164104.

(140) Errede, L. A. *Macromolecules* **1986***, 19*, 1522-1525.

(141) Flory, P. *J. Chem. Phys.* **1943***, 11*, 521.

(142) Errede, L. A. *J. Appl. Polym. Sci.* **1986***, 31*, 1749-1761.

(143) Errede, L. A. *Macromolecules* **1986***, 19*, 1525-1528.

(144) Gee, G. *Trans. Faraday Soc.* **1946***, 42*, 585-598.

(145) Errede, L. A. *J. Phys. Chem.* **1989***, 93*, 2668-2671.

Chapter 2 - Analytical Techniques Used in This Research

2.1 Introduction

Nanoporous (Track Etched Polycarbonate) membranes, PS-b-PMMA films and Self Assembled Monolayer coatings prepared in this research were characterized by several analytical techniques. Thickness of the sputter coated thin gold layer was measured by stylus profilometer. Spectroscopic ellipsometry was used to measure the thickness of PS-b-PMMA films spin cast on gold coated Si wafer at three stages, viz. before annealing the films, before and after etching of PMMA domains. Cyclic voltammetry (CV) was used in assessing the active surface area of the electrodes fabricated from TEPCM and PS-b-PMMA nanoporous films on gold substrate. Diffusion modes of redox molecules in the nanoporous structures used in this research was determined from CV. Permeability change of redox molecules on a charged SAM modified electrode and surface charge of TEPCM were assessed by CV. Electrochemical Impedance Spectroscopy (EIS) was used to investigate the organic solvent induced permeability changes of redox molecules on PS-b-PMMA nanoporous films. To support the EIS data on permeability changes, Atomic Force Microscopy (AFM), contact mode was employed to obtain topographic images.

2.2 Ellipsometry[1, 2]

Spectroscopic ellipsometry is a non destructive method which uses elliptic polarization of light to measure the thickness of thin films. When an incident light beam hits on the sample and is reflected from its surface at a different angle than the incident angle, a phase shift occurs. This changes the ellipticity of the polarized light. Thus by analyzing the reflected light, a detailed picture of that material can be obtained. Elliptic polarization is defined by a phase shift Δ, and the amplitude of electric field; X and Y in x and y directions. For ellipsometric measurements, ratio of amplitudes X and Y is used, denoted by $\tan \Psi = X/Y$, where Ψ is the angle between X and Y.

Figure 2.1 shows the components of an ellipsometer which has a polarizer-compensator-sample-analyzer configuration. The arm bearing the polarizer- compensator emits an incident light beam with a known polarization state on the sample. Then according to the properties of the sample, incident beam's polarization is changed. The arm with analyzer and detector will detect the change in the polarization of the reflected beam of light. The change in polarization of incident light after reflection from the sample is given as a ratio between the polarization parallel to the plane of incidence (p-polarized) and perpendicular to the plane of incidence (s-polarized). See equation 2.1.

$$\rho = r_p / r_s = \tan \Psi e^{i\Delta} \qquad (2.1)$$

where ρ is the change of polarization or the ellipticity. The ratio r_p / r_s is expressed in terms of the phase shift Δ and Ψ which is the angle between the amplitude of electric field in X and Y.

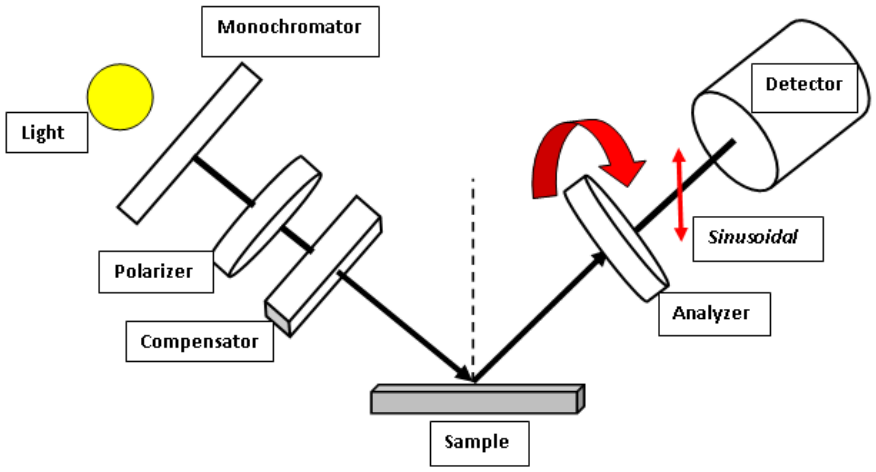

Figure 2.1 Schematic diagram of Polarizer- Compensator- Analyzer-Detector type ellipsometer.

Once an ellipsometric spectrum is generated for the film, analysis is carried out using a layer model to extract parameters such as film thickness and refractive index of the material. The model developed should have the correct layer sequence, and have guessed values for thickness of all layers, and refractive index. Then the unknown parameters are varied (thickness and refractive index) and Δ and Ψ values are calculated. This process is repeated till the mean square error is minimized between the calculated values of Δ and Ψ and the experimental spectra. When

the calculated and the experimental data match with a minimized mean square error, desired film parameters can be obtained.

2.3 Cyclic Voltammetry[3]

Cyclic voltammetry (CV) is a potential sweep method where potential is varied linearly with time at a constant sweep rate, to obtain a current – potential (i-E) curve. This technique is useful in discussing reversibility of a reaction, diffusion mode (linear or radial), diffusion constant (D_0) for a reactant, and estimation of "n" in an electrode reaction (n = number of electrons involved in the electrode reaction).In CV 3 dimensional i-t-E region is obtained by measuring the current passed between the working and counter electrode, by controlling the potential between working and the reference electrode. Figure 2.2 shows a typical CV obtained for a reversible, one electron reaction;

$O + e \rightarrow R$.

According to figure 2.2, when the scan begins at a positive potential, capacitive current flow for a certain time. When the potential is near $E^{0'}$ (formal potential of the electrode), Faradaic current begins to flow due to reduction of the species "O" (oxidized form). As the potential becomes more negative (closer to $E^{0'}$), the surface concentration of "O" decreases. This results in an increased flux and current. The peak around $E^{0'}$ is due to electrolysis of "O" near the electrode surface. Then the Faradaic current gradually decreases (after the peak), which reflects a decrease in the rate of arrival of "O" molecules to the electrode surface. When the potential scan is reversed towards a negative potential, the "R" (reduced form) begins to get oxidized (since the concentration of "R" is large on the electrode surface). As the potential approaches $E^{0'}$, a peak is begins to emerge due to oxidation of 'R"; giving rise to an anodic current. The choice of initial potential and the switching potential is important, and this requires knowledge of redox potential molecule used. The switching potential should be at least 35/n mV beyond the peaks in order to observe a clear peak in the reverse direction. Initial potential should be well chosen, so that there are no interfering electrode reactions occur at that potential.

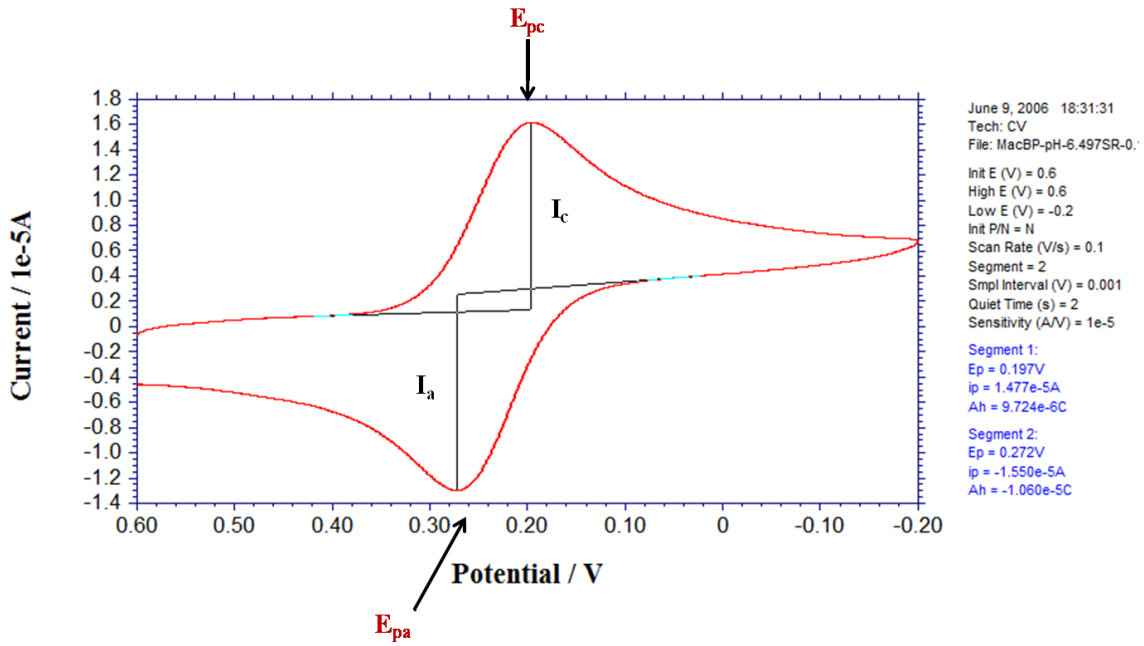

Figure 2.2 Cyclic voltammogram for macro bare gold disk electrode.

In this research, a three electrode cell set up consisting of a working electrode (micro / macro disk gold electrode, recessed nanoporous array electrode of either TEPCM (track etched polycarbonate membrane) or PS-b-PMMA film), a reference electrode (Ag/ AgCl, 3M KCl) and a counter electrode (Pt wire) was used. Depending on the scan rate and the working electrode type (nanopore electrode / micro/ macro disk electrode), the shape of the CVs obtained was different. This allowed investigating the diffusion mode of the redox molecules to the electrode surface.

For a macro electrode (bare gold disk electrode, d = 2mm), a reversible redox reaction gives a peak shaped CV (cyclic voltammogram), regardless of the scan rate. This is due to linear diffusion of the analyte to the electrode surface (Figure 2.3). The peak current i_p is dependent on $\nu^{1/2}$ (ν = scan rate in V/s).

$$i_p = (2.69 \times 10^5)\, n^{3/2}\, A\, D_0^{1/2}\, C_0^{*}\, \nu^{1/2} \qquad (2.2)$$

Where n is the number of electrons, A is the area of the electrode (cm^2), D_0 is the diffusion coefficient of the species "O" (= cm^2/ s), and C_0^{*} is the bulk concentration of "O" (mol/cm^3). Thus from a CV generated for a redox molecule at a macro electrode, above parameters can be extracted.

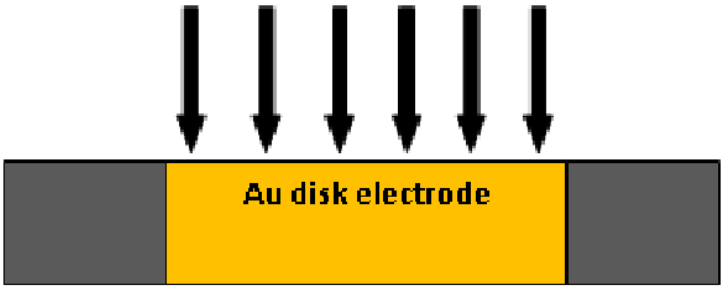

Figure 2.3 Schematic diagram showing linear diffusion of redox molecules to macro electrode surface. (Diffusion layer thickness δ << electrode size).

Microelectrodes exhibit a steady state behavior represented by a sigmoidal CV (except at very high scan rates) (Figure 2.4). At shorter time scales, the diffusion layer thickness is smaller, compared to the radius of the micro-disk electrodes (r_0). Thus the diffusion becomes linear. At longer time scales (slower scan rates), when the diffusion layer thickness grows larger than the electrode size, a steady state is reached given by a sigmoidal CV. This type of CV is obtained when the radial diffusion is dominant.

Unlike for a macro electrode, steady state current (limiting current, i_{lim}) at a micro-disk electrode is not dependent on the scan rate. Thus the limiting current i_{lim} is given as

$$i_{lim} = 4nFD_0C_0^*r_0 \qquad (2.3)$$

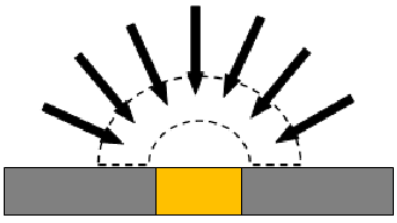

Figure 2.4 Schematic diagram showing radial diffusion of redox molecules to the micro electrode surface. (Diffusion layer thickness δ >> electrode size).

Recessed nanodisk array electrodes (RNE) were prepared from TEPCM or PS-b-PMMA films. Diffusion mode changes from linear to radial depending on the scan rate used. At higher scan rates, peak shaped CVs result from the diffusion of redox molecules within the nanopores. At slower scan rates, sigmoidal CVs are observed reflecting the radial diffusion of redox molecules outside the nanopores. In the case RNEs prepared from TEPCM, observation of steady state CVs (sigmoidal shape) at slow scan rates suggested that the spacing between the pores were large enough to prevent overlap of radial diffusion regimes from individual pores. In contrast, RNEs prepared from TEPCM, PS-b-PMMA films based RNEs showed peak shaped CVs at slower scan rates. This indicates the overlapping of radial diffusion regimes of individual nanopores due to close spacing between them. The following theoretical equations related to i_{lim} in a sigmoidal CV and i_p in a peak shaped CV on a RNE were used in determining pore density, diffusion coefficient ratios (Chapter 4) in this research.

$$i_{lim} = (4\pi nFC_sD_sa^2N) / (4L (D_s/D_p) + \pi a) \quad (2.4)$$

$$i_p = 0.446nF(N\pi a^2)C \sqrt{(nFD\nu)/ (RT)} \quad (2.5)$$

where n is the number of electrons, F is the Faraday's constant (= 96485 C/mol), a is the pore diameter, R is the gas constant (= 8.314J/Kmol), T is the temperature (= 298K), N is the total number of pores participating in the electrode reaction, L is the length of the pore (membrane / film thickness), C is the concentration of redox molecules in bulk solution (mol/cm^3), D_s and D_p are the diffusion coefficients of the redox molecules in the bulk solution and inside the pores respectively (cm^2/s). Figures 2.5 – 2.7 shows the diffusion modes for RNEs based on TEPCM and PS-b-PMMA films depending on the scan rate and pore spacing.

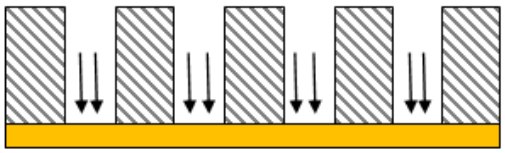

Figure 2.5 Schematic diagram of linear diffusion of redox molecules inside nanopores of a RNE.

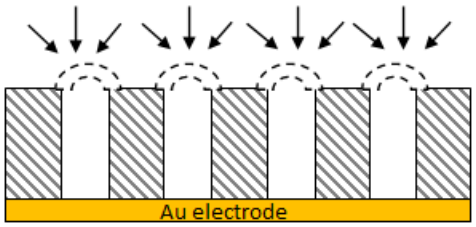

Figure 2.6 Schematic diagram of radial diffusion of redox molecules outside the nanopores of a RNE.

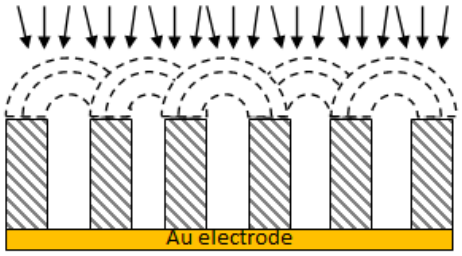

Figure 2.7 Schematic diagram of linear diffusion of redox molecules resulting from overlap of radial diffusion regimes of individual nanopores (pore spacing is closer)

2.4 Electrochemical Impedance Spectroscopy[3-5]

In this technique, impedance of a cell or electrode is measured as a function of frequency. Potential sweep, potential step or current step methods use a large perturbation to drive the electrode reaction far from the equilibrium, and observe a transient signal as the response. In contrast, electrochemical impedance uses a small excitation signal to observe how the system follows the given signal at a steady state. This is done by applying an AC potential to the electrochemical cell and measuring the current through the system. In a dc current, the ration between voltage V and current I, is given as resistance R (Ohm's law). Resistance is independent of frequency, and current and voltage are in phase with each other (no phase shift). (See figure 2.8)

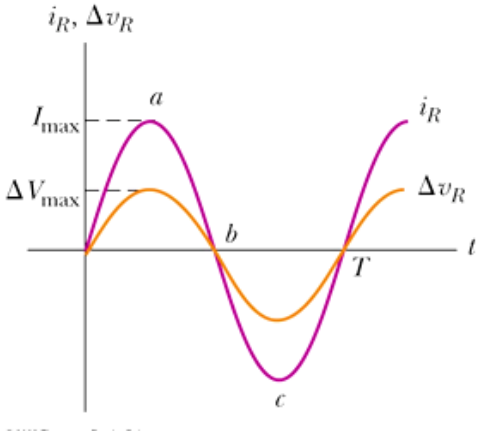

Figure 2.8 Voltage and current across a resistor in a dc circuit.
(https://rlphysicsinfo.wikispaces.com/file/view/Untitled8.png/33492809/Untitled8.png)

In an ac circuit, when a sinusoidal potential is applied $\Delta E \sin\omega t$ ($E = E_0 \sin(\omega t)$), the resulting current will also be sinusoidal with a phase shift of ϕ and a value $\Delta I \sin(\omega t + \phi)$ (resulting current $I = I_0 \sin(\omega t + \phi)$. The relationship between the applied voltage and resulting current in an ac circuit is known as impedance (Z). See figure 2.9.

$$Z = E/I = E_0 \sin(\omega t) / I_0 \sin(\omega t + \phi) \quad (2.6)$$

$$Z = Z_0 \sin(\omega t) / \sin(\omega t + \phi) \quad (2.7)$$

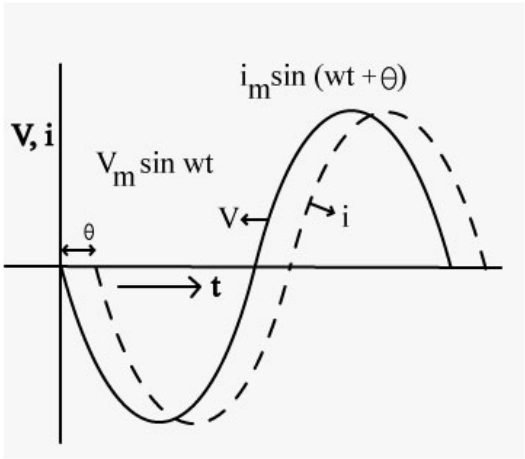

Figure 2.9 Relationship between ac current and voltage signal for a dc circuit. Phase shift for resulting current is ϕ. (http://www.epuniversity.org/tech/image/current-leading-voltage.jpg).

A common electrochemical system consists of resistors, capacitors and inductors. These should be considered when EIS data is analyzed by fitting the data into equivalent circuits. Application of a sinusoidal potential through a pure resistor with a value of R, will result in an impedance value equal to R, and a phase shift 0 at all frequencies (Figure 2.10). This means that a pure resistor does not have an imaginary part, thus the current resulting through the resistor will be in phase with the applied voltage across the resistor. In phasor notation this can be given as $\dot{E} = \dot{i} R$.

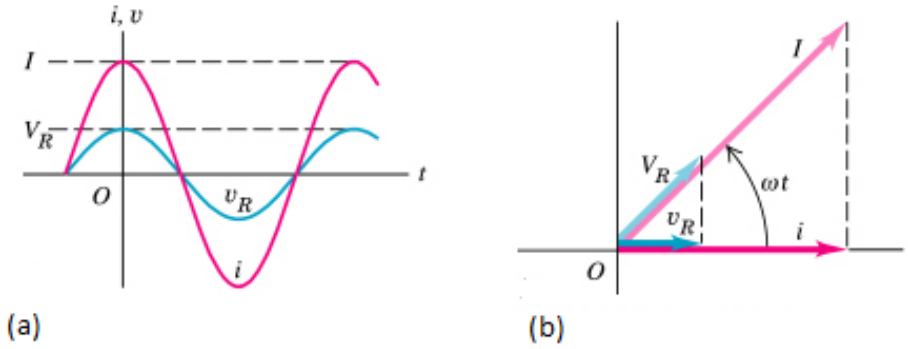

Figure 2.10 (a) Relationship between ac voltage across a pure resistor, and current through the resistor. (b) phasor diagram for the above circuit.
(http://www.physics.sjsu.edu/becker/physics51/images/32_03_Resistance%20phasor.JPG).

When a pure capacitor is used in place of resistor, the resulting impedance, Z is equal to $1/ j\omega C$ and the phase angle ϕ will be 90° (π /2) (see Figure 2.11). Unlike a resistor, a capacitor will have only an imaginary component. It is dependent on frequency and the current through the capacitor is phase shifted 90° w.r.t the applied voltage.

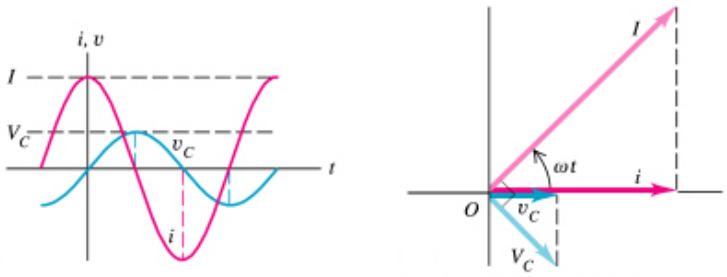

Figure 2.11 relationship between ac voltage across a pure capacitor and current through the capacitor. Right hand side phasor diagram for the above relationship. (http://www.physics.sjsu.edu/becker/physics51/ac_circuits.htm)

For an inductor, application of ac voltage results in an impedance (Z) equal to jωL, and a current which has a phase shift of (-) 90° w.r.t the applied voltage. The impedance of an inductor increases with the frequency (Figure 2.12).

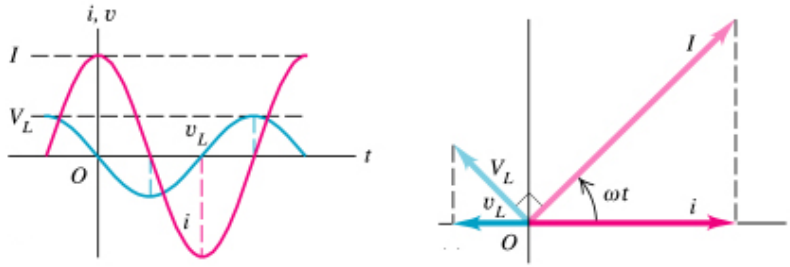

Figure 2.12 Relationship between ac voltage across an inductor and resulting current though the inductor. (http://www.physics.sjsu.edu/becker/physics51/ac_circuits.htm)

Variation of impedance with frequency is represented in Bode plots and Nyquist plots. In Bode plots, log $|Z|$ and ϕ (phase angle) is plotted against log ω (frequency). Nyquist plots are expressed as the imaginary (-Im Z) and the real (Re Z) parts of impedance.

Once the impedance spectra have been generated, parameters governing the electrochemical processes in a given system can be extracted by fitting the data according to Randle's equivalent circuit. In these circuits resistors and capacitors are connected parallel or in

series depicting each process in the electrochemical cell. Following types of equivalence circuits were used to fit data in this research (chapter 5).

2.4.1. Equivalence circuit for bare gold substrate electrode

The impedance spectra obtained from bare gold substrate electrode was fitted according to the following Randle's equivalent circuit (Figure 2.13)

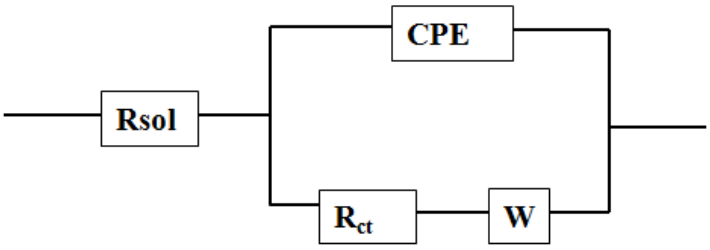

Figure 2.13 Randle's equivalent circuit for a bare gold substrate electrode.

In this circuit a constant phase element (CPE) was used instead of a capacitor. Capacitors in real cells does not behave ideally, thus use of CPE is more appropriate. Impedance of a capacitor is given as $Z = 1/ Cj\omega$, for a CPE it becomes $Z = 1/C (j\omega)^{-\alpha}$ where α is <1 for CPE ($0 < \alpha$) and equals 1 for a capacitor. In the above circuit, solution resistance due to electrolyte is given as R_{sol}. At high frequencies R_{sol} becomes independent of frequency, and is the intercept on the real impedance axis at the high frequency side. Charge transfer resistance, R_{ct} (polarization resistance at the formal electrode potential) is the kinetically controlled part of Faradaic impedance in a electrochemical reaction. This is due to the electron transfer across the electrode interface, by overcoming the polarization resistance. For a bare gold electrode, R_{ct} will be low, reflected by a less developed semi-circle due to fast kinetics. In contrast for a polymer film coated electrode, a well defined semi-circle is observed due to sluggish kinetics / higher R_{ct}. Warburg impedance (W) is the resistance to mass transport of the reactants. At higher frequencies, it becomes negligible because the distance that the reactants have to diffuse is less. However at low frequencies, it becomes significant since the reactants have to diffuse for long distances. In a Nyquist plot Warburg impedance is represented as a straight line with a slope equal to 1, and an angle of 45°, while in Bode plot it reflects a phase shift of 45 degrees.

2.4.2 Equivalence circuit for PS-b-PMMA film coated nanoporous electrode.[6-9]

For the PS-b-PMMA nanoporous film coated electrode the EIS data were fitted to a modified Randle's equivalent circuit (see Figure 2.14). This model incorporates the pore resistance (R_{pore}) and the capacitance of the polymer film $CPE_{polymer}$ (instead of a pure capacitor CPE is used). This model assumes that the redox molecules reach the electrode surface through open pores. In contrast to the bare gold substrate electrode, the charge transfer resistance is given as a well defined semi circle.

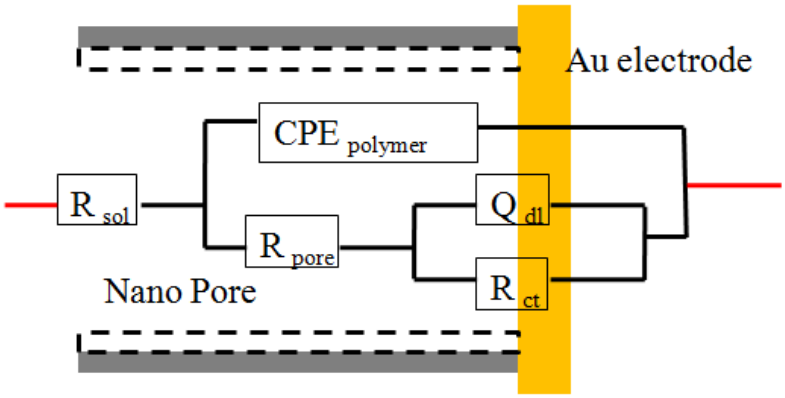

Figure 2.14 Randle's equivalent circuit for the PS-b-PMMA film coated electrode.

2.5 Atomic Force Microscopy[10-13]

In this research, contact mode AFM (Atomic Force Microscopy) imaging in solution phase was used to generate topographic images of PS-b-PMMA nanoporous films in the presence and absence of organic solvents. AFM can be considered as a combination of STM and stylus profiler. In contrast to STM (Scanning Tunneling Microscopy), AFM can be used for both conductive and non conductive samples whereas former can image only conductive samples in a vacuum. AFM is used vastly in surface characterization, imaging and determination of interaction forces between molecules / surfaces of interest. It is also advantageous over electron microscopy, since it can be used in air or solution phase.

AFM gives 3 dimensional images in x, y planes (horizontal) and z plane (vertical). To obtain images The AFM probe mounted at the end of a flexible cantilever is raster scanned across the sample surface to measure the atomic level forces between the tip and the surface. The

deflection of the cantilever arm is detected to build the topographic image of the sample. This is the basic technique of AFM imaging, and it is varied according to the sample to be imaged and the required information from an experiment. The basic components of an AFM is given in figure 2.15.

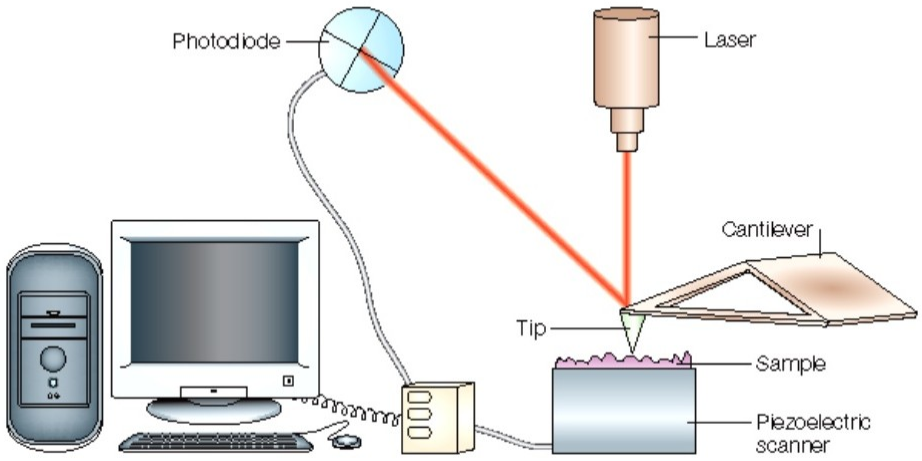

Figure 2.15 Components of AFM

(http://www.geobacter.org/research/nanowires/images/jpg/AFM_diagram.jpg)

AFM measures the forces between the sharp tip (usually made of Si_3N_4) and the sample surface. These forces deflect the cantilever according to Hooke's Law (equation 2.8).

$$F = -k\,x \qquad (2.8)$$

Where F is the elastic force (= N), x is the deflection of the cantilever (=m) and k is the spring constant of the cantilever (N/m). When taking the AFM image the tip will be moved relative to the sample by a piezo scanner. The cantilever chip or the sample itself can be mounted on the piezo crystal (tip scanning or surface scanning respectively). Direction of the scanning is referred to as z axis. Deflection of the cantilever as it moves along the surface will change the laser spot position on the quad photo detector, allowing monitoring the changes in deflection. In a typically a quadrant photo diode is used. This is divided into four parts with a horizontal and vertical line, and each quarter is labeled A to D. The deflection signal is calculated by (A + B) – (C + D) which gives the topographic data. (See figure 2.16). All these segments combine to give the sum of the signal. The measure of the cantilever deflection is given by the amplified

differential signal of the top two segments and the two bottom segments. By comparing the signal strength detected by A + C vs. B + D, lateral or torsional bending of the cantilever is possible.

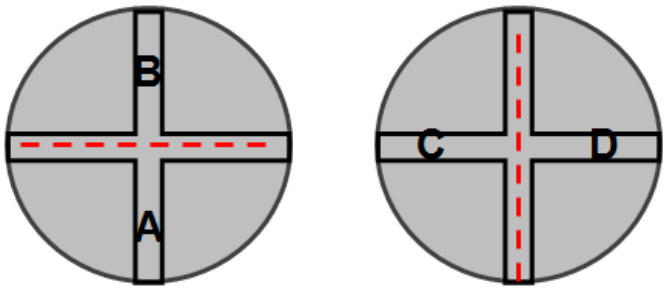

Figure 2.16 Quadrant photo diode detector used in AFM

The images of PS-b-PMMA nanoporous films in this research are generated by contact mode AFM. In this mode, the tip comes to contact with the sample at all the time. The repulsive forces between the probe and the sample generate the image, by applying a constant force or constant height. In constant force mode, the force of the cantilever deflection is kept constant. When the cantilever is deflected, the z height is adjusted to cause the tip to return to the original deflection. The change in z height is monitored and is used as a function of x and y directions to create the topographic image. In the constant height mode, the z height is kept constant and the deflection of the cantilever is used in generating the image.

References

(1) Tompkins, H. G.; Irene, E. A., Eds.; In *Handbook of Ellipsometry;* William Andrew Publishing/Noyes: 2005; .

(2) Mrstik, B. J.; McMarr, P. J.; Blanco, J. R.; Bennett, J. M. *J. Electrochem. Soc.* **1991***, 138*, 1770-1778.

(3) Bard, A. J.; Faulkner, L. R., Eds.; In *Electrochemical Methods, Fundamentals and Applications;* Bard, A. J., Faulkner, L. R., Eds.; Wiley: New York, 2001; Vol. 2nd.

(4) Chang, B.; Park, S. *Annual Review of Analytical Chemistry* **2010***, 3*, 207-229.

(5) Park, S.; Yoo, J. *Anal. Chem.* **2003***, 75*, 455 A-461 A.

(6) Macdonald, J. R., Ed.; In *Impedance Spectroscopy Emphasizing Solid Materials and Systems;* John Wiley & Sons, Inc.: 1987; .

(7) Scully, J. R.; Silverman, D. C.; Kendig, M. W., Eds.; In *Electrochemical Impedance Analysis and Interpretation;* ASTM: 1993; .

(8) Mansfeld, F. *Electrochim. Acta* **1993***, 38*, 1891-1897.

(9) Mansfeld, F. *Electrochim. Acta* **1990***, 35*, 1533-1544.

(10) Bowen, W. R.; Hilal, N., Eds.; In *Atomic Force Microscopy in Process Engineering - An Introduction to AFM for Improved Processes and Products;* Elsevier: 2009; .

(11) Drelich, J.; Mittal, K. L., Eds.; In *Atomic Force Microscopy in Adhesion Studies;* VSP - An imprint of BRILL: 2005; .

(12) Giessibl, F. J. *Materials Today* **2005***, 8*, 32-41.

(13) Kailash C. Khulbe, C.Y. Feng, Takeshi Matsuura. In ***Synthetic polymeric membranes characterization by atomic force microscopy****;* Springer Berlin Heidelberg: Berlin, 2008; .

Chapter 3 - pH dependent voltammetric response of micro disk gold electrodes modified with thioctic acid self assembled monolayers.

Reproduced by permission of Taylor & Francis Group.

Published as: Perera, D.M.N.T.; Nagasaka, S.; Ito, T. Supramolecular Chemistry, 2010, 22, 450-454. (DOI: 10.1080/10610278.2010.483736)

3.1. Introduction

Ion Channel Sensors (ICS) are electrochemical sensors that can determine the concentration of a redox inactive analyte. They are particularly desirable in detection of large hydrophilic ionic species having high charge numbers.[1] ICS employ electrodes modified with thin films of analyte selective binding moieties. Selective binding of analytes or substrates triggers changes in surface charge[2] and /or porosity of the films[3] which can be measured as changes in the redox current of electro-active markers added to the media (e.g. $Fe(CN)_6^{3-}$). Thus working principle of an ion channel sensor mimics ion channel proteins in biological membranes. Key advantages of ICSs are selective recognition of analytes and signal amplification. Selective binding of a small amount of analytes results in an electrochemical response caused by a larger number of electro-active species. Thus principle of signal transduction can be generally applied for electrochemical sensors designed for small ions and molecules,[2-10] to relatively large biomolecules.[11-14] ICSs can be classified into two types, based on their response mechanism. In one type, analyte molecules form inclusion type complexes with the substrate / receptors, physically block the intra-molecular channels. These ICSs are used in detection of neutral, redox inactive analytes, and response mechanism resembles ion channel proteins in biological membranes.[3] Charge based ICSs (CB-ICS) use electrostatic attraction or repulsion as the response mechanism. These exhibit voltammetric responses based on electrode surface charge changes, induced by analyte – substrate complexation. Binding of ionic analytes to the sensor surface induce large changes in surface charge of thin films, leading to large voltammetric responses for charged redox markers.[7, 11, 12]

This chapter reports our attempts to experimentally and theoretically investigate the voltammetric response of CB-ICSs, based on micro-disk electrodes. Understanding the response behavior of micro electrode based ICS is important for their future applications in *in-vivo* biological research,[15] array based sensor chips,[16] and detectors in micro fluidic devices.[17] Voltammograms at a micro-disk electrode can be theoretically described using closed form equations,[18-20] thus allowing us to analyze the experimental data quantitatively. Quantitative analysis based on a simple model was used to recognize the chemical processes that contribute significantly to the voltammetric responses of ICSs. Previous studies have reported various processes involved in voltammetric response of an ICS.[21, 22] This study focused only on investigating the simplest case of voltammetric response of CB-ICS; an ion channel sensor based on electrostatic repulsion. The voltammetric response of ICSs has been evaluated on the basis of the effects of electrode surface charge on electrode reaction kinetics; the Frumkin effect.[23, 24]

In this chapter we report the pH dependence of cyclic voltammograms (CVs) of $Fe(CN)_6^{3-}$ on micro-disk gold electrodes modified with thioctic acid (TA) monolayers. A TA modified electrode can be considered as a simple model system of an ICS based on electrostatic repulsion. Upon deprotonation at higher pH, the terminal –COOH groups of a TA monolayer offers a negative surface charge, which can be recognized by measuring the redox current of charged electro-active markers.[24-26] By using a negative redox marker ($Fe(CN)_6^{3-}$), we were able to simplify our theoretical simulation, because the voltammetric response arise from the diffusion of the redox marker, rather than ions adsorbed on the electrode surface.[21] Although CV's of $Fe(CN)_6^{3-}$ on a TA modified micro electrode at pH 1.5 and 7.4 were reported previously,[26] they were not discussed quantitatively using theoretical equations.

3.2. Materials and Methods

3.2.1Chemicals

All of the solutions were prepared with ultra pure water with a specific resistance greater than 18.0 MΩ cm (Barnstead Nanopure Systems, Dubuque, IA, USA). Potassium chloride (KCl; Fisher, Loughborough, UK), potassium hydroxide (KOH; Fisher), hydrochloric acid (HCl; Fisher), potassium dihydrogen phosphate (KH_2PO_4; Fisher), potassium hydrogen phosphate

(K_2HPO_4, Fisher), potassium hexacyanoferrate(III) ($K_3Fe(CN)_6$; Acros Organics, Geel, Belgium), and thioctic acid (TA; TCI) were of analytical grade and used as received.

3.2.2 Electrode Preparation and Electrode Measurements

A gold microdisk electrode (25 μm in diameter; CH Instruments, Austin, TX, USA) was polished with wet Alumina slurry (0.05 μm; Buehler, Lake Bluff, Il, USA). The polished electrode was dipped in an ethanolic solution of 5 mM thioctic acid overnight, and then washed with ethanol and subsequently with ultra-pure water prior to use. Electrochemical measurements were performed in a three-electrode setup containing an Ag/AgCl (3 M KCl) reference electrode and a Pt counter electrode with a CH Instrument 720C electrochemical analyzer. CVs on gold microdisk electrodes before and after TA modification were measured in 3.0 mM $K_3Fe(CN)_6$ solutions containing 0.1 M KCl and 10 mM phosphate (pH 2.5, 3.5, 4.5, 5.5, 6.5 and 7.5) at room temperature (*ca.* 25 °C). The relative standard deviation of the reduction current of $Fe(CN)_6^{3-}$ obtained at 3–6 separate TA-modified electrodes was ca. 20%, probably due to the variation of the molecular packing of the TA monolayers. The reproducibility of CV data was not improved by increasing TA modification time or by electrochemically cleaning a microdisk gold electrode in an aqueous KOH or H_2SO_4 solution prior to TA modification. Theoretical voltammograms for the reduction of $Fe(CN)_6^{3-}$ on microelectrodes under the influence of the Frumkin effect were obtained using MS-Excel.

3.3. Results and Discussion

3.3.1. Stability of the TA Monolayer on a Microdisk Gold Electrode.

First, the stability of a TA-modified microdisk gold electrode during multiple CV measurements in 3.0 mM $Fe(CN)_6^{3-}$ solutions was examined. Figure 3.1 shows the voltammetric response of a TA-modified microelectrode for $Fe(CN)_6^{3-}$ as a function of pH. The CV measurements were performed in seven separate solutions of different pH, from acidic (2.5) to neutral pH (7.5) and then pH 2.5. The reduction current of $Fe(CN)_6^{3-}$ was smaller at higher pH, reflecting the deprotonation of the terminal -COOH groups of the TA monolayer.[26] However, the second measurement at pH 2.5 exhibited a larger reduction current as compared with the first measurement at pH 2.5, suggesting the desorption of TA from the gold surface during the CV

measurements probably due to the etching of gold by $Fe(CN)_6^{3-}$.[27] The etching may have occurred at defects in the loosely-packed TA monolayer: Its surface coverage (3.1×10^{-10} mol/cm^2)[28] is much lower than that of densely-packed alkanethiol monolayers (2.5×10^{-9} mol/cm^2).[18] Because of the relatively low stability of the TA monolayer in $Fe(CN)_6^{3-}$ solutions, each freshly-prepared TA-modified microelectrode was used to measure one CV data at a certain pH condition.

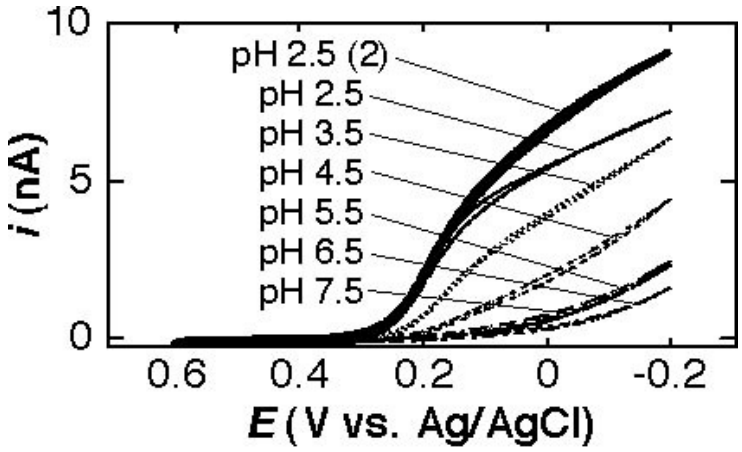

Figure 3.1 Typical voltammetric response (scan rate: 10 mV/s) of a TA-modified microdisk gold electrode (25 µm in diameter) for $Fe(CN)_6^{3-}$ as a function of pH. CV measurements were performed from pH 2.5 to 7.5, and then at pH 2.5 (pH 2.5 (2)). Measured in 3.0 mM $Fe(CN)_6^{3-}$ solutions containing 0.1 M KCl and 10 mM phosphate at room temperature (ca. 25°C)

3.3.2. pH Dependence of the CVs of $Fe(CN)_6^{3-}$ at Freshly-Prepared TA-Modified Microdisk Gold Electrodes.

Figure 3.2 shows typical CVs of $Fe(CN)_6^{3-}$ at microdisk gold electrodes before and after TA modification at different pH. Bare microdisk gold electrodes exhibited very similar sigmoidal CVs at all the pH conditions examined. The similarity in limiting currents (i_{lim}) and CV shapes indicate that solution pH did not affect the diffusion coefficient (D) and electron-transfer rate constant (k^0) of $Fe(CN)_6^{3-}$ at the bare gold electrode. These parameters were calculated from the CV data using the following equations: [18, 19]

$$i_{\lim} = 4nFDCr \qquad (1)$$

$$\frac{i}{i_{\lim}} = \frac{1}{\frac{D}{rk}\exp\left[\frac{\alpha F}{RT}(E - E^{0\prime})\right] + 1 + \exp\left[\frac{F}{RT}(E - E^{0\prime})\right]} \qquad (2)$$

where n is the number of electrons (n = 1 for $Fe(CN)_6^{3-}$), F is Faraday's constant (= 96485 C/mol), C is the concentration of $Fe(CN)_6^{3-}$ (= 3.0 mM), r is the radius of the disk electrode (= 12.5 μm), R is the gas constant (= 8.31 J/K•mol), T is temperature (= 298 K for 25 °C), k is the electron-transfer rate constant (= k^0 at an unmodified gold electrode), α is the transfer coefficient (≈ 0.5), E is the applied potential, and $E^{0\prime}$ is the formal potential of $Fe(CN)_6^{3-/4-}$. Regardless of solution pH, the D and k^0 of $Fe(CN)_6^{3-}$ were similar (Figure 3.3), ca. 7.7 x 10^{-6} cm^2/s and 2.5 x 10^{-2} cm/s, respectively, which were very close to literature values.[18, 29]

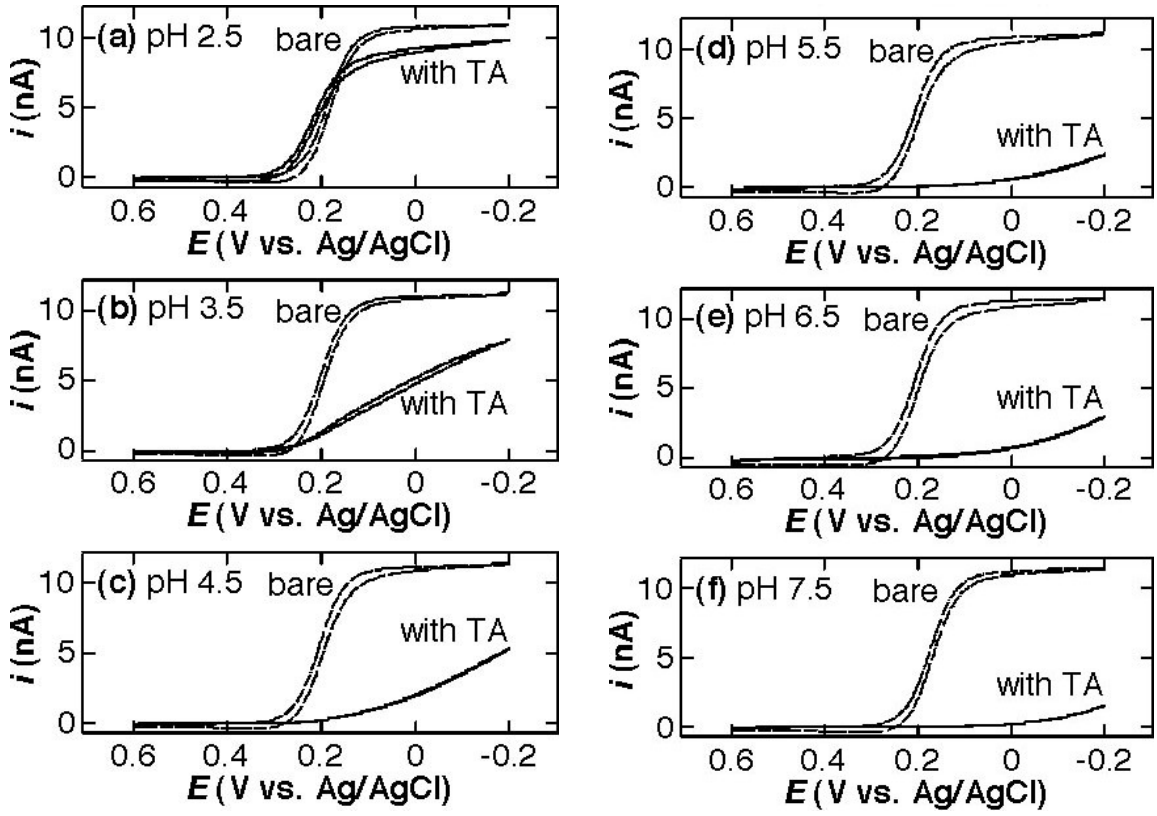

Figure 3.2 CVs (scan rate: 10 mV/s) of $Fe(CN)_6^{3-}$ at microdisk gold electrodes (25 μm in diameter) before (dashed lines) and after (solid lines) TA modification in solutions of different pH. Each CV was measured at a freshly-prepared electrode. Measured in 3.0 mM $Fe(CN)_6^{3-}$ solutions containing 0.1 M KCl and 10 mM phosphate at room temperature (ca. 25°C). Data taken by Ms. Shinobu Nagasaka.

In contrast, the reduction current of $Fe(CN)_6^{3-}$ at TA-modified microelectrodes gradually decreased from pH 2.5 to 5.5, and then was similar at higher pH. At pH 2.5, a quasi-reversible CV was observed, although the limiting current was slightly smaller than that at the microelectrode prior to TA modification. At the higher pH, CVs were less reversible, suggesting a decrease in the rate constant of the electrode reaction. These observations could be related to the deprotonation of the -COOH groups of the TA monolayer covalently immobilized onto the electrode surface, as described in the previous section.[26] In contrast, electrodes coated with insulator-based nanopores having ionizable surface functional groups exhibited pH-dependent CV changes with similar reversibility, which were explained by changes in effective pore size due to the electrical double layer extending from the pore surface.[30-34] The CV data at TA-modified micro-disk electrodes were compared to the theoretical voltammograms in the next section.

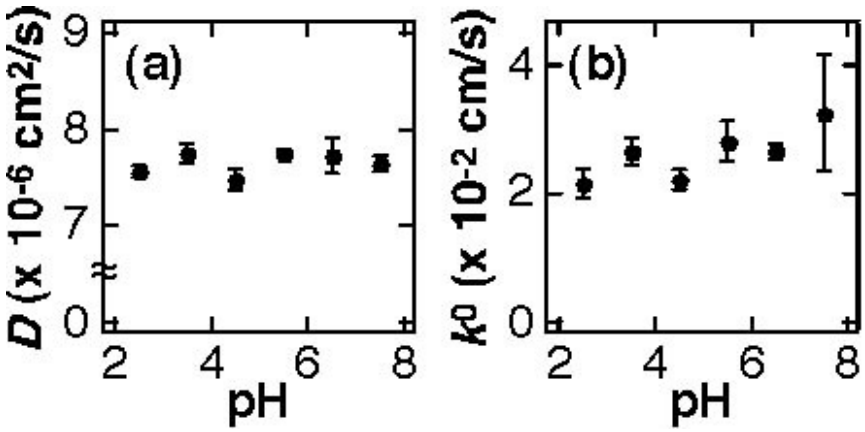

Figure 3.3 (a) *D* and (b) k^0 values of $Fe(CN)_6^{3-}$ measured at bare microdisk gold electrodes (25 µm in diameter) in 3.0 mM $Fe(CN)_6^{3-}$ solutions containing 0.1 M KCl and 10 mM phosphate at room temperature (ca. 25°C). The plots and error bars indicate the averages and standard deviations obtained from three separate electrodes.

3.3.4. Theoretical Voltammetric Responses of TA-Modified Micro disk Electrodes.

As discussed above, the pH-dependent changes in voltammetric reversibility at TA-modified electrodes could reflect electrode reaction kinetics on charged electrodes that can be interpreted based on the Frumkin effect.[18] In the Frumkin effect, electrode reaction kinetics is

affected by changes in (i) the distribution of ionic electroactive species at charged electrode surface due to electrostatic interactions and (ii) the effective potential driving the redox reaction at charged electrode. The rate constant at a charged electrode (k^0_{eff}) can be related to the rate constant at a bare electrode (k^0) using the following equation:[18, 20, 35]

$$k^0_{eff} = k^0 \exp\left[\frac{(\alpha - z_{red})F\phi_2}{RT}\right] \quad (3)$$

where z_{red} is the charge of the electroactive species (z_{red} = -3 for $Fe(CN)_6^{3-}$) and ϕ_2 (V) is the potential at the outer Helmholtz plane. In a 1:1 electrolyte, ϕ_2 is described using the electrode surface charge density, σ (C/cm^2), according to the Gouy-Chapman theory:[18]

$$\sigma = \left(8RT\varepsilon\varepsilon_0 C_{elec}\right)^{1/2} \sinh\left(\frac{zF\phi_2}{2RT}\right) \quad (4)$$

where z is the charge of the supporting electrolyte ions (here, z = 1), ε is the dielectric constant of the solution (~ 78.35), ε_0 the permittivity of free space (= 8.85 x 10^{-12} F/m), and C_{elec} is the supporting electrolyte concentration (~ 0.1 M). Assuming that the electrode surface density is determined by the charge of a TA monolayer, σ can be described using the following equation regarding the protonation/deprotonation of the surface -COOH groups:[36]

$$\sigma = -\frac{FK_a\Gamma_{COOH,total}}{[H^+] + K_a} \quad (5)$$

where K_a is the apparent acid dissociation constant of the surface -COOH groups, $\Gamma_{COOH,\ total}$ is the TA density on the electrode surface (= 3.1 x 10^{-10} mol/cm^2),[28] and [H$^+$] is the proton concentration in the solution. A solid-form equation describing the relationship between i/i_{lim} and $E - E^0$ could be obtained from Eqs (2)–(5) ($k = k^0_{eff}$ in Eq (2)), and was used to simulate the pH dependence of voltammetric response of a TA-modified micro-disk electrode.

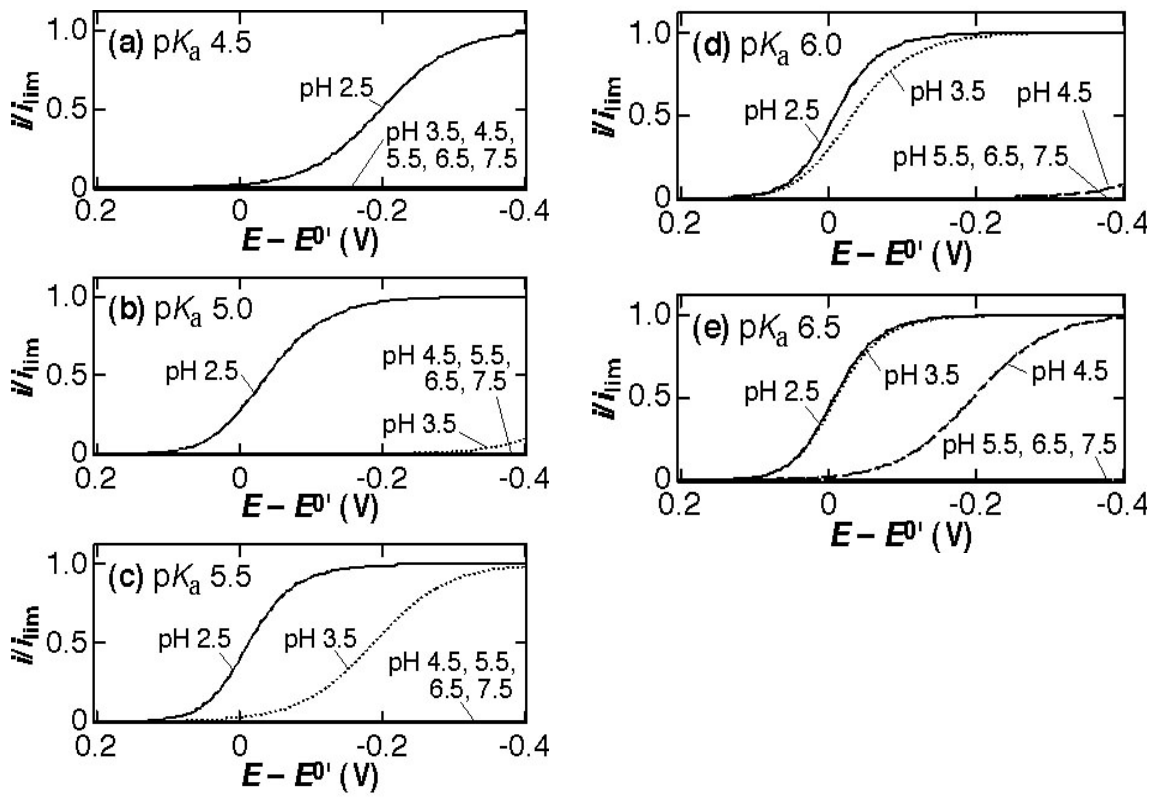

Figure 3.4 Theoretical voltammetric pH responses for the reduction of a redox-active trivalent anion at microdisk electrodes coated with acidic functional groups having different apparent surface pK_a values: (a) pK_a 4.5, (b) pK_a 5.0, (c) pK_a 5.5, (d) pK_a 6.0, (e) pK_a 6.5. The k^0 and D values employed for the simulation were obtained from Figure 3. The currents were normalized by the transport-limited current value (i_{lim})

Figure 3.4 shows the theoretical voltammetric pH responses for the reduction of a trivalent redox-active anion at micro-disk electrodes coated with monolayers having acidic functional groups. The pH dependences were simulated by varying the apparent surface pK_a of the acidic groups. In all cases, more reversible voltammograms could be obtained at the lower pH, reflecting the larger k^0_{eff} due to the smaller negative surface charge, as suggested by Eq (3). In addition, the trivalent redox-active anion could be reduced at higher pH for surface acidic groups having higher apparent surface pK_a, i.e., higher affinity to H^+. Importantly, the pH

dependence measured experimentally (Figure 3.2) was close to the one theoretically obtained with the apparent surface pK_a of 5.5 (Figure 3.4c), which was consistent with that of surface -COOH groups in loosely-packed monolayers.[37] Indeed, the apparent surface pK_a estimated using the least squares fitting of theoretical curves to the CV data was 5.42. Using the pK_a value, k^0_{eff} values (cm/s) for the trivalent redox-active anion could be calculated to be 1.1 x 10^{-2} (pH 2.5), 5.5 x 10^{-5} (pH 3.5), 3.5 x 10^{-11} (pH 4.5), 5.9 x 10^{-16} (pH 5.5), 1.6 x 10^{-17} (pH 6.5) and 1.2 x 10^{-17} (pH 7.5). The decrease in k^0_{eff} from pH 2.5 to 5.5 originates from an increase in the surface negative charge due to the deprotonation of the surface acidic groups, leading to the voltammetric response. The similarity of the experimental and theoretical data suggests that the voltammetric response of a TA-modified electrode to pH can be primarily explained on the basis of the variation of the electrode reaction kinetics of $Fe(CN)_6^{3-}$ due to the charge of the COOH-terminated surface. On the other hand, experimental reduction currents at pH higher than 4.5 were larger than the theoretical currents (Figure 3.2c-f vs. Figure 3.4c), probably reflecting the presence of defects in the TA monolayers. It should be noted that the theoretical equations can be used for predicting the effects of different parameters, including the density and affinity of surface binding moieties as well as the charges of analytes and electroactive markers, on the voltammetric responses of microelectrode-based CB-ICSs.

3.4. Conclusions

This chapter discussed the experimental and theoretical investigations on the pH dependence of the CVs of $Fe(CN)_6^{3-}$ at TA-modified micro-disk electrodes. Although the defects of a monolayer significantly influenced the experimental CV data, the voltammetric pH responses measured experimentally were similar to quasi-reversible steady-state voltammograms simulated in consideration of the Frumkin effect. The similarity suggests that changes in electrode reaction kinetics reflecting the distribution of $Fe(CN)_6^{3-}$ and the effective potential at the charged electrode surface would be one of the major factors affecting the voltammetric responses of ICSs based on electrostatic repulsion.

References

(1) Umezewa, Y.; Aoki, H. *Anal. Chem.* **2004***, 76*, 320 A-326 A.

(2) Sugawara, M.; Kojima, K.; Sazawa, H.; Umezawa, Y. *Anal. Chem.* **1987***, 59*, 2842-2846.

(3) Odashima, K.; Kotato, M.; Sugawara, M.; Umezawa, Y. *Anal. Chem.* **1993***, 65*, 927-936.

(4) Nagase, S.; Kataoka, M.; Naganawa, R.; Komatsu, R.; Odashima, K.; Umezawa, Y. *Anal. Chem.* **1990***, 62*, 1252-1259.

(5) Xiao, K. P.; Buhlmann, P.; Umezawa, Y. *Anal. Chem.* **1999***, 71*, 1183-1187.

(6) Katayama, Y.; Ohuchi, Y.; Higashi, H.; Kudo, Y.; Maeda, M. *Anal. Chem.* **2000***, 72*, 4671-4674.

(7) Ito, T. *J Electroanal Chem* **2001***, 495*, 87-97.

(8) Murata, M.; Nakayama, M.; Irie, H.; Yakabe, K.; Fukuma, K.; Katayama, Y.; Maeda, M. *Analytical Sciences* **2001***, 17*, 387-390.

(9) Aoki, H.; Hasegawa, K.; Tohda, K.; Umezawa, Y. *Biosensors and Bioelectronics* **2003***, 18*, 261-267.

(10) Kurzatkowska, K.; Dolusic, E.; Dehaen, W.; Siero-Stoltny, K.; Sieron, A.; Radecka, H. *Anal. Chem.* **2009***, 81*, 7397-7405.

(11) Gadzekpo, V. P. Y.; Xiao, K. P.; Aoki, H.; Buhlmann, P.; Umezawa, Y. *Anal. Chem.* **1999***, 71*, 5109-5115.

(12) Gadzekpo, V. P. Y.; Bühlmann, P.; Xiao, K. P.; Aoki, H.; Umezawa, Y. *Anal. Chim. Acta* **2000***, 411*, 163-173.

(13) Aoki, H.; Umezawa, Y. *Analyst* **2003***, 128*, 681-685.

(14) Hou, Y.; Gochin, M. *Anal. Chem.* **2008***, 80*, 5924-5929.

(15) Wightman, R. M. *Science* **2006***, 311*, 1570-1574.

(16) Fritsch, I.; Aguilar, Z. P. *Anal. Bioanal. Chem.* **2007***, 387*, 159-163.

(17) Vandaveer, I., W.R.; Pasas-Farmer, S. A.; Fischer, D. J.; Frankenfeld, C. N.; Lunte, S. M. *Electrophoresis* **2004***, 25*, 3528-3549.

(18) Bard, A. J.; Faulkner, L. R., Eds.; In *Electrochemical Methods, Fundamentals and Applications;* Bard, A. J., Faulkner, L. R., Eds.; Wiley: New York, 2001; Vol. 2nd.

(19) Oldham, K. B.; Zoski, C. G. *J Electroanal Chem* **1988***, 256*, 11-19.

(20) Watkins, J. J.; White, H. S. *Langmuir* **2004***, 20*, 5474-5483.

(21) Degefa, T. H.; Schön, P.; Bongard, D.; Walder, L. *J Electroanal Chem* **2004***, 574*, 49-62.

(22) Schön, P.; Degefa, T. H.; Asaftei, S.; Meyer, W.; Walder, L. *J. Am. Chem. Soc.* **2005***, 127*, 11486-11496.

(23) Takehara, K.; Takemura, H.; Ide, Y. *Electrochim. Acta* **1994***, 39*, 817-822.

(24) Cheng, Q.; Brajter-Toth, A. *Anal. Chem.* **1995***, 67*, 2767-2775.

(25) Cheng, Q.; Brajter-Toth, A. *Anal. Chem.* **1992***, 64*, 1998-2000.

(26) Cheng, Q.; Brajter-Toth, A. *Anal. Chem.* **1996***, 68*, 4180-4185.

(27) Dijksma, M.; Boukamp, B. A.; Kamp, B.; van Bennekom, W. P. *Langmuir* **2002***, 18*, 3105-3112.

(28) Wang, Y.; Kaifer, A. E. *The Journal of Physical Chemistry B* **1998***, 102*, 9922-9927.

(29) Sabatani, E.; Rubinstein, I.; Maoz, R.; Sagiv, J. *J Electroanal Chem* **1987***, 219*, 365-371.

(30) Newton, M. R.; Bohaty, A. K.; White, H. S.; Zharov, I. *J. Am. Chem. Soc.* **2005***, 127*, 7268-7269.

(31) Wang, G.; Zhang, B.; Wayment, J. R.; Harris, J. M.; White, H. S. *J. Am. Chem. Soc.* **2006***, 128*, 7679-7686.

(32) Li, Y.; Maire, H. C.; Ito, T. *Langmuir* **2007***, 23*, 12771-12776.

(33) Li, Y.; Ito, T. *Langmuir* **2008***, 24*, 8959-8963.

(34) Perera, D. M. N.; Ito, T. *Analyst* **2010***, 135*, 172-176.

(35) Burshtain, D.; Mandler, D. *J Electroanal Chem* **2005***, 581*, 310-319.

(36) Smith, C. P.; White, H. S. *Langmuir* **1993***, 9*, 1-3.

(37) Dai, Z.; Ju, H. *Phys. Chem. Chem. Phys.* **2001***, 3*, 3769-3773.

Chapter 4 - Cyclic Voltammetry on Recessed Nanodisk-Array Electrodes Prepared from Track-Etched Polycarbonate Membranes with 10-nm Diameter Pores

Reproduced by permission of The Royal Society of Chemistry
Published as: Perera, D.M.N.T. and Ito, T. *Analyst*, **2010**, *135*, 172-176.

4.1 Introduction

Track etched polycarbonate membranes have nearly cylindrical pore shapes and narrow pore size distribution. Thus they have been employed as filtration membranes,[1] as model systems for studying hindered mass transport[2] and as templates for synthesis of nanowires and nano electrode ensembles.[3, 4] TEPCMs incorporated into microfluidic devices have been used as diffusion controlled separators between two channels,[5] as potential controlled gates,[6-10] and for the electrokinetic preconcentration of molecules.[6, 11, 12] Nano-porous TEPCM can be used in separation and detection of analytes based on size exclusion and chemical interaction. Such devises are fabricated by electroless deposition of gold on TEPCM nano-pores and their subsequent chemical functionalization with thiolate self assembled monolayers.[13, 14] All these applications involves mass transport of solvated molecules that reflects the surface properties such as charge and hydrophobicity of TEPCM nano-pores.

Previously the surface charge of unmodified TEPCM nano-pores was assessed by streaming potential,[15-17] electro-viscous effects[17] and flux of florescent molecules.[18, 19] These studies have suggested the presence of surface charge on solution filled TEPCM nano-pores that possibly originates from functional groups developed during membrane processing or adsorption of ions from the aqueous solution.[16, 18, 19] Although these methods have provided information reflecting the net properties of nano-pores, they have not been employed to discuss the heterogeneous nature of the nano-pores (e.g. surface vs. cavity). The surface of TEPCM nano-pores is often coated with a thin polyvinylpyrrolidone (PVP) layer to increase the hydrophilicity, that may play an essential role in the molecular mass transport behavior.[18, 19]

In contrast to the above methods, electrochemical methods have been used to discuss the heterogeneous natures of nanoporous media deposited on electrode surfaces.[20] A faradic current

reflects the diffusion coefficients and concentrations of redox species in the media, the kinetics of the electrode reaction, the time-scale of measurements (e.g., scan rate in voltammetry), solution convection and electrode geometry.[21] Thus, detailed analysis of faradic currents measured under controlled conditions made it possible to discuss the distinct electron/mass transport modes within nanoporous media. For example, the properties of two bicontinuous phases within anodic aluminum oxide (AAO) nanopores modified with an organic polymer or bilayer assemblies were investigated using voltammetry and chronocoulometry on AAO-based recessed nanodisk-array electrodes (RNEs).[22-25] The mass/electron transport properties and concentration of redox species within a thin organic layer on the nanopore were different from those within the nanopore cavity, resulting in observations of enhanced redox reaction.[23-25]

In this chapter, study of the surface properties of 10-nm diameter TEPCM nano-pores coated with PVP using cyclic voltammetry on TEPCM based RNEs is discussed. Due to their higher surface-to-volume ratio, TEPCMs with 10-nm diameter pores were expected to offer a faradic current more significantly reflecting the nanopore surface properties as compared to those containing 50-nm diameter pores.[26] TEPCM-based RNEs were characterized using several different approaches, including measurements of charging and faradic currents, profilometry to measure the membrane thickness, and scanning electron microscopy (SEM) to determine the pore density and diameter. As compared to AAO membranes[3, 14, 22-25, 27] and nanoporous membranes derived from block copolymers[28-34] that contain an array of densely-packed cylindrical nanopores, the pore density in the TEPCM was much lower. The low pore density provided a means for characterizing the RNEs from the transition of cyclic voltammogram (CV) shapes measured at different scan rates.[26, 35-39] At slower scan rates, sigmoidal CVs reflecting the steady-state, radial diffusion of redox molecules from a solution into the nanopores were observed on these RNEs, which facilitated our discussion on the electrochemical data. The charge within the TEPCM nanopores was assessed from the limiting currents in sigmoidal CVs of charged and uncharged redox species measured at different pH and supporting electrolyte concentrations.

4.2 Experimental Section

4.2.1 Chemicals and Materials

All solutions were prepared with water having a resistivity of 18 MΩcm or higher (Barnstead Nanopore Systems). Potassium nitrate (Fisher Chemical), potassium dihydrogen phosphate (Fisher Chemical), potassium hydrogen phosphate (Fisher Chemical), potassium hydroxide (Fisher Chemical), potassium ferricyanide ($K_3Fe(CN)_6$; Arcos Organics), ferrocenylmethyltrimethylammonium iodide ($TMAFc^+I^-$; Strem Chemicals), and 1,1'-ferrocenedimethanol (FcDM; Aldich) were of reagent grade quality and used without further purification. Ferrocenylmethyltrimethylammonium nitrate ($TMAFc^+NO_3^-$) was prepared by passing a $TMAFc^+I^-$ solution through NO_3^--form anion exchange resin (Amberlite IRA-900, Aldrich), and characterized using ion chromatography (column: Hamilton PRP-X100). TEPCMs with pore diameters of 10 nm (25 mm membrane diameter) were obtained from Osmonics. The thickness of a TEPCM was measured using a profilometer (Ambios Technology XP-2 Stylus Profiler). SEM images of a TEPCM were measured using a Zeiss Leo 32 SEM at the Microscopy & Analytical Imaging Laboratory, the University of Kansas, upon deposition of a 5-nm thick Pd/Au alloy film on the sample.

4.2.2 Fabrication of TEPCM-Based RNEs

TEPCM-based RNEs were prepared according to the procedures described previously.[26] In short, the rougher face of a TEPCM was coated with a gold layer (≥ 200nm thick) via sputtering (EFFA Coater, Ernest F. Fullam), and then the gold side was mounted on a glass slide (ca. 1 x 1 cm^2) coated with a thin film of PDMS (Sylgard 184, Dow Corning). Electrical contact to the Au surface was made using conducting copper tape (Electron Microscopy Sciences) to use the RNE as a working electrode (Figure 4.1).

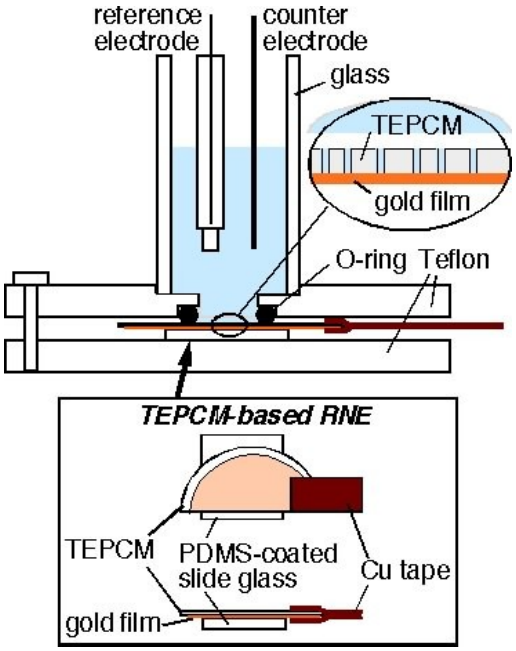

Figure 4.1 Schematic illustration of the experimental setup used for measuring CVs on a TEPCM based RNE.

4.2.3 Electrochemical Measurements

Electrochemical data were obtained using a CH Instruments Model 618B electrochemical analyzer. Electrochemical experiments were carried out in a three-electrode cell containing a Ag/AgCl (3 M KCl) reference electrode and a Pt counter electrode (**Figure 1**).[26] The area of the RNE in contact with solution was 0.34 cm^2. In addition, a 25-µm diameter gold microelectrode was used to measure the diffusion coefficients of $Fe(CN)_6^{3-}$, $TMAFc^+$ and FcDM in 0.1 M KNO_3. CV measurements were taken at scan rates ranging from 5 mV/s to 1000 mV/s at room temperature.

4.3 Results and Discussion

4.3.1 Electrochemical Characterization of TEPCM-Based RNEs with 10-nm Diameter Pores.

First, TEPCM-based RNEs were characterized by measuring (a) capacitive currents and (b) CVs of uncharged FcDM at different scan rates. The former provides a means for determining the total active area of a RNE that makes it possible to directly assess the seal

between the gold layer and TEPCM.[40] The latter offers the scan rate that gives the transition between sigmoidal and peak-shaped CVs, permitting us to discuss the diffusion behavior of FcDM within the TEPCM nanopores.[26, 35, 41]

(a) Capacitive Current Measurements

Capacitive current on a TEPCM-based RNE was obtained by measuring CVs in 0.1 M KNO_3 (Figure 4.2) and was used in determining the effective surface area of the recessed nanodisk electrode array. In a RNE, each nanodisk behaves as an individual nano electrode having an area of πa^2. The effective surface area of the nanodisk array is the sum of surface areas from each individual nanodisk (equation 4.1)

$$A_{eff} = (\pi a^2) N \qquad (4.1)$$

Where $N = \pi r^2 d$, N is the number of open pores, d is the pore density (pores/cm^2), r is the "O" ring radius (cm), and a is the radius of nano pore (cm). The cathodic and anodic current at 0.1 V vs. Ag/AgCl was used to calculate the active electrode area of a RNE using the double layer capacitance of gold surface that was measured on a gold disk electrode (5.7×10^{-5} F/cm^2). The slope of the plot of capacitive current and scan rate is used to calculate the effective surface area, according to equation 4.2. (See figure 4.3)

$$I_{chg} = \nu A C_d \qquad (4.2)$$

Where I_{chg} is the capacitive current (A), ν is the scan rate (V/s), C_d is the double layer capacitance (F/cm^2). If the seal between the TEPCM and gold film was perfect, the active electrode area of a RNE would be close to the total cross-sectional area of the open pores (5.1×10^{-4} cm^2), which was calculated from the pore radius (7.1 nm) and pore density (9.5 pores/μm^2) determined from SEM images (Figure 4.4). If the gold film is completely detached from the TEPCM, the active area would be close to the RNE area in contact to the solution (0.34 cm^2). The experimental active area was $(1.1 \pm 0.7) \times 10^{-2}$ cm^2 (average ± standard deviation from 4 separate RNEs), suggesting that the solution crept into gaps between the TEPCM and the gold film formed due to their imperfect seal. The charging current of a RNE was unchanged for 5-7 days, indicating the strong adhesion of the sputter-coated gold film onto the TEPCM in contrast to a vapor-deposited gold film.[26]

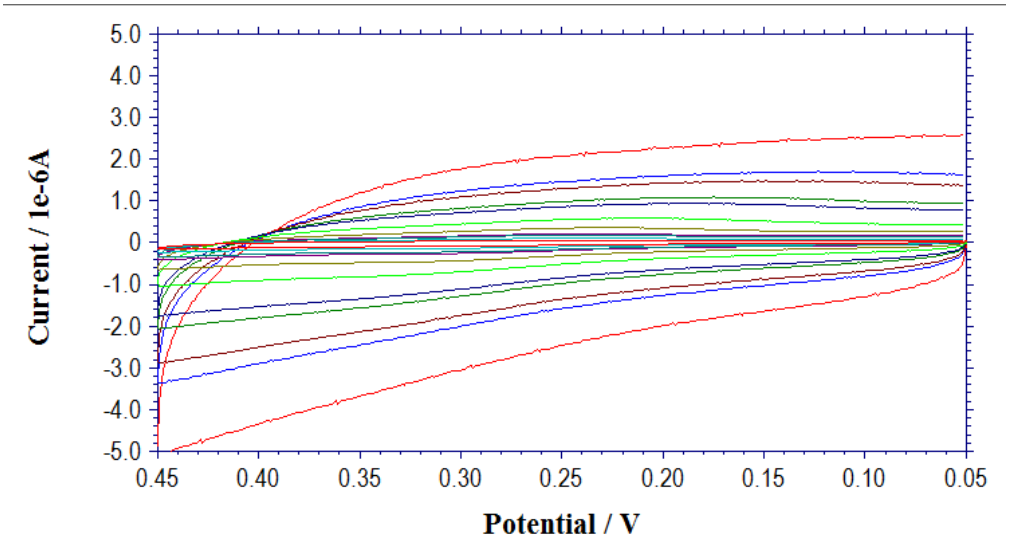

Figure 4.2 Overlaid Cyclic Voltammogram for a TEPCM based RNE (pore diameter 10nm) in 0.1M KNO_3 for scan rates 2000mV/s – 10mV/s. Capacitive current measured at 0.1V.

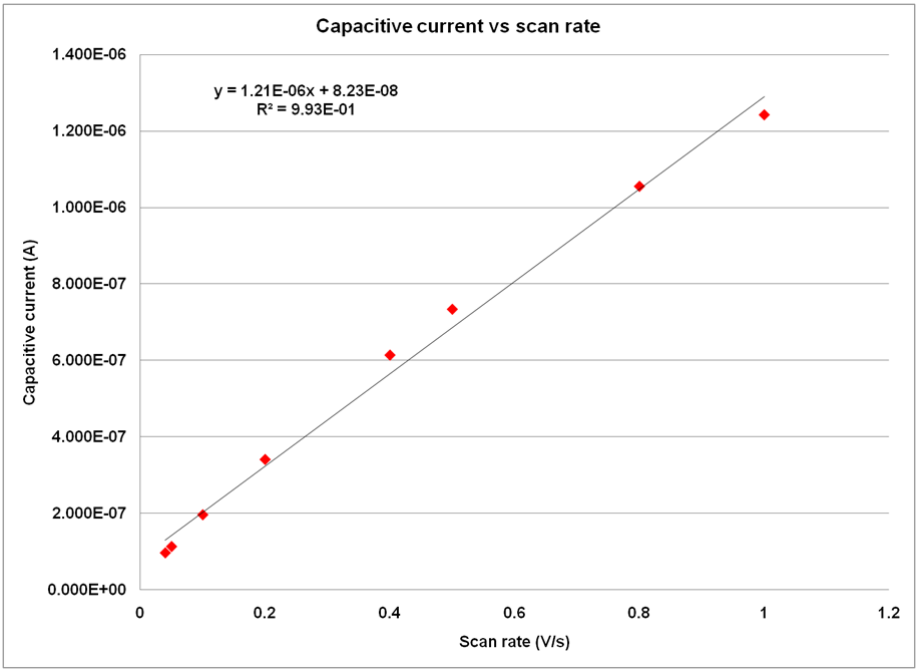

Figure 4.3 Plot of Capacitive current vs. scan rate for a TEPCM based RNE (pore diameter 10nm) in 0.1M KNO_3, for scan rates 1000 mV/s – 40 mV/s. capacitive current measured at 0.1 V.

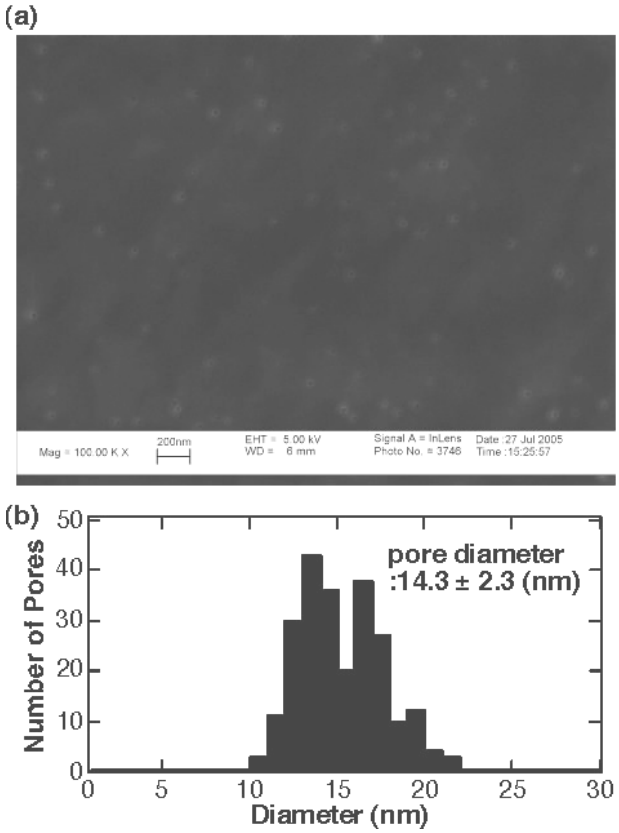

Figure 4.4 (a) SEM image of TEPCM showing pore distribution. (b) Histogram for pore size distribution of TEPCM.

(b) CV Measurements at Different Scan Rates

Subsequently, CVs of 3.0 mM FcDM on TEPCM-based RNEs with 10-nm diameter pores were measured at different scan rates (v). As shown in Figure 4.5a, the transition from sigmoidal to peak-shaped CVs was observed with increasing scan rate. The sigmoidal CVs reflected the radial diffusion of redox molecules from the outside of the pores, whereas the peak-shaped CV originated from their linear diffusion within the nanopores.[26, 35, 36] The observation of sigmoidal CVs at slower scan rates suggested that the spacing between pores was so large that the diffusion layers from individual pores did not overlap.[42]

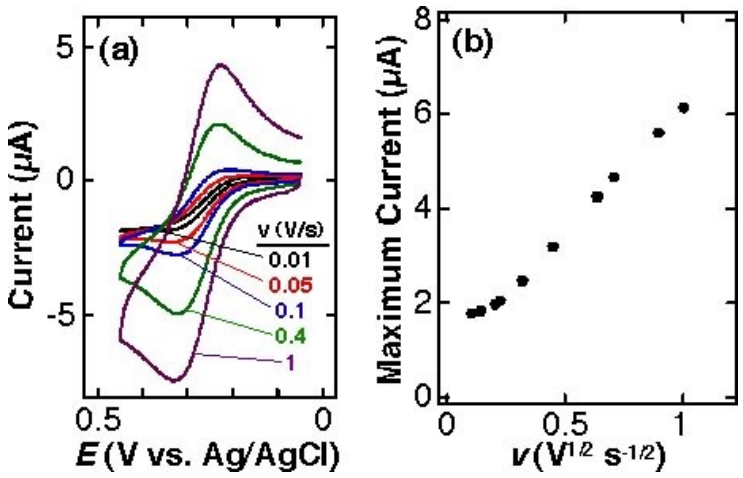

Figure 4.5(a) Cyclic voltammograms for a TEPCM-based RNE (10 nm in pore diameter) in a solution of 3.0 mM FcDM containing 0.01 M KNO_3 and 0.01 M KH_2PO_4-K_2HPO_4 buffer (pH 6.3) at five different scan rates (0.01, 0.05, 0.1, 0.4 and 1 V/s). (b) Relationship between the maximum oxidation current of 3.0 mM FcDM and the square root of scan rate. Measured in 0.01 M KNO_3 and 0.01 M KH_2PO_4-K_2HPO_4 buffer (pH 6.3) on the TEPCM-based RNE that gave CVs shown in Figure 4.5a.

Figure 4.5b summarizes the relationship between the maximum oxidation current (i.e., a limiting current (i_{lim}) in a sigmoidal CV; a peak current (i_p) in a peak-shaped CV) and scan rate, i.e., $v^{1/2}$. The maximum current was similar at lower v, and then linearly increased for v greater than 0.05 V/s. Similar results were obtained on four separate TEPCM-based RNEs with 10-nm diameter pores. These observations are qualitatively consistent with the following theoretical equations regarding i_{lim} in a sigmoidal CV and i_p in a peak-shaped CV on a RNE[35, 43]:

$$i_{\lim} = \frac{4\pi nFC_s D_s a^2 N}{4L\left(D_s / D_p\right) + \pi a} \tag{4.3}$$

$$i_p = 0.446nF(N\pi a^2)C_p\sqrt{\frac{nFD_p v}{RT}} \tag{4.4}$$

Where n is the number of electrons (n = 1 for the redox-active molecules used in this study), F is Faraday's constant (= 96485 C/mol), a is the pore diameter, R is the gas constant (= 8.31 J/K•mol), and T is temperature (= 298 K for 25 °C). N is the total number of nanopores

participating (*vide supra*), and L is the length of the nanopore, which would be close to the thickness of the TEPCM measured using profilometry (6.4 μm). These equations were derived under the assumption that the apparent diffusion coefficients and concentrations of redox species within nanopores (D_p, C_p) are different from those in a solution (D_s, C_s). Eq (4.3) indicates i_{lim} is similar regardless of v, and Eq (4.4) indicates i_p is proportional to $v^{1/2}$, as shown in Figure 4.5b.

However, in contrast to previously reported results obtained on TEPCM-based RNEs containing 50-nm diameter pores,[26] the currents observed on the RNEs with 10-nm diameter pores were larger than those calculated using the theoretical equations. For example, the average and standard deviation of i_{lim} measured on four separate RNEs was 2.3 ± 0.7 μA, and was larger than 1.4 μA that was obtained from eq (4.3) by assuming $D_p = D_s = 6.1 \times 10^{-6}$ cm^2/s for FcDM. In addition, i_p was much larger than the theoretical one calculated using eq (2) at $C_p = C_s = 3.0$ mM and $D_p = D_s$: For example, i_p obtained at 0.4 V/s from the four RNEs was 4.5 ± 0.4 μA, whereas the theoretical value was 0.8 μA. The large currents suggest the involvement of enhanced electron/mass transport (i.e., larger apparent D_p) within the nanopores such as electron hopping through a nanopore surface layer that contains the redox species at higher concentration.[20] The surface layer may originate from a PVP layer immobilized on the nanopore surface, considering its hydrophobic nature as compared with aqueous solution within the nanopore cavity. An enhanced faradic current was previously reported on AAO-based RNEs whose pore surface was covered with such an organic polymer layer.[22-25]

On the other hand, the scan rate that gave the transition (v_t) was ca. 0.05 V/s (Figure 4.5b), which was much slower than the scan rate (0.8 V/s) estimated using eq (4.5) under the assumption of $L = 6.4$ μm and $D_p \sim D_s$.[26, 27]

$$v_t = \frac{2RTD_p}{FL^2} \qquad (4.5)$$

Smaller D_p than D_s due to strong interactions with nanopores and/or larger L due to the tilted track angle may explain the slower v_t, but are not consistent with the larger i_{lim} and i_p (*vide supra*). Currently, we do not have a comprehensive model that can explain both the larger faradic current and smaller v_t.

4.3.2 CV Measurements of Uncharged and Charged Redox Species on TEPCM-Based RNEs at Different pH and Supporting Electrolyte Concentrations.

Subsequently, CVs of three different redox species were measured at different pH (pH 4 – 9) and supporting electrolyte concentrations ([KNO_3] = 0.1 and 0.01 M in addition to 0.01 M KH_2PO_4–K_2HPO_4). A series of sigmoidal CVs measured at 0.01 V/s on an identical TEPCM-based RNE is discussed. Limiting currents in such CVs may be affected by the gaps suggested by the capacitive current measurements (*vide supra*) less significantly than peak currents in peak-shaped CVs, because they reflect the diffusion of redox species from the outside of the nanopores. Eq (4.3) suggests that difference in i_{lim} can be attributed to changes in D_p. D_p reflects the partition of the redox species into the nanopores in addition to the mass/electron transport properties of the nanopores.[20, 44] Thus, comparison of the sigmoidal CVs of charged and uncharged redox species at different pH can be employed to discuss interactions between the redox species and the 10-nm diameter nanopores.

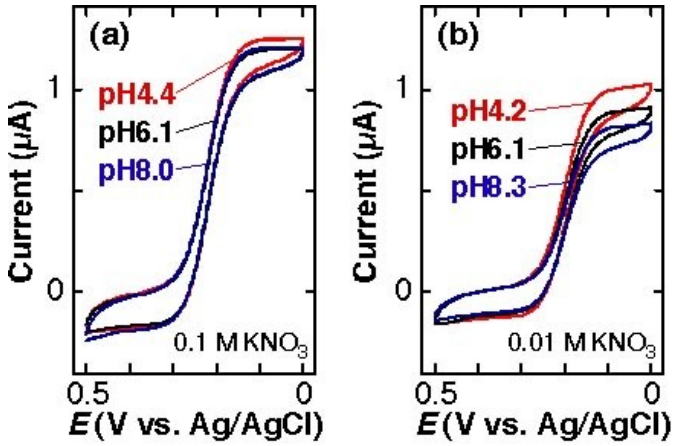

Figure 4.6 Cyclic voltammograms (scan rate: 0.01 V/s) of 1.0 mM $K_3Fe(CN)_6$ solutions containing (a) 0.1 M KNO_3 + 0.01 M KH_2PO_4-K_2HPO_4 and (b) 0.01 M KNO_3 + 0.01 M KH_2PO_4-K_2HPO_4 at three different pH on a TEPCM-based RNE (10 nm in pore diameter). These data were obtained using a RNE different from that gave the data shown in Figure 4.5

Figure 4.6 shows CVs of 1.0 mM $Fe(CN)_6^{3-}$ measured on a RNE at 0.01 V/s in solutions of three different pH conditions containing (a) 0.1 M and (b) 0.01 M KNO_3. In 0.1 M KNO_3, i_{lim} at pH 4.4 was slightly larger than those at pH 6.1 and 8.0 (Figure 4.6a). In 0.01 M KNO_3, the decrease in i_{lim} at higher pH was larger (Figure 4.6b) as compared with that in 0.1 M KNO_3. The shapes of the CVs were very similar, suggesting that the decrease in i_{lim} originated from changes in nanopore properties rather than changes in electrode surface properties. These observations suggest that electrostatic interactions between $Fe(CN)_6^{3-}$ and the nanopores play an essential role in the changes of i_{lim}.[31, 32, 45]

In contrast to the decrease in i_{lim} of $Fe(CN)_6^{3-}$, $TMAFc^+$ exhibited an increase in i_{lim} with increasing pH, as shown in Figure 4.7. The change in i_{lim} in 0.01 M KNO_3 (Figure 4.7b) was larger than that in 0.1 M KNO_3 (Figure 4.7a). The reversibility of the CVs was very similar regardless of the pH and supporting electrolyte concentrations. These results support the involvement of electrostatic interactions in the pH dependence of i_{lim} of the cationic $TMAFc^+$.

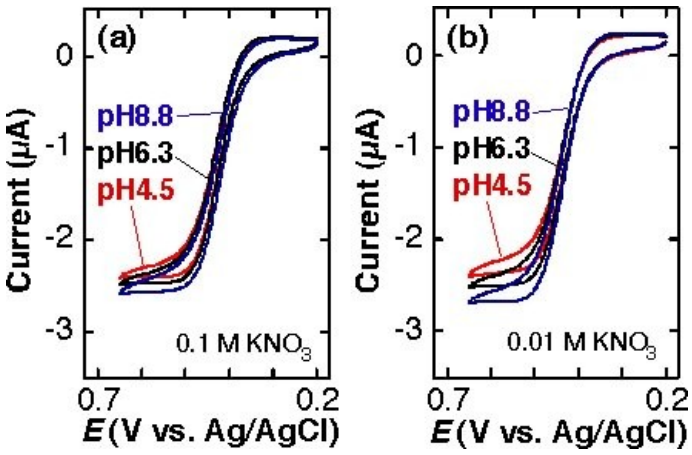

Figure 4.7 Cyclic voltammograms (scan rate: 0.01 V/s) of 3.0 mM $TMAFc^+$ solutions containing (a) 0.1 M KNO_3 + 0.01 M KH_2PO_4-K_2HPO_4 and (b) 0.01 M KNO_3 + 0.01 M KH_2PO_4-K_2HPO_4 at three different pH on a TEPCM-based RNE (10 nm in pore diameter). The data shown in Figure 4 were obtained using a RNE that gave the data shown in Figure 4.5.

CVs of uncharged FcDM were similar regardless of pH and supporting electrolyte concentrations examined (Figure 4.8). These observations indicated that the diffusion of

uncharged FcDM was not affected by electrostatic interactions in contrast to that of charged $Fe(CN)_6^{3-}$ and $TMAFc^+$ (Figures 4.6 and 4.7).

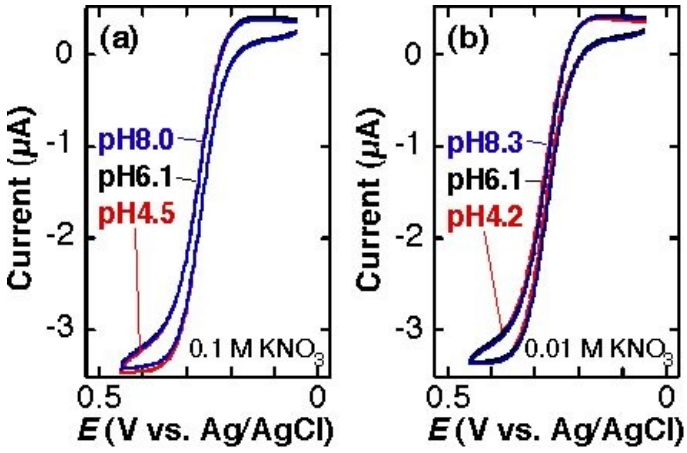

Figure 4.8 Cyclic voltammograms (scan rate: 0.01 V/s) of 3.0 mM FcDM solutions containing (a) 0.1 M KNO_3 + 0.01 M KH_2PO_4-K_2HPO_4 and (b) 0.01 M KNO_3 + 0.01 M KH_2PO_4-K_2HPO_4 at three different pH on a TEPCM-based RNE (10 nm in pore diameter). The data shown in Figure 5 were obtained using a RNE that gave the data shown in Figure 4.6.

Figure 4.9 summarizes the pH dependence of the ratio of i_{lim}/C_s between charged redox species X (where X is $Fe(CN)_6^{3-}$ or $TMAFc^+$) and FcDM measured on an identical RNE. The ratio of i_{lim}/C_s can be directly correlated to the ratio of apparent diffusion coefficients of the two species ($D_{p,X}/D_{p,FcDM}$) as shown by the following equation derived from Eq (4.3) under the assumption that a, L and N are unchanged during the measurements and $L(D_s/D_p) >> \pi a$:

$$\frac{i_{\lim,X}/C_{s,X}}{i_{\lim,FcDM}/C_{s,FcDM}} = \frac{D_{s,X}/\left[4L\left(D_{s,X}/D_{p,X}\right)+\pi a\right]}{D_{s,FcDM}/\left[4L\left(D_{s,FcDM}/D_{p,FcDM}\right)+\pi a\right]} \approx \frac{D_{p,X}}{D_{p,FcDM}} \qquad (4.6)$$

where $i_{lim,X}$ and $i_{lim,FcDM}$ are the limiting currents of charged redox species X and FcDM, and $C_{s,X}$ and $C_{s,FcDM}$ are the concentrations of X and FcDM in the sample solutions. $D_{s,X}$ and $D_{s,FcDM}$ are the diffusion coefficients of X and FcDM in solution, i.e., 6.1 x 10^{-6}, 6.7 x 10^{-6} and 7.3 x 10^{-6} cm^2/s for FcDM, $Fe(CN)_6^{3-}$ and $TMAFc^+$, respectively.

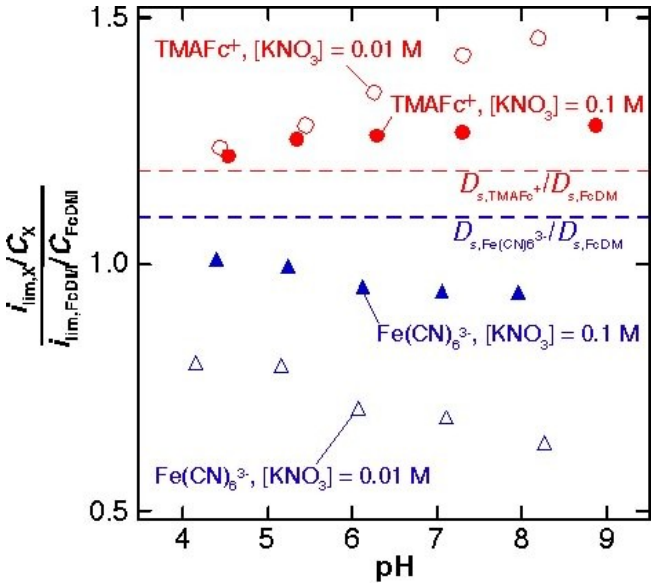

Figure 4.9 pH dependence of the ratio of i_{lim}/C between charged redox species (X = $Fe(CN)_6^{3-}$ (blue triangles) or $TMAFc^+$ (red circles)) and FcDM. The i_{lim} values were measured at 0.01 V/s on TEPCM-based RNEs (10 nm in pore diameter) in solutions containing 0.1 M (filled symbols) or 0.01 M (open symbols) KNO_3 in addition to 0.01 M KH_2PO_4-K_2HPO_4. The ratios of the diffusion coefficients in 0.1 M KNO_3 + 0.01 M KH_2PO_4-K_2HPO_4 (pH 6.3), which were measured using a gold microelectrode (25 µm in diameter), were shown in dashed lines.

Figure 4.9 clarifies the pH-dependent changes in i_{lim} of the charged redox species in addition to the influence of KNO_3 concentration on i_{lim}, as described above. In addition, for the pH range examined, the ratios for $Fe(CN)_6^{3-}$ were smaller than its $D_{s,X}/D_{s,FcDM}$, whereas those of $TMAFc^+$ were larger than its $D_{s,X}/D_{s,FcDM}$. These results suggest that the 10-nm diameter nanopores were negatively charged over the pH range examined, and the charge increased at the higher pH. The increase in the negative charge at higher pH enhanced electrostatic attraction and repulsion with $TMAFc^+$ and $Fe(CN)_6^{3-}$, resulting in the increase and decrease in the i_{lim}/C_s ratio, respectively. The larger and smaller redox currents of $Fe(CN)_6^{3-}$ and $TMAFc^+$ at the lower KNO_3 concentration can be explained by the weaker screening of the negative charge of the nanopore surface that enhanced the electrostatic interactions.[16-18] The pH range that gave the change in i_{lim}/C_s ratios was pH 4–6 for both charged redox molecules, which is similar to the pH

range that gave an increase in the negative streaming potential.[16] The pH range suggests that the negative surface charge may originate from functional groups such as –COOH groups (pK_a ~ 4.5) that were developed during membrane processing.[16] The PVP layer on the nanopore surface would not directly involve in the negative surface charge because of the high pK_a value of its amide group.[46] Importantly, the deviation of $D_{p,X}/D_{p,FcDM}$ from $D_{s,X}/D_{s,FcDM}$ for $Fe(CN)_6^{3-}$ was negligible on TEPCM-based RNEs with 50-nm diameter pores as suggested by the excellent correlation between experimental and theoretical currents.[26] probably due to the smaller contributions of the surface properties to the mass/electron transport through the 50-nm diameter nanopores.

4.4 Conclusions

This chapter discussed the CVs of uncharged and charged redox species on TEPCM-based RNEs with 10-nm diameter pores. The effects of pH and supporting electrolyte concentrations on the CVs suggested the presence of negative charge within the nanopores. The faradic currents measured in this study were larger than those estimated using theoretical equations, suggesting the enhanced mass and/or electron transport through the nanopores. These results may reflect the presence of a distinct surface layer on the 10-nm diameter nanopores to which the redox species partition preferentially. The CV data reported here offered information on the charge properties within the 10-nm diameter nanopores, which may make it possible to tune the properties of TEPCMs as templates for nanomaterials synthesis and separation membranes.

References

(1) Han, J.; Fu, J.; Schoch, R. B. *Lab Chip* **2008**, *8*, 23-33.

(2) Deen, W. M. *AIChEJ* **1987**, *33*, 1409-1425.

(3) Martin, C. R. *Science* **1994**, *266*, 1961-1966.

(4) Hulteen, J. C.; Martin, C. R. *J. Mater. Chem.* **1997**, *7*, 1075-1087.

(5) Ismagilov, R. F.; Ng, J. M. K.; Kenis, P. J. A.; Whitesides, G. M. *Anal. Chem.* **2001**, *73*, 5207-5213.

(6) Kuo, T.; Cannon, D. M.; Shannon, M. A.; Bohn, P. W.; Sweedler, J. V. *Sensors and Actuators A: Physical* **2003**, *102*, 223-233.

(7) Kuo, T.; Cannon, , Donald M.; Chen, Y.; Tulock, J. J.; Shannon, M. A.; Sweedler, J. V.; Bohn, P. W. *Anal. Chem.* **2003**, *75*, 1861-1867.

(8) Cannon, , Donald M.; Kuo, T.; Bohn, P. W.; Sweedler, J. V. *Anal. Chem.* **2003**, *75*, 2224-2230.

(9) Fa, K.; Tulock, J. J.; Sweedler, J. V.; Bohn, P. W. *J. Am. Chem. Soc.* **2005**, *127*, 13928-13933.

(10) Gatimu, E. N.; Sweedler, J. V.; Bohn, P. W. *Analyst* **2006**, *131*, 705-709.

(11) Dai, J.; Ito, T.; Sun, L.; Crooks, R. M. *J. Am. Chem. Soc.* **2003**, *125*, 13026-13027.

(12) Zhang, Y.; Timperman, A. T. *Analyst* **2003**, *128*, 537-542.

(13) Martin, C. R.; Nishizawa, M.; Jirage, K.; Kang, M.; Lee, S. B. *Adv Mater* **2001**, *13*, 1351-1362.

(14) Baker, L. A.; Jin, P.; Martin, C. R. *Crit. Rev. Solid State Mat. Sci.* **2005**, *30*, 183-205.

(15) Kim, K. J.; Fane, A. G.; Nyström, M.; Pihlajamaki, A. *J. Membr. Sci.* **1997**, *134*, 199-208.

(16) Lettmann, C.; Möckel, D.; Staude, E. *J. Membr. Sci.* **1999**, *159*, 243-251.

(17) Huisman, I. H.; Prádanos, P.; Calvo, J. I.; Hernández, A. *J. Membr. Sci.* **2000**, *178*, 79-92.

(18) Kemery, P. J.; Steehler, J. K.; Bohn, P. W. *Langmuir* **1998**, *14*, 2884-2889.

(19) Kuo, T.; Sloan, L. A.; Sweedler, J. V.; Bohn, P. W. *Langmuir* **2001**, *17*, 6298-6303.

(20) Murray, R. W., Ed.; In *Molecular Design of Electrode Surfaces;* Wiley & Sons: New York, 1992; .

(21) Bard, A. J.; Faulkner, L. R., Eds.; In *Electrochemical Methods, Fundamentals and Applications;* Bard, A. J., Faulkner, L. R., Eds.; Wiley: New York, 2001; Vol. 2nd.
(22) Miller, C. J.; Majda, M. *J. Am. Chem. Soc.* **1985***, 107*, 1419-1420.
(23) Miller, C. J.; Majda, M. *J Electroanal Chem* **1986***, 207*, 49-72.
(24) Miller, C. J.; Majda, M. *J. Am. Chem. Soc.* **1986***, 108*, 3118-3120.
(25) Miller, C. J.; Widrig, C. A.; Charych, D. H.; Majda, M. *J. Phys. Chem.* **1988***, 92*, 1928-1936.
(26) Ito, T.; Audi, A. A.; Dible, G. P. *Anal. Chem.* **2006***, 78*, 7048-7053.
(27) Brumlik, C. J.; Martin, C. R.; Tokuda, K. *Anal. Chem.* **1992***, 64*, 1201-1203.
(28) Hillmyer, M. A. *Adv. Polym Sci.* **2005***, 190*, 137-181.
(29) Olson, D. A.; Chen, L.; Hillmyer, M. A. *Chemistry of Materials* **2008***, 20*, 869-890.
(30) Jeoung, E.; Galow, T. H.; Schotter, J.; Bal, M.; Ursache, A.; Tuominen, M. T.; Stafford, C. M.; Russell, T. P.; Rotello, V. M. *Langmuir* **2001***, 17*, 6396-6398.
(31) Li, Y.; Maire, H. C.; Ito, T. *Langmuir* **2007***, 23*, 12771-12776.
(32) Li, Y.; Ito, T. *Langmuir* **2008***, 24*, 8959-8963.
(33) Li, Y.; Ito, T. *Anal. Chem.* **2009***, 81*, 851-855.
(34) Maire, H. C.; Ibrahim, S.; Li, Y.; Ito, T. *Polymer* **2009***, 50*, 2273-2280.
(35) Tokuda, K.; Morita, K.; Shimizu, Y. *Anal. Chem.* **1989***, 61*, 1763-1768.
(36) Henry, C. S.; Fritsch, I. *Anal. Chem.* **1999***, 71*, 550-556.
(37) Kralj, B.; Dryfe, R. A. W. *Phys. Chem. Chem. Phys.* **2001***, 3*, 3156-3164.
(38) Bhatt, A. I.; Dryfe, R. A. W. *J Electroanal Chem* **2005***, 584*, 131-140.
(39) Zoski, C. G.; Yang, N.; He, P.; Berdondini, L.; Koudelka-Hep, M. *Anal. Chem.* **2007***, 79*, 1474-1484.
(40) Penner, R. M.; Martin, C. R. *Anal. Chem.* **1987***, 59*, 2625-2630.
(41) Amatore, C.; Savéant, J. M.; Tessier, D. *J Electroanal Chem* **1983***, 147*, 39-51.
(42) Beriet, C.; Ferrigno, R.; Girault, H. H. *J Electroanal Chem* **2000***, 486*, 56-64.
(43) Bond, A. M.; Luscombe, D.; Oldham, K. B.; Zoski, C. G. *J Electroanal Chem* **1988***, 249*, 1-14.
(44) Savéant, J. *J Electroanal Chem* **1991***, 302*, 91-101.

(45) Wang, G.; Zhang, B.; Wayment, J. R.; Harris, J. M.; White, H. S. *J. Am. Chem. Soc.* **2006***, 128*, 7679-7686.

(46) Lessene, G.; Bordeau, M.; Biran, C.; de Montauzon, D.; Gerval, J. *J Electroanal Chem* **2000***, 490*, 79-84.

Chapter 5 - Organic solvent induced permeability changes of PS-b-PMMA derived nano-porous films studied using electrochemical impedance spectroscopy.

5.1 Introduction

This chapter describes the organic solvent induced permeability changes of nano-porous films derived from PS-b-PMMA. Electrochemical Impedance Spectroscopy was used to investigate change in permeability of Fe^{2+}/Fe^{3+} redox couple, which was represented by membrane resistance in an equivalence circuit. Solution phase Atomic Force Microscopy (AFM) imaging was done in the presence and absence of organic solvents, to assess the change in pore diameter due to swelling of the nano-porous films.

Block copolymers (BCP) have two or more chemically distinct polymers connected end-to-end. If the constituent polymers are immiscible, and the volume fraction of the minor component is ~ 30%, the minor fragment will self assemble to form cylindrical domains in a matrix of major polymer fragment.[1-3] By etching out the minor component chemically[4], thermally[5] or photochemically[6], and provided that the major component is etch resistant, nano-porous materials can be generated. Nano-porous membranes are used in a variety of applications due to their ordered nano scale structure and high surface area. They are useful in many applications such as templates for nanowires (Si and metal)[7-9] as masks in lithography,[10, 11] electrophoretic deposition of nanoparticles[12] ultralow dielectric constant materials for high density circuits[13] and in size-based separations.[14-16] The above applications depends on substrate and nano-porous surface interactions such as specific and non specific adsorptions, interfacial chemical interactions and coloumbic interactions.[17] Control of vertical orientation of domains and surface functionalization are key factors that maximizes aforementioned applications. Vertical alignment of domains can be achieved by addition of homopolymers,[18] controlling solvent evaporation conditions,[19] optimizing the film thickness,[20] and by applying an electric field during annealing.[21] Surface functionalization of nano-porous membranes is necessary to

control mass transport based on chemical interactions between nano-pore wall and analytes. Many BCPs, that offer known surface functional groups have been synthesized.[4, 17, 22, 23] In addition, surface functional groups that result in chemical etching have been functionalized.[24]

While aforementioned applications depends on the domain alignment and interactions between surface functionalities and the analytes, responsive behavior of BCP to environmental stimuli is also an important factor in BCP applications. Interactions between nanoporous polymer films and organic solvents are important in their applications as sensors. However the life time of these sensors are limited due to delamination of polymer film from the rigid support. Delamination of the film occurs when the covalent bonds between the substrate and the polymer film breaks due to shear force resulting from shrinking and swelling.[25] Sensors based on polymer films and hydro gel membranes responding to stimuli such as pH,[26, 27] chemical/ biochemical signals,[28] analytes such as salts,[29, 30] glucose,[31, 32] ionic species (calcium, copper)[33] have been developed. Most of these sensors are mechanically stabilized by cross linking. The degree of swelling due to the stimuli in these sensors is related to optical parameters such as refractive index and wave length of diffracted light or electrical parameters such as capacitance change, conductivity and resistance. Swelling of a polymer films is related to the cross linking of the polymer, solubility of polymer film on a given solvent and the chemical properties of the solvent (functional groups, hydrophobic – hydrophilic nature) and the affinity of the functional group for the polymer.[34-36]

Most of the above sensors are based on polystyrene films in different forms; in ionic form; e.g. aminated PS or non ionic form; poly(styrene-co-divinylbenzene) or amorphous PS. Therefore the swelling of PS in various organic solvents has been studied extensively. Unlike the PS polymer beads, films have limited freedom to swell in every direction (cannot swell parallel to the substrate) and undergo higher mechanical stress. Most of these studies are done for polymer – solvent systems. We investigated the solvent effect on PS-b-PMMA nanoporous film where the nanopores are surrounded by the PS matrix (after PMMA domains have been etched out). These nanoporous films have been cross linked to a greater extent, thus the behavior of these films in organic solvents should be different in terms of degree of swelling. In our study we used polymer – solvent – water system in contrast to the previous studies.[34-37] The goal of this work was to investigate the effect of organic solvents on PS-b-PMMA nano-porous films. We

measured the permeability of a redox couple, Fe^{2+}/Fe^{3+} using electrochemical impedance spectroscopy. EIS has been used to extract different parameters such polymer film resistance and capacitance for ultra-thin copolymer brushes.[38] After fitting the data to a theoretical equivalent circuit, we were able to extract different variables representing the electrochemical changes in the PS-b-PMMA nano-porous film coated electrode. In addition to electrochemical methods, we obtained AFM images to study the topography of PS-b-PMMA nano-porous films in the presence and absence of organic solvents.

5.2 Experimental Section

5.2.1 Chemicals and Materials.

All solutions were prepared with water having a resistivity of 18MΩcm or higher (Barnstead Nanopure Systems). Two types of PS-b-PMMA and PS (31K PS-b-PMMA: Mn = 21500g/mol for PS and 10000g/mol for PMMA, Mw/Mn = 1.06; 82K PS-b-PMMA: Mn = 57000g/mol for PS and 25000g/mol for PMMA, Mw/Mn = 1.07; 115K PS, Mn = 115000g/mol, Mw = 119600, Mw/Mn = 1.04) were purchased from Polymer Source and used as received. Potassium dihydrogen phosphate (Fisher Chemical), Potassium nitrate (Fisher Chemical), Potassium hydroxide (Fisher Chemicals), Potassium ferricyanide (Acros Organics), Potassium ferrocyanide (Acros Organics) were used as received. Toluene (Fisher Chemicals), Methylene chloride (Fisher Chemicals), Methyl ethyl ketone (Fisher Chemicals), di ethyl ether (Fisher Chemicals) and ethanol (Decon Labs inc.) were used as received. Aqueous solutions saturated with organic solvents were prepared by saturating the aqueous layer with above solvents. Gold coated Si wafers which were prepared by sputtering 10nm Ti, followed by 20nm of Au onto Si (100) wafers were purchased from LGA Thin Films (Foster City, CA).

5.2.2 Preparation of PS-b-PMMA films

Gold coated Si wafers were cleaned in Novascan PSD-UVT-UV ozone system for 30min prior to use. Thin films of PS-b-PMMA were prepared on gold substrate by spin coating (2000rpm, 40s) from its toluene solution (0.75% w/w). Spin coated PS-b-PMMA films were annealed at 180°C in vacuum (ca. 0.3 Torr) for 60h to form cylindrical PMMA domains. The PMMA domains were etched via UV irradiation using a Novascan-PSD-UVT-UV ozone system

(ca 20mW/cm^2) under an Ar atmosphere. UV irradiation involves simultaneous cross linking of PS matrix and etching of PMMA. Then the degraded PMMA domains were removed by rinsing with glacial acetic acid[7, 39] The thickness of the PS-b-PMMA film was measured using a J.A. Woollam alpha-SE spectroscopic ellipsometer. The ellipsometric thickness of the annealed PS-b-PMMA films prior to PMMA etching was in the range of 30-35nm for 82K and 31K PS-b-PMMA.

5.2.3 Electrochemical measurements

Electrochemical Impedance measurements were performed in a three-electrode cell containing a Ag/AgCl (3M KCl) reference electrode and a Pt counter electrode, using CH instruments model 618B electrochemical analyzer. AC impedance measurements were done in 3mM $K_3Fe(CN)_6$ / 3mM $K_4Fe(CN)_6$ / 0.1M phosphate buffer (pH ~7), by applying a 5 mV ac potential and the dc potential was held at 0.22 V. The voltage frequencies used for impedance measurements were in the range of 10^5 Hz to 0.001 Hz. Complex impedance plots were fitted to equivalent circuit to obtain the necessary parameters. The working electrode, a PS-b-PMMA nano-porous film coated on Au/Si substrate was immobilized at the bottom of the Teflon cell. The diameter of the area exposed to the solution was defined by the "O" ring (diameter 0.66 cm, A = 0.34 cm^2).

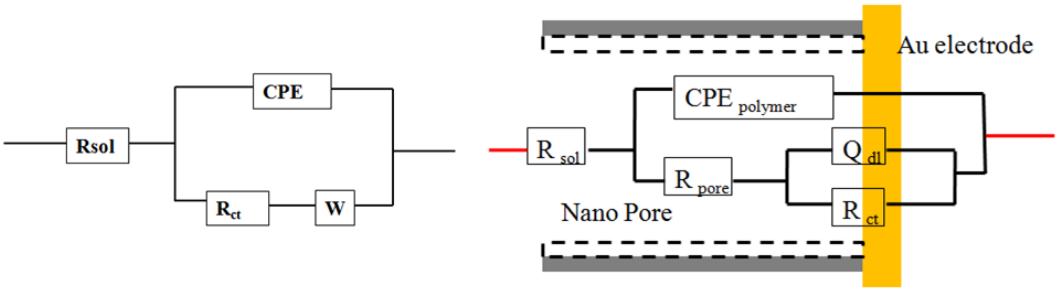

Figure 5.1 Randle's equivalent circuit for bare gold electrode (left) and PS-b-PMMA nanoporous film coated gold electrode (right).

5.2.4 AFM Measurements

AFM images were obtained by contact mode imaging in solution using a Picoscan SPM (Molecular Imaging) within a liquid cell. Contact mode, non reflex coated tips from Nano

Science Instruments; Vista Probes (cantilever length 225 μm, width 45 μm, spring constant 0.1 N/m, resonant frequency 28 kHz) were first rinsed in ethanol and then cleaned in a Novascan PSD-UVT-UV ozone system for 10 min. The tips were kept immersed in methanol till imaging was done.

5.3 Results and Discussion.

5.3.1 Electrochemical characterization of the PS-b-PMMA nano-porous film on Au substrate.

PS-b-PMMA nano-porous electrodes were characterized by measuring (a) capacitive current (to estimate the active surface area) and (b) Faradic current of $K_3Fe(CN)_6$ at different scan rates. Active surface area of the PS-b-PMMA nano-porous electrode can be determined by charging current measurements.[40] The extent of the PMMA removal by UV irradiation can be determined from the CVs of redox current measurements of $K_3Fe(CN)_6$.[41]

(a) Capacitive current measurements – capacitive current on a PS-b-PMMA film based nano-porous electrode was obtained by measuring CVs in 0.1M KNO_3. Current at 0.1V vs. Ag/AgCl was used to calculate electrode area of the PS-b-PMMA nano-porous electrode, using the double layer capacitance of gold surface that was measured on a gold disk electrode (5.7×10^{-5} F/cm^2). If all the PMMA domains have been removed by UV irradiation and sonication in acetic acid, then the active surface area of the PS-b-PMMA nano-porous electrode would be close to the volume fraction of PMMA domains (30%). Thus the cross sectional area exposed gold enclosed by the "O" ring should be 1.03×10^{-1} cm^2. If the PS-b-PMMA film was detached from the gold surface the active area obtained would be larger than the expected value. Our experimental area was $(1.9 \pm 0.51) \times 10^{-1}$ cm^2 (average ± st. dev. From 8 separate 82K PS-b-PMMA cells).

(b) Faradaic current measurements – CVs of 3.0mM $K_3Fe(CN)_6$ on PS-b-PMMA nano-porous electrode was measured at different scan rates (υ, from 500mV/s to 10 mV/s). Figure 5.2 shows the CVs of 3.0 mM $K_3Fe(CN)_6$ on PS-b-PMMA nano-porous electrode. When PMMA has been completely removed by UV irradiation, we were

able to observe peak shaped CVs at slower scan rates (40- 10 mV/s), due to overlapping of radial diffusion regimes of individual nano-pores.[42-44] In some cases (Figure 5.3), we observed a sigmoidal CVs at slower scan rates. This might be due to the presence of a very thin polymer layer (PS) on the gold surface or partial alignment of cylindrical PMMA domains.

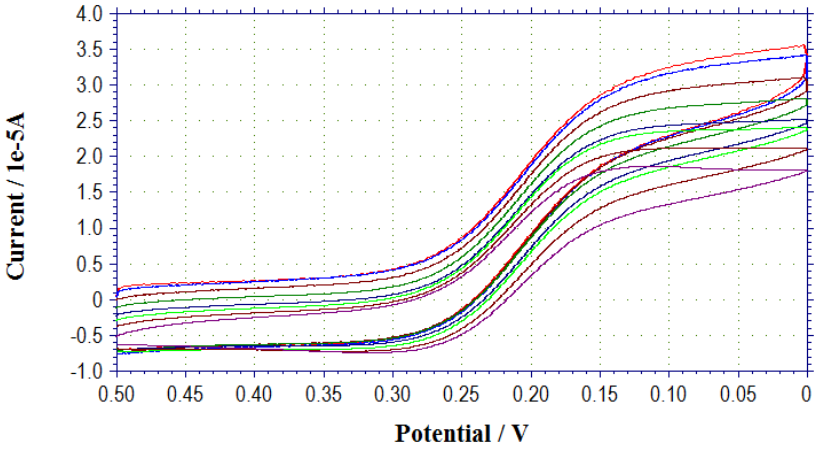

Figure 5.2 Overlaid CVs (scan rate 500 – 10mV/s) for 3mM $K_3Fe(CN)_6$, 0.1M KNO_3 on a 82K PS-b-PMMA nano-porous film coated Au electrode. (Complete removal of PMMA domains)

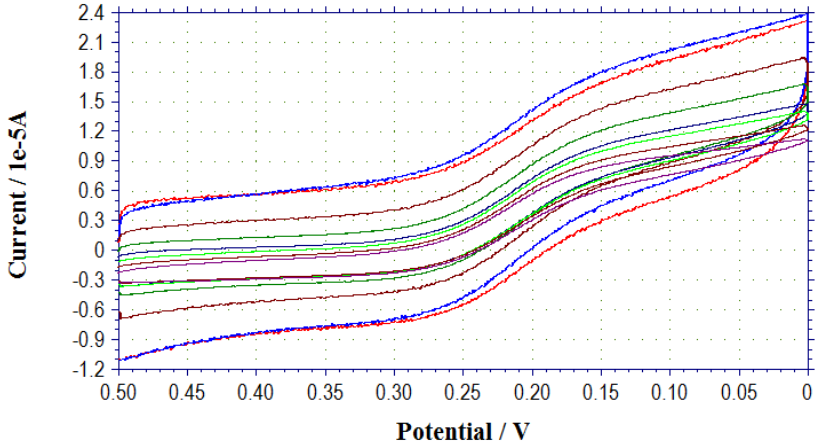

Figure 5.3 Overlaid CVs (scan rate 500 – 10mV/s) for 3mM $K_3Fe(CN)_6$, 0.1M KNO_3 on a 82K PS-b-PMMA nano-porous film coated Au electrode. (Incomplete removal of PMMA domains).

5.3.2 Stabilization of PS-b-PMMA nano-porous electrode /PS coated electrode before impedance measurements in organic solvents

The PS-b-PMMA films coated and PS coated electrodes were stabilized by taking a series of impedance spectra without adding any organic solvents (Figure 5.4 and 5.5). During the time scale of stabilization measurements (~6.5h), we observed a decrease in the response of pore resistance (R_{pore}) of both PS-b-PMMA and PS films. This might be due to alteration of the di-block copolymer material with constant exposure to phosphate buffer/ redox molecules. Previous studies have reported an increase in the gold oxide formation peak at PS coated gold electrode. Initially the smaller peaks indicated less gold oxide formed on the electrode surface, but with continuous CV measurements, the height these peaks increased due to formation of pin holes/ defects of the PS coating or increase in the average size of pin holes.[45] Thus our observations in the decrease of pore resistance might be due to formation of new pin holes and/ or increase in their average size.

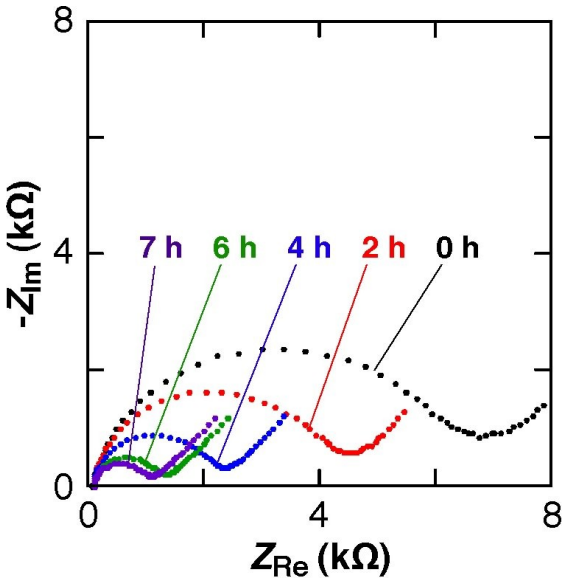

Figure 5.4 Electrochemical impedance spectra for stabilization of 82K PS-b-PMMA film for ~ 6.5hrs in $Fe(CN)_6^{3-}/Fe(CN)_6^{4-}$ 0.1 M phosphate (pH 7).

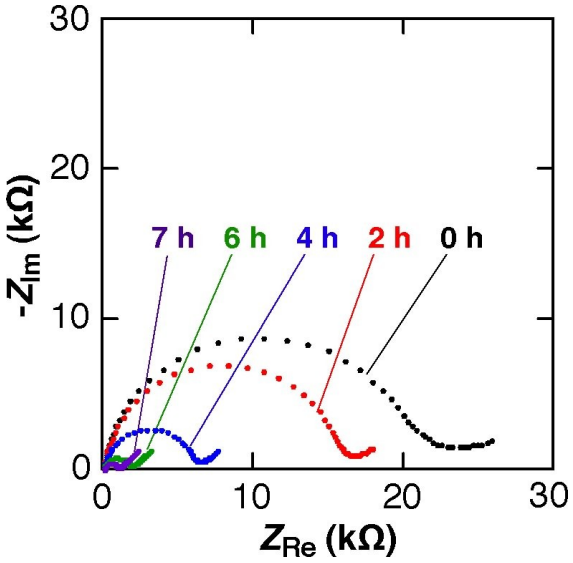

Figure 5.5 Electrochemical impedance spectra for stabilization of PS brush electrode for ~ 6.5hrs in $Fe(CN)_6^{3-}/Fe(CN)_6^{4-}$ 0.1 M phosphate (pH 7).

5.3.3 Permeability changes induced by organic solvents for 82K PS-b-PMMA films.

AC impedance was used to determine the permeability changes in PS-b-PMMA nano-porous film, induced by five organic solvents. Impedance measurements were taken in 3mM $K_3Fe(CN)_6$ / 3mM $K_4Fe(CN)_6$ / 0.1M phosphate buffer (pH ~7) solution. This technique is widely used in assessing self assembled monolayers,[46, 47] polymer brush electrodes[48, 49] and polymer coatings,[50] since it provides information of electrochemical processes occurring at the electrode surface. We compared the impedance spectra obtained from a bare gold electrode and PS-b-PMMA nano-porous electrode. Figure 5.6 shows impedance responses obtained from a bare gold electrode for five different solvents. Data fitting to an equivalent circuit (Figure 5.1) enabled us to extract parameters such as charge transfer resistance, double layer capacitance and Warburg impedance, which provides details on kinetic and diffusion controlled processes on the electrode surface. For the bare gold electrode, impedance spectra did not show a dependence on the solvent type used, and the less defined semi circle at higher frequency range was due to fast electrode reaction occurring at the bare gold surface. A 45° line characteristic of Warburg impedance was observed,[51] indicating that the redox reaction was diffusion controlled.[46, 47, 52, 53]

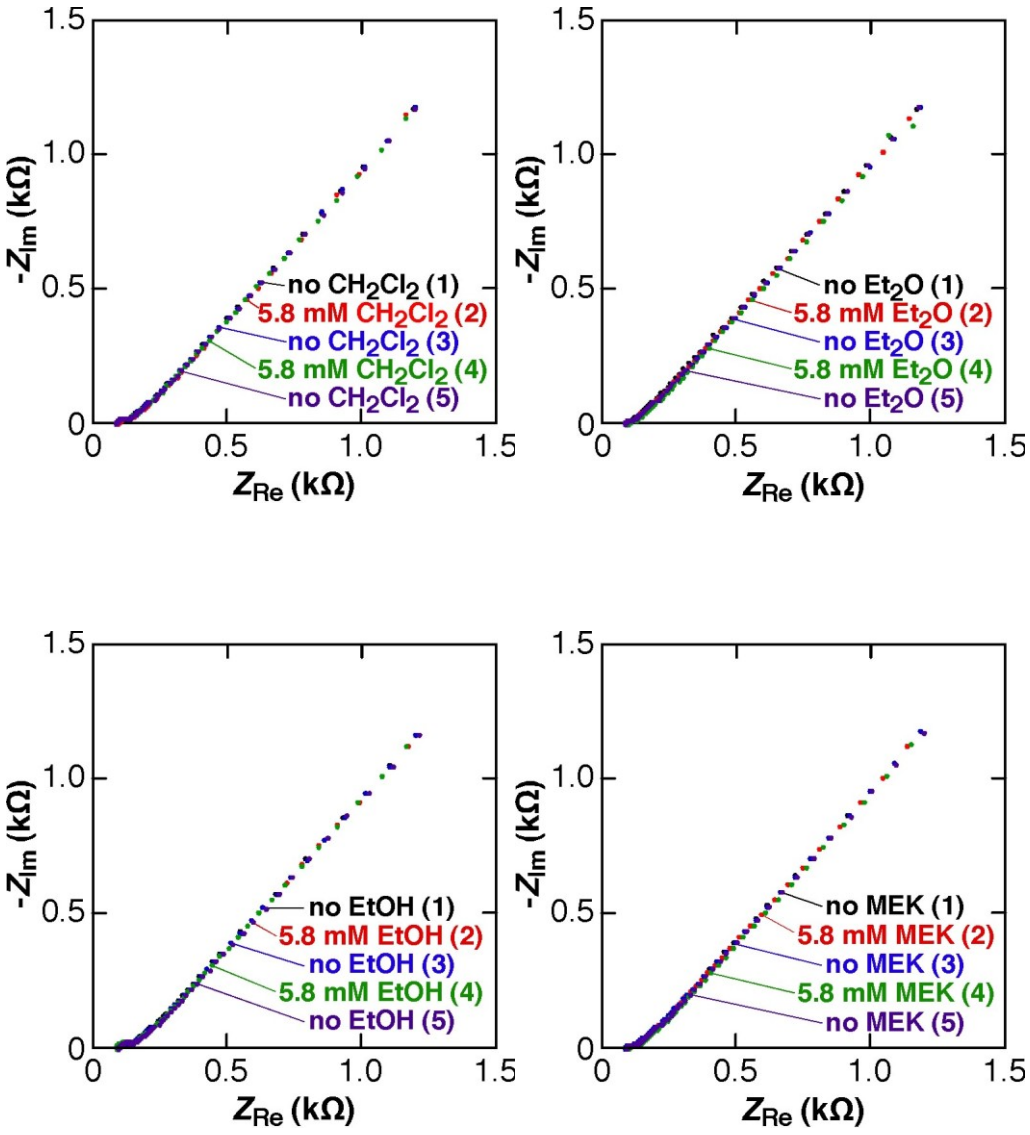
1.5
1.0
0.5
0
0
0.5
1.0
1.5
-Z_Im (kΩ)
Z_Re (kΩ)
no CH2Cl2 (1)
5.8 mM CH2Cl2 (2)
no CH2Cl2 (3)
5.8 mM CH2Cl2 (4)
no CH2Cl2 (5)
no Et2O (1)
5.8 mM Et2O (2)
no Et2O (3)
5.8 mM Et2O (4)
no Et2O (5)
no EtOH (1)
5.8 mM EtOH (2)
no EtOH (3)
5.8 mM EtOH (4)
no EtOH (5)
no MEK (1)
5.8 mM MEK (2)
no MEK (3)
5.8 mM MEK (4)
no MEK (5)

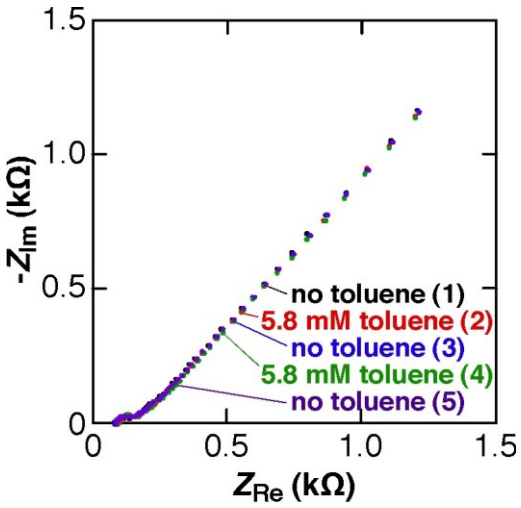

Figure 5.6 Electrochemical impedance spectra for bare gold electrode in 5.8mM organic solvents / in $Fe(CN)_6^{3-}/Fe(CN)_6^{4-}$ 0.1 M phosphate (pH 7). Top left response for Methylene chloride, top right response for diethyl ether, middle left response in ethanol, middle right response for methyl ethyl ketone, and bottom left response for toluene.

In contrast to the bare gold electrode, we observed a prominent semi circle in the high frequency range in complex impedance plots for PS-b-PMMA nano-porous electrodes (Figure 5.7). Complex impedance plots obtained in the presence and absence of toluene, methylene chloride, methyl ethyl ketone, ethanol and di-ethyl ether, were fitted to an equivalent circuit which incorporated pore resistance and capacitance of the polymer film (Figure 5.1). We assume that the electrochemical reaction occurs only at the exposed area on the gold electrode and that the redox molecules diffuse through the nanopores in the PS-b-PMMA film. Thus the equivalent circuit developed from the pin-hole model is appropriate for fitting the complex impedance plots.[54-56]

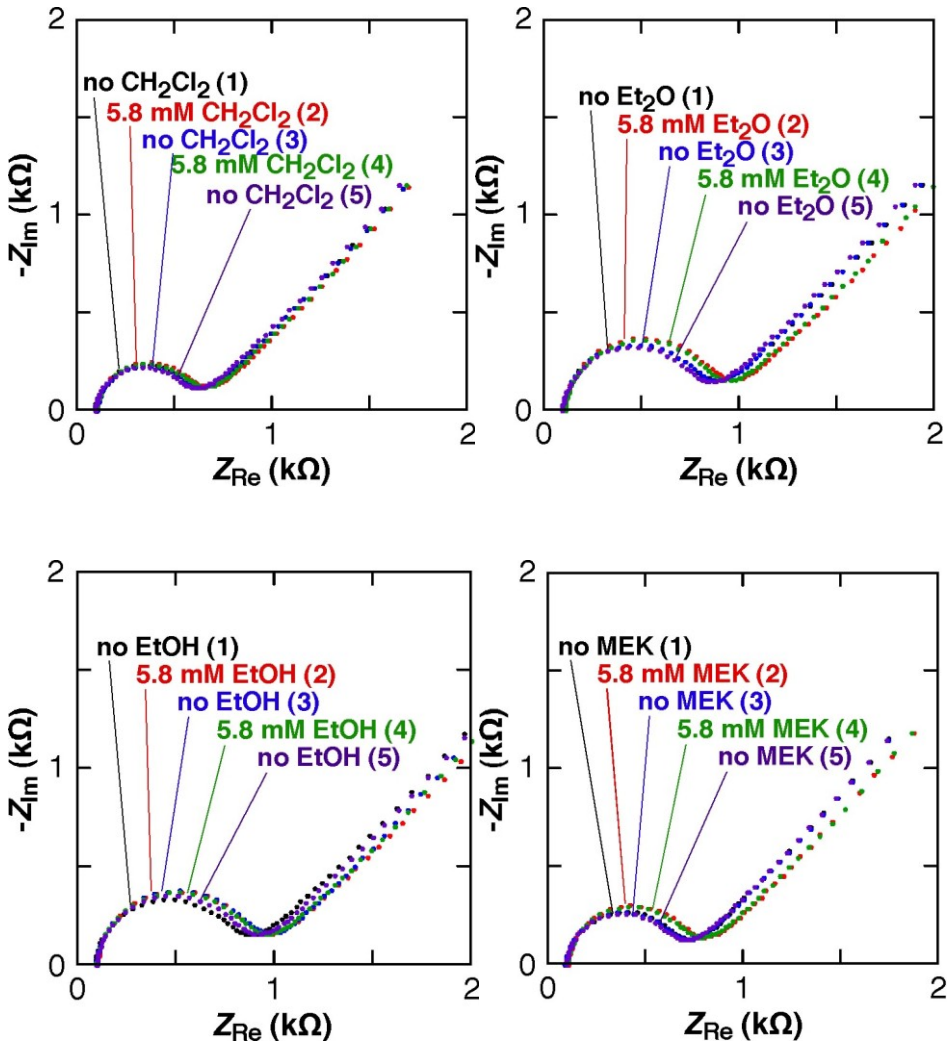
no CH_2Cl_2 (1)
5.8 mM CH_2Cl_2 (2)
no CH_2Cl_2 (3)
5.8 mM CH_2Cl_2 (4)
no CH_2Cl_2 (5)
no Et_2O (1)
5.8 mM Et_2O (2)
no Et_2O (3)
5.8 mM Et_2O (4)
no Et_2O (5)
no EtOH (1)
5.8 mM EtOH (2)
no EtOH (3)
5.8 mM EtOH (4)
no EtOH (5)
no MEK (1)
5.8 mM MEK (2)
no MEK (3)
5.8 mM MEK (4)
no MEK (5)
$-Z_{Im}$ (kΩ)
Z_{Re} (kΩ)
0
1
2

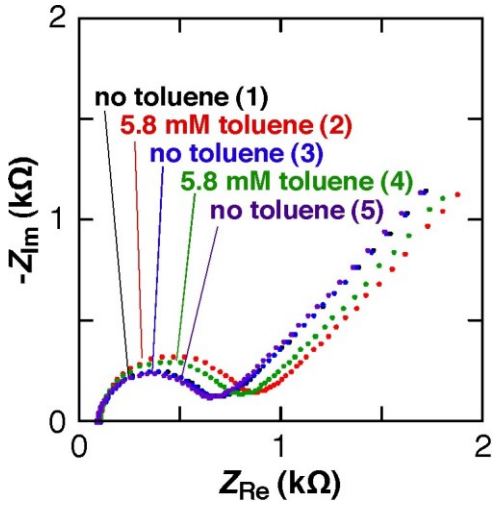

Figure5.7 Electrochemical impedance spectra for 82K PS-b-PMMA nanoporous electrode in 5.8mM organic solvents / in $Fe(CN)_6^{3-}/Fe(CN)_6^{4-}$ 0.1 M phosphate (pH 7). Top left response for Methylene chloride, top right response for diethyl ether, middle left response in ethanol, middle right response for methyl ethyl ketone, and bottom left response for toluene.

Pore resistance (R_{pore}) values obtained in the presence of organic solvents were higher than that in the absence of the solvents for PS-b-PMMA films. The change in R_{pore} can be related to swelling of the polymer or partitioning of the organic solvent inside the nanopores (equation 5.1) If PS swells due to organic solvents we should observe an increase in the thickness of the PS-b-PMMA film and a decrease in the pore diameter, which gives a larger value for R_{pore}. On the other hand if partitioning of the solvent occurs, resistivity ρ should change, again increasing R_{pore} of the nanopores.

$$R_{pore} = \rho\ (l / N\pi r^2) \qquad (5.1)$$

Where ρ is the resistivity of the organic solvent, l is the thickness of the PS-b-PMMA film (= nm), r is the pore diameter (= nm) and N is the number of open pores.

Also we observed reversible change in R_{pore}, indicating swelling / de-swelling or partitioning of organic solvent in PS-b-PMMA films with and without organic solvents. A higher R_{pore} indicated swelling or partitioning of solvent in the nano-pores, which leads to a decrease in permeability of redox molecules into the pores. Ratio of R_{pore} with and without organic solvents

is compared to identify which solvents give a larger response in terms of permeability changes. This can be expressed as follows

Ratio = R_{pore} in 5.8mM solvent solution / R_{pore} in buffer solution.

Table 5.1 summarizes the ratios obtained for PS brush electrode and 82K PS-b-PMMA nanoporous film for each organic solvent.

Table 5.1 Average and standard deviation for R_{pore}/ R_{pore}^0 values shown for PS brush and PS-b-PMMA nanoporous film in organic solvents (5.8mM concentration), Swelling Power (C) for each solvent and their solubility in water at 25°C (from Literature).

	Parameters	Toluene	CH_2Cl_2	MeCOEt	Et_2O	EtOH
6nm thick PS brush	R_{pore}/ R_{pore}^0	1.13 ± 0.11 (N = 3)	1.08 ± 0.03 (N = 3)	1.10 ± 0.09 (N = 3)	1.19 ± 0.08 (N = 3)	1.13 ± 0.02 (N = 3)
33-nm dia. PS nanopores from 82K PS-*b*-PMMA	R_{pore}/ R_{pore}^0	1.33 ± 0.23 (N = 6)	1.11 ± 0.07 (N = 6)	1.09 ± 0.03 (N = 3)	1.09 ± 0.02 (N = 3)	1.02 ± 0.01 (N = 3)
	Relative Swelling power of PS[36]	2.02	1.99	1.11	0.64	0.00
	Solubility in water at 25°C[57]	0.0531 wt% 0.0058M	1.75 wt% 0.21M	25.9 wt% 3.6M	6.04 wt% 0.81M	∞

PS brush electrode did not show any selectivity in the solvents used. The ratio of pore resistance is similar in all solvents used. In contrast PS nanopores from 82K PS-b-PMMA films show

larger ratio of pore resistance in toluene. According to the literature values, toluene and CH_2Cl_2 shows higher swelling power of PS.

For crosslinked PS matrix to be swollen in the presence of an organic solvent, cohesive energy density of the polymer and the solvent must be similar. Since for crosslinked polymers, solubility is measured by the degree of swelling, solubility parameters (δ) of the polymer (δ_p) and the solvent (δ_s) is used in calculating the extent of polymer swelling and maximum swelling of the polymer is observed when $(\delta_p - \delta_s)^2 = 0$[34, 58] The volume of solvent adsorbed (S in other words the swellability of the polymer) for per unit mass of PS has been determined from the following relationship between the S and the weight of polymer in the dried and saturated with the solvent state. (Equation 5.2)[37]

$$S = [(W_s - W_0)/d - V_0] / xW_0 \qquad (5.2)$$

Where S (mL) is the volume of solvent adsorbed per gram of polymer, W_s (g) is the weight of polymer saturated with the solvent, W_0 (g) is the weight of the dried polymer, d (g/mL) is the density of the solvent, and x is the weight fraction of polymer film, and V_0 is the void volume of the polymer film. S (swellability) of the polymer is related to the swelling power of the solvent C through the cross linking density λ (equation 5.3)[34, 37].

$$S = C (\lambda^{1/3} - \lambda_0^{1/3}) \qquad (5.3)$$

Where C is the swelling power, λ is the average number of carbon atoms in the backbone of PS segments between cross linked fragments and λ_0 is the critical cross link density of the PS. The literature values of C, swelling power of toluene, Methylene chloride, Methyl ethyl ketone di-ethyl ether and ethanol are 2.02, 1.99, 1.11, 0.64 and 0.00 respectively.[34] Thus the swelling of PS should be a maximum in toluene. We observed maximum impedance for the nano-porous film in toluene, represented by a larger semi circle diameter R_{pore} (R_{pore}/ R_{pore}^0 ratio). Our PS-b-PMMA nano-porous films showed a larger response to toluene as compared to the other organic solvents used. Swelling in ethanol was lowest which is in agreement with the swelling power of 0.00. Thus 82K PS-b-PMMA films are selective towards toluene. Figure 5.8 compares the R_{pore} values obtained for 5.8mM toluene and CH_2Cl_2. Even though the swelling powers for these two solvents are nearly the same, the largest reversible change in R_{pore} of the Nyquist plot is given by toluene. The difference in response to toluene and Methylene chloride might arise from the difference of solubility of each solvent in water. Toluene has a lower solubility in water than

Methylene chloride, thus it is likely that toluene partition into hydrophobic PS nanopores. However, Methylene chloride is more polar than toluene, and is less likely to partition into a hydrophobic environment such as PS nanopores.

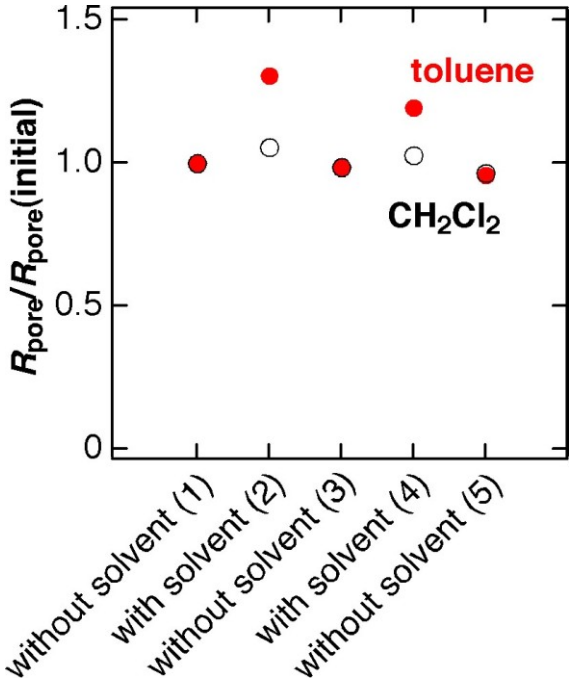

Figure 5.8 Ratio of R_{pore} /R_{pore}^0 for toluene (5.8mM) and CH_2Cl_2 for 82K PS-b-PMMA nanoporous film.

5.3.4AFM data for 82K PS-b-PMMA films in organic solvents.

To determine if the permeability change of PS-b-PMMA films in organic solvents is due to swelling of the polymer or partitioning of the solvent within the nanopores, we did AFM imaging of PS-b-PMMA films in the presence and absence of the solvents. We used contact mode AFM to obtain topographic images of these films. Figures 5.9 to 5.13 shows the AFM images obtained without the organic solvent and with organic solvent. These images are 1μm X 1 μm, 1024 pixels and taken in 0.1m phosphate buffer (pH ~7).

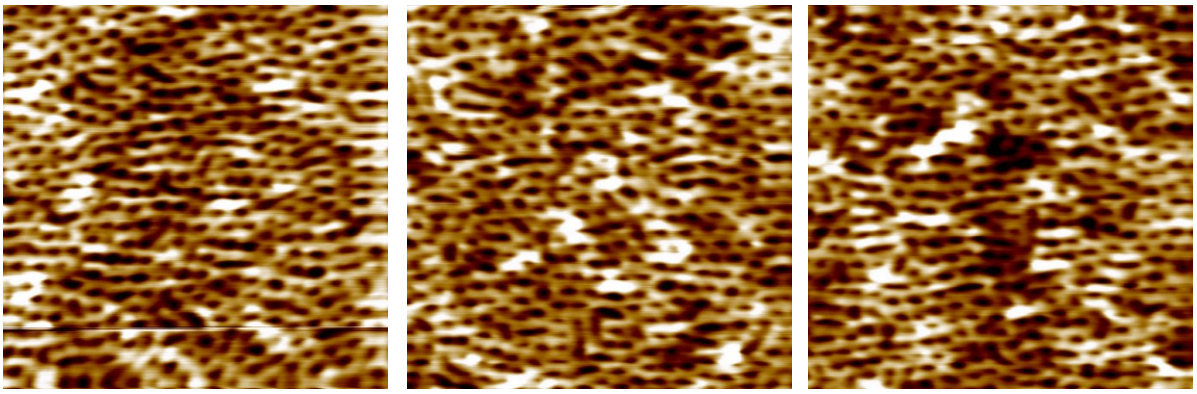

Figure 5.9 Contact mode AFM images for 82K PS-b-PMMA in the presence and absence of 5.8mM methyl ethyl ketone. Left image without MEK (ΔZ = 4nm), middle image in MEK (ΔZ = 3.6nm), right image without MEK (ΔZ = 3.7nm).

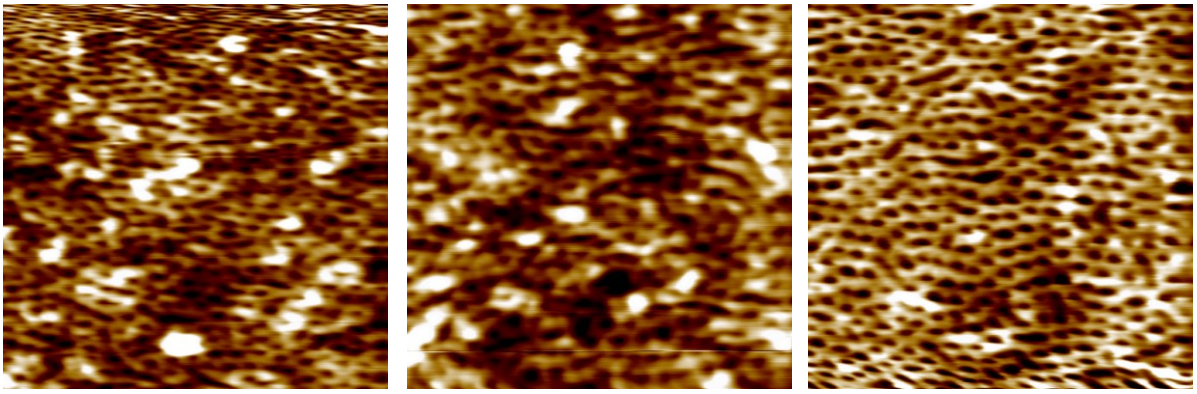

Figure 5.10 Contact mode AFM images for 82K PS-b-PMMA in the presence and absence of 5.8mM Di-ethyl ether. Left image without ether (ΔZ = 4nm), middle image in ether (ΔZ = 2.6nm), right image without ether (ΔZ = 5.3nm).

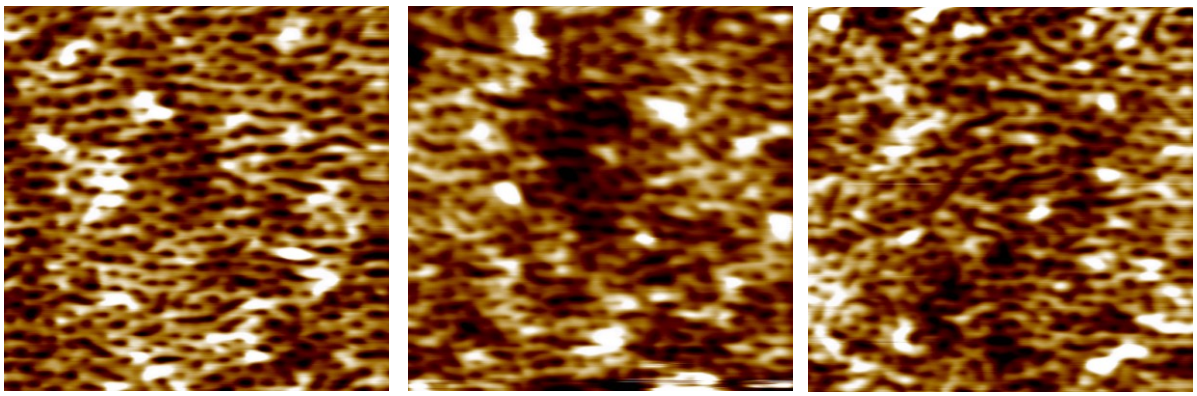

Figure 5.11 Contact mode AFM images for 82K PS-b-PMMA in the presence and absence of 5.8mM CH_2Cl_2. Left image without CH_2Cl_2 (ΔZ = 3.4nm), middle image in CH_2Cl_2 (ΔZ = 3.0nm), right image without CH_2Cl_2(ΔZ = 3.0nm).

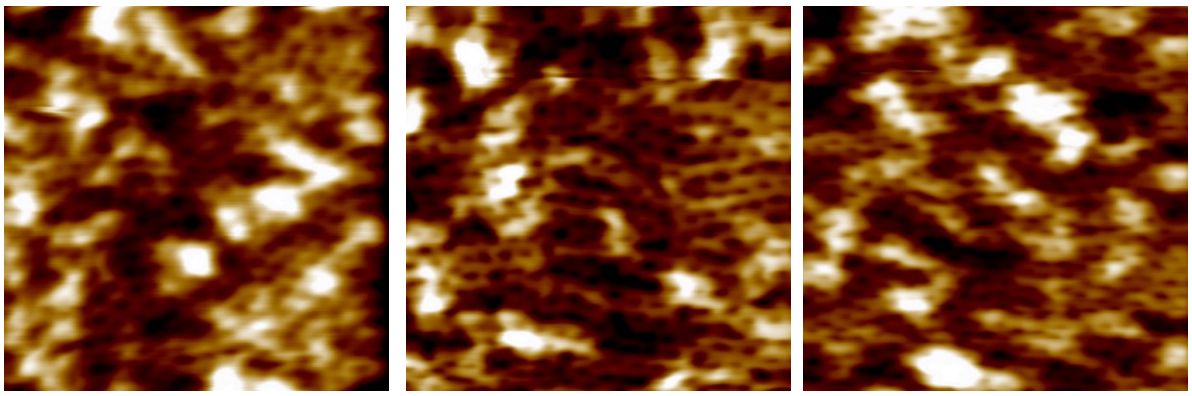

Figure 5.12 Contact mode AFM images for 82K PS-b-PMMA in the presence and absence of 5.8mM Ethanol. Left image without EtOH (ΔZ = 4.5nm), middle image in EtOH (ΔZ = 5.4nm), right image without EtOH (ΔZ = 8.0nm).

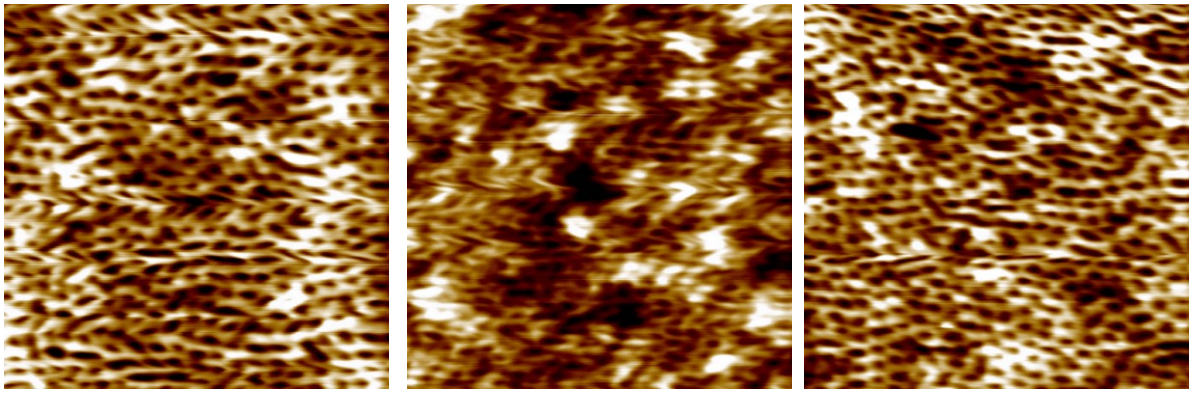

Figure 5.13 Contact mode AFM images for 82K PS-b-PMMA in the presence and absence of 5.8mM Toluene. Left image without toluene (ΔZ = 3.3nm), middle image in toluene (ΔZ = 2.0nm), right image without toluene (ΔZ = 2.8nm).

The topographic AFM images obtained for CH_2Cl_2, Methyl ethyl ketone, diethyl ether and ethanol did not show an appreciable change in the pore diameter. The pore diameters determined from the AFM images with and without organic solvents did not give large changes. (The standard deviation was also high for the averaged pore diameters.) Thus the pore resistance indicated by semi circle in Nyquist plots is not due to swelling of the nanopores. When the PS-b-PMMA films were imaged in 5.8mM toluene/ 0.1M phosphate buffer, the images appeared to be swelled (but without any appreciable change in pore diameter) than the images obtained without toluene. The topography of these images seems to have a lubricant character, indicating that toluene might be partitioned into the relatively hydrophobic nanopores. Thus the increase in R_{pore} is due to the increase in resistivity of the solvent given by ρ in equation 5.1.

5.3.5 Permeability changes induced by organic solvents for PS brush electrodes.

We measured the permeability change induced by organic solvents on PS brush electrodes by EIS. Before impedance measurements were done in organic solvents, PS brush electrodes were tested for their stability, by taking a series of impedance spectra in 3mM $K_3Fe(CN)_6$ / 3mM $K_4Fe(CN)_6$ / 0.1M phosphate buffer (pH ~7) solution (Figure 5.5). Stability of PS brush electrodes were less than the 82K PS-b-PMMA nanoporous films. Impedance spectra obtained in toluene, CH_2Cl_2, Methyl ethyl ketone, di-ethyl ether and ethanol, did not show any selectivity on PS brush electrode. There was a gradual decrease in the semi circle portion of the Nyquist plots, indicating decreasing R_{pore} due to detachment of PS brushes (Figure 5.14). In contrast to PS-b-PMMA nanoporous film, the response R_{pore} in the presence of organic solvents were not reversible for the PS brush electrode.

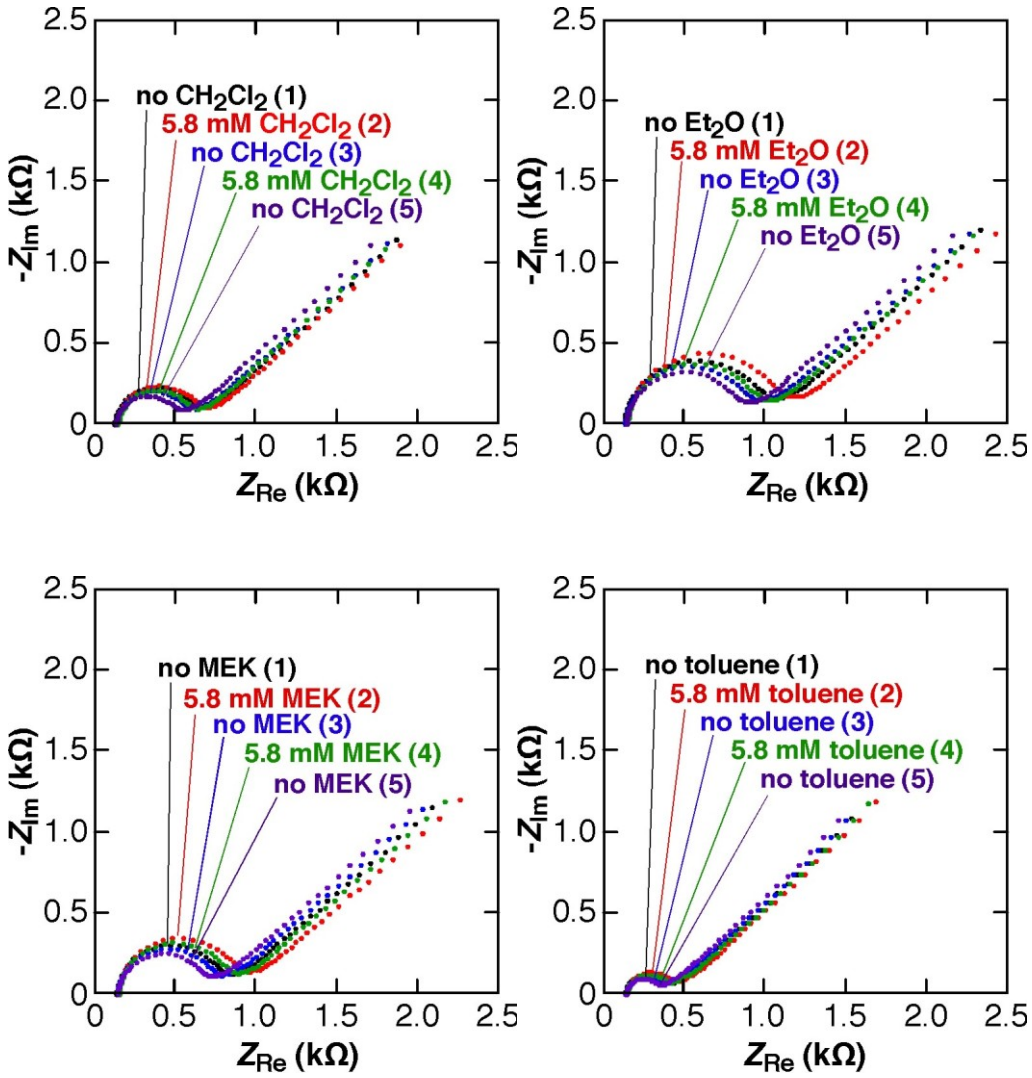
no CH_2Cl_2 (1)
5.8 mM CH_2Cl_2 (2)
no CH_2Cl_2 (3)
5.8 mM CH_2Cl_2 (4)
no CH_2Cl_2 (5)
no Et_2O (1)
5.8 mM Et_2O (2)
no Et_2O (3)
5.8 mM Et_2O (4)
no Et_2O (5)
no MEK (1)
5.8 mM MEK (2)
no MEK (3)
5.8 mM MEK (4)
no MEK (5)
no toluene (1)
5.8 mM toluene (2)
no toluene (3)
5.8 mM toluene (4)
no toluene (5)
$-Z_{Im}$ (kΩ)
Z_{Re} (kΩ)
0
0.5
1.0
1.5
2.0
2.5

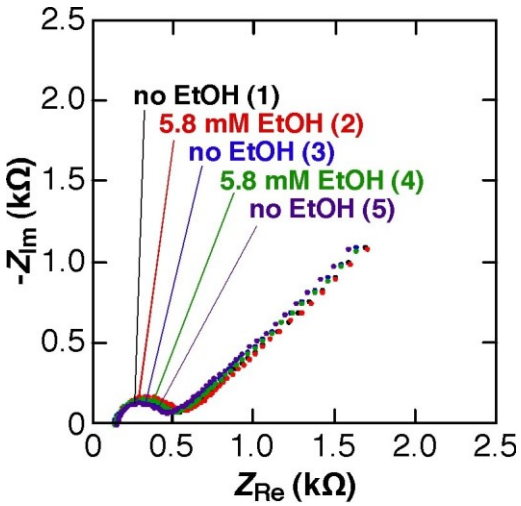

Figure 5.14 Electrochemical impedance spectra for 115K PS brush electrode in 5.8mM organic solvents / in $Fe(CN)_6^{3-}/Fe(CN)_6^{4-}$ 0.1 M phosphate (pH 7). Top left response for Methylene chloride, top right response for diethyl ether, middle left response in methyl ethyl ketone, middle right response for toluene, and bottom left response for ethanol.

5.4 Conclusions.

In this chapter we demonstrated the permeability changes induced by organic solvents, in PS-b-PMMA di-block copolymers. A significant change in the pore resistance was observed for toluene. This might be due to partitioning of hydrophobic toluene in relatively hydrophobic PS-b-PMMA nanopores rather than swelling of the nanoporous membrane. We come to this conclusion because we did not observe appreciable change in pore diameter in the presence of organic solvent from the AFM images. Therefore the reversible change in R_{pore} should be due to solvent partitioning inside the nanopores. A higher partitioning of toluene may be due to the lesser degree of solubility of toluene in water. Thus phase separation in toluene – aqueous may be higher than the rest of the solvents used. Thus 82K PS-b-PMMA nano-porous films showed higher sensitivity towards toluene. The PS brush electrodes were not sensitive to the solvents used, compared with the PS-b-PMMA nanoporous film. Also it was not as stable as PS-b-PMMA film, thus PS-b-PMMA films are more suitable for sensors than PS brush electrodes.

References

(1) Hillmyer, M. A. *Adv. Polym Sci.* **2005***, 190*, 137-181.

(2) Olson, D. A.; Chen, L.; Hillmyer, M. A. *Chemistry of Materials* **2008***, 20*, 869-890.

(3) Li, M.; Coenjarts, C. A.; Ober, C. K. *Adv. Polym Sci.* **2005***, 190*, 183-226.

(4) Zalusky, A. S.; Olayo-Valles, R.; Wolf, J. H.; Hillmyer, M. A. *J. Am. Chem. Soc.* **2002***, 124*, 12761-12773.

(5) Chung, C. M.; Lee, J. H.; Cho, S. Y.; Kim, J. G.; Moon, S. Y. *J Appl. Polym. Sci.* **2006***, 101*, 532-538.

(6) Melde, B. J.; Burkett, S. L.; Xu, T.; Goldbach, J. T.; Russell, T. P.; Hawker, C. J. *Chemistry of Materials* **2005***, 17*, 4743-4749.

(7) Thurn-Albrecht, T.; Schotter, J.; Kastle, G. A.; Emley, N.; Shibauchi, T.; Krusin-Elbaum, L.; Guarini, K.; Black, C. T.; Tuominen, M. T.; Russell, T. P. *Science* **2000***, 290*, 2126-2129.

(8) Kim, H. C.; Jia, X.; Stafford, C. M.; Kim, D. H.; McCarthy, T. J.; Tuominen, M.; Hawker, C. J.; Russell, T. P. *Adv Mater* **2001***, 13*, 795-797.

(9) Crossland, E. J. W.; Ludwigs, S.; Hillmyer, M. A.; Steiner, U. *Soft Mater.* **2007***, 3*, 94-98.

(10) Park, M.; Harrison, C.; Chaikin, P. M.; Register, R. A.; Adamson, D. H. *Science* **1997***, 276*, 1401-1404.

(11) Zschech, D.; Kim, D. H.; Milenin, A. P.; Hopfe, S.; Scholz, R.; Goring, p.; Hillebrand, R.; Senz, S.; Hawker, C. J.; Russell, T. P.; Steinhart, M.; Gosele, U. *Nanotechnology* **2006***, 17*, 2122-2126.

(12) Zhang, Q.; Xu, T.; Butterfield, D.; Misner, M. J.; Ryu, D. Y.; Emrick, T.; Russell, T. P. *Nano Letters* **2005***, 5*, 357-361.

(13) Fu, G. D.; Yuan, Z.; Kang, E. T.; Neoh, K. G.; Lai, D.; Huan, A. *Adv. Funct. Mater.* **2005***, 15*, 315-322.

(14) Yang, S.; Ryu, I.; Kim, H.; Kim, J.; Jang, S.; Russell, T. *Adv Mater* **2006***, 18*, 709-712.

(15) Li, Y.; Ito, T. *Anal. Chem.* **2009***, 81*, 851-855.

(16) Uehara, H.; Kakiage, M.; Sekiya, M.; Sakuma, D.; Yamonobe, T.; Takano, N.; Barraud, A.; Meurville, E.; Ryser, P. *ACS Nano* **2009***, 3*, 924-932.

(17) Rzayev, J.; Hillmyer, M. A. *J. Am. Chem. Soc.* **2005***, 127*, 13373-13379.

(18) Jeong, U.; Ryu, D.; Kho, D.; Kim, J.; Goldbach, J.; Kim, D.; Russell, T. *Adv Mater* **2004***, 16*, 533-536.

(19) Xuan, Y.; Peng, J.; Cui, L.; Wang, H.; Li, B.; Han, Y. *Macromolecules* **2004***, 37*, 7301-7307.

(20) Fasolka, M. J.; Mayes, A. M. *Annual Review of Materials Research* **2001***, 31*, 323-355.

(21) Thurn-Albrecht, T.; DeRouchey, J.; Russell, T. P.; Jaeger, H. M. *Macromolecules* **2000***, 33*, 3250-3253.

(22) Bailey, T. S.; Rzayev, J.; Hillmyer, M. A. *Macromolecules* **2006***, 39*, 8772-8781.

(23) Klaikherd, A.; Ghosh, S.; Thayumanavan, S. *Macromolecules* **2007***, 40*, 8518-8520.

(24) Li, Y.; Ito, T. *Langmuir* **2008***, 24*, 8959-8963.

(25) Lavine, B. K.; kaval, N.; Westover, D. J.; Oxenford, L. *Anal. Lett.* **2006***, 39*, 1773-1783.

(26) Zhang, L.; Langmuir, M. E.; Bai, M.; Rudolf Seitz, W. *Talanta* **1997***, 44*, 1691-1698.

(27) Zhang, Z.; Shakhsher, Z.; Seitz, W. R. *Microchimica Acta* **1995***, 121*, 41-50.

(28) Tokarev, I.; Orlov, M.; Katz, E.; Minko, S. *The Journal of Physical Chemistry B* **2007***, 111*, 12141-12145.

(29) Cong, J.; Zhang, X.; Chen, K.; Xu, J. *Sensors Actuators B: Chem.* **2002***, 87*, 487-490.

(30) McCurley, M. F.; Seitz, W. R. *Anal. Chim. Acta* **1991***, 249*, 373-380.

(31) Asher, S. A.; Alexeev, V. L.; Goponenko, A. V.; Sharma, A. C.; Lednev, I. K.; Wilcox, C. S.; Finegold, D. N. *J. Am. Chem. Soc.* **2003***, 125*, 3322-3329.

(32) Kataoka, K.; Miyazaki, H.; Bunya, M.; Okano, T.; Sakurai, Y. *J. Am. Chem. Soc.* **1998***, 120*, 12694-12695.

(33) Shakhsher, Z. M.; Odeh, I.; Jabr, S.; Rudolf Seitz, W. *Microchimica Acta* **2004***, 144*, 147-153.

(34) Errede, L. A. *Macromolecules* **1986***, 19*, 1522-1525.

(35) Errede, L. A. *Macromolecules* **1986***, 19*, 1525-1528.

(36) Errede, L. A. *J. Phys. Chem.* **1989***, 93*, 2668-2671.

(37) Errede, L. A. *J. Appl. Polym. Sci.* **1986***, 31*, 1749-1761.

(38) Bai, D.; Habersberger, B. M.; Jennings, G. K. *J. Am. Chem. Soc.* **2005***, 127*, 16486-16493.

(39) Thurn-Albrecht, T.; Steiner, R.; DeRouchey, J.; Stafford, C. M.; Huang, E.; Bal, M.; Tuominen, M.; Hawker, C. J.; Russell, T. P. *Adv Mater* **2000***, 12*, 787-791.

(40) Penner, R. M.; Martin, C. R. *Anal. Chem.* **1987***, 59*, 2625-2630.

(41) Li, Y.; Maire, H. C.; Ito, T. *Langmuir* **2007***, 23*, 12771-12776.

(42) Ito, T.; Audi, A. A.; Dible, G. P. *Anal. Chem.* **2006***, 78*, 7048-7053.

(43) Amatore, C.; Savéant, J. M.; Tessier, D. *J Electroanal Chem* **1983***, 147*, 39-51.

(44) Zoski, C. G.; Yang, N.; He, P.; Berdondini, L.; Koudelka-Hep, M. *Anal. Chem.* **2007***, 79*, 1474-1484.

(45) Xia, S. J.; Liu, G.; Birss, V. I. *Langmuir* **2000***, 16*, 1379-1387.

(46) Sabatani, E.; Cohen-Boulakia, J.; Bruening, M.; Rubinstein, I. *Langmuir* **1993***, 9*, 2974-2981.

(47) Sabatani, E.; Rubinstein, I. *J. Phys. Chem.* **1987***, 91*, 6663-6669.

(48) Motornov, M.; Sheparovych, R.; Katz, E.; Minko, S. *ACS Nano* **2008***, 2*, 41-52.

(49) Tam, T. K.; Ornatska, M.; Pita, M.; Minko, S.; Katz, E. *The Journal of Physical Chemistry C* **2008***, 112*, 8438-8445.

(50) Domingues, L.; Oliveira, C.; Fernandes, J. C. S.; Ferreira, M. G. S. *Electrochim. Acta* **2002***, 47*, 2253-2258.

(51) Bard, A. J.; Faulkner, L. R., Eds.; In *Electrochemical Methods, Fundamentals and Applications;* Bard, A. J., Faulkner, L. R., Eds.; Wiley: New York, 2001; Vol. 2nd.

(52) Hunter, T. B.; Tyler, P. S.; Smyrl, W. H.; White, H. S. *J. Electrochem. Soc.* **1987***, 134*, 2198-2204.

(53) Rubinstein, I.; Sabatani, E.; Rishpon, J. *J. Electrochem. Soc.* **1987***, 134*, 3078-3083.

(54) Mansfeld, F. *Electrochim. Acta* **1990***, 35*, 1533-1544.

(55) Mansfeld, F. *Electrochim. Acta* **1993***, 38*, 1891-1897.

(56) Zhao, M.; Zhou, Y.; Bruening, M. L.; Bergbreiter, D. E.; Crooks, R. M. *Langmuir* **1997***, 13*, 1388-1391.

(57) Stephenson, R. M. *Journal of Chemical & Engineering Data* **1992***, 37*, 80-95.

(58) Lee, J. N.; Park, C.; Whitesides, G. M. *Anal. Chem.* **2003***, 75*, 6544-6554.

Chapter 6 – Conclusions and Future Research

In this research, we studied how self assembled monolayers, track etched polycarbonate membranes and PS-b-PMMA nanoporous films respond to certain environmental stimuli such as pH and organic solvents. When these stimuli were applied to afore mentioned materials, we observed a change in permeability of marker ions. We were able to relate the permeability change of Thioctic acid SAM and nanoporous TEPCM to a charged redox marker, to change in surface charge. In the case of PS-b-PMMA nanoporous film, we assign the permeability to partitioning of the organic solvent in the nanopores, thus altering the hydrophilic/ hydrophobic nature within the pores.

We prepared a thioctic acid SAM modified microelectrode to represent a simple charge based ion channel sensor. This can be also considered as a voltammetric electrochemical sensor, and we were able to CV responses of the redox current generated by the marker ions. By changing the medium pH the surface charge of the electrode can be tuned, which in turn affects the redox current. Change in the redox current reflected the rate of the electrode reaction at the charged electrode. By using closed form equations, we simulated the steady state quasi reversible CV responses and compared them with the experimentally obtained CVs. From the simulated CVs, effective rate constants at different pKa values were extracted, which was similar to a titration of rate constants vs. pH. The effect of surface charge change was explained in terms of Frumkin effect which is related to the distribution of ions in the electrical double layer and the altered potential at the outer Helmholtz plane. We only explored the Frumkin effect that contributed to the redox current of a charged marker at a charged electrode surface. It should be noted that there are other effects that contribute to the kinetics of an electrode reaction at a modified electrode.

A recessed nano disk array electrode was prepared from track etched polycarbonate membranes, having 10nm diameter. The surface charge of the nanopores was tuned by changing the medium pH. Depending on the protonation / deprotonation state of –COOH groups on the nanopore surface, redox current of charged markers (positive and negative) change. We assess the surface charge within the nanopore cavity by means of CV. This is because the redox current

is diffusion controlled and the change in the redox current will be due to the surface charge in the cavity, not the surface of the membrane. We also observed that the redox current of charged markers is affected by the concentration of the electrolyte used. This is due to extension of the electrical double layer adjacent to the pore surface with increasing electrolyte concentration. Thus permeability of charged markers would be further suppressed. The Faradaic current we observed for in this study were larger than the ones predicted from the theoretical equations, indicating enhanced mass transport. This may be due to partitioning of the redox markers in a distinct surface layer on the pore. In other words this indicates there is a difference of diffusion coefficients inside the pores and in the bulk solution.

In the work done related to PS-b-PMMA nanoporous films, the applied external stimulus was different from the previous two cases. We investigated the permeability changes in PS-b-PMMA nanoporous films induced by organic solvent. In the beginning of this work we hypothesized the permeability change was either due to swelling of the nanoporous film caused by the organic solvents or partitioning of the solvents in the nanopores. Both of these processes would increase the resistance of nanopores, indicated by a well developed semi circle in the Nyquist plots. If swelling of the nanoporous membrane occurs, the pore diameter should change reversibly, in the presence and absence of the organic solvents. But our AFM data did not show any appreciable change in the pore diameter. Thus we concluded that the permeability induced by the organic solvents was due to partitioning of the solvents inside the nanopores. We also noted that only toluene showed a reversible change in pore resistance, but not the other solvents used. Also we compared the stability and the response to organic solvents for both PS-b-PMMA nanoporous film and PS brush on gold substrate, and we found that PS brush was less stable than the PS-b-PMMA film and showed random response for solvents. Thus PS-b-PMMA is a better material than PS brush to prepare sensors that involves organic solvents.

In the work related to permeability changes induced by organic solvents in PS-b-PMMA nanoporous films, further investigation into partitioning of the solvents is needed. This can involve studying the other effects that would enhance the partitioning of solvents, such as temperature, cross linking density of the porous film and thickness of the PS-b-PMMA films. Understanding how these factors contribute to partitioning of the organic solvents will help us to

tune the properties of PS-b-PMMA films to be selective and sensitive in order to optimize its use as a sensor.